Luminescence study of III-nitride semiconductor nanostructures and LEDs

Dipl.-Phys. Jochen Bruckbauer

A thesis submitted to
the Department of Physics
University of Strathclyde
for the degree of
Doctor of Philosophy

9th July, 2013

For my Mom.

Declaration of author's right

This thesis is the result of the author's original research. It has been composed by the author and has not been previously submitted for examination which has lead to the award of a degree.

Signed: Date:

Abstract

In this work, cathodoluminescence (CL) hyperspectral imaging, photoluminescence (PL) and electroluminescence are used to study the optical properties of III-nitride semiconductor materials.

III-nitride semiconductors have successfully opened up the solid-state lighting market. Light-emitting diodes (LEDs) fabricated using III-nitrides, however, still suffer from numerous deficiencies such as high defect densities, efficiency droop and the 'green gap'.

In order to investigate the type and properties of the defects, CL and electron channelling contrast imaging (ECCI) were performed on the same micron-scale area of a GaN thin film. A one-to-one correlation between isolated dark spots in CL and threading dislocations (TDs) in ECCI showed that TDs of pure edge character and TDs with a screw component act as non-radiative recombination centres.

Secondary electron imaging of planar InGaN/GaN multiple quantum well (MQW) structures identified trench defects of varying width. CL imaging revealed a strong redshift (90 meV) and intensity increase for trench defects with wide trenches compared with the defect-free surrounding area. Narrower trench defects showed a small redshift (10 meV) and a slight reduction in intensity.

The optical properties of nanorods fabricated from planar InGaN/GaN MQW structures were investigated using PL and CL. PL spectroscopy identified reduced strain within the MQW stack in the nanorods compared with the planar structure. CL imaging of single nanorods revealed a redshift of 18 meV of the MQW emission along the nanorod axis and provided an estimate of 55 nm for the carrier diffusion length.

Colour conversion using novel organic compounds as energy down-converters was studied. The first molecules absorbed in the ultra-violet and emitted in the

yellow spectral region. Further modification of the organic compound shifted the absorption into the blue and white light generation was investigated by coating blue-emitting nanorods and blue LEDs. Determination of the colour rendering index and colour temperature showed “warm white” light emission with values of 70 and 3220 K, respectively.

Zusammenfassung

In dieser Arbeit werden die optischen Eigenschaften von III-Nitrid Halbleitermaterialien mittels hyperspektraler Kathodolumineszenz- (CL), Photolumineszenz- (PL) und Elektrolumineszenz-Spektroskopie untersucht.

III-Nitrid Halbleiter haben erfolgreich den Markt für Festkörper-Beleuchtung geöffnet. Leuchtdioden (*light-emitting diodes*, LEDs) basierend auf diesem Materialsystem haben jedoch zahlreiche Mängel, wie zum Beispiel hohe Defektdichten, Leistungsabfälle unter hohen Stromdichten (*efficiency droop*) und der sogenannten 'grünen Lücke' (*green gap*).

CL- und Elektronenkanalisierungskontrast-Messungen (*electron channelling contrast imaging*, ECCI) wurden zur Untersuchung des Typs und der Eigenschaften von Defekten durchgeführt. Die Messungen wurden an einem identischen Mikrometer großen Bereiches einer GaN Schicht ausgeführt. Eine eineindeutige Beziehung zwischen isolierten Bereichen geringer Intensität in CL Bildern und Fadenversetzungsdichten in ECCI zeigte, dass Stufenversetzungen und Versetzungen mit einem Schraubenanteil, Zentren für strahlungslose Übergänge darstellen.

Sekundärelektronenmikroskopie von ebenen InGaN/GaN Vielfachquantentöpfen zeigte die Präsenz von ringförmingen Vertiefungen mit unterschiedlichen Breiten. CL-Messungen zeigte eine starke Rotverschiebung (90 meV) und Intensitätssteigerung von breiten Vertiefungen und eine kleine Rotverschiebung (10 meV) und eine geringfügige Intensitätsreduzierung von schmaleren Vertiefungen.

Die optischen Eigenschaften von Nanostäbchen, welche aus oben genannten ebenen InGaN/GaN Vielfachquantentöpfen hergestellt wurden, wurden mittels CL- und PL-Spektroskopie analysiert. PL-Messungen stellten eine reduzierte Verspannung innerhalb der Vielfachquantentopfstruktur der Nanostäbche im Vergleich zur eben Struktur fest. CL-Messungen eines einzelnen Nanostäbchen zeigte

eine 18 meV Rotverschiebung der Emission des Vielfachquantentopfes entlang der Achse des Nanostäbchens und Berechnung der Ladungsträgerausbreitung ergab einen Wert von 55 nm.

Farbkonvertierung wurde mittels eines neuwertigen organischen Stoffes zur Energieumwandlung untersucht. Die ersten Moleküle absorbierten im ultravioletten und emittierten im gelben Spektralbereich. Modifizierung der chemischen Struktur des organischen Stoffes verschob die Absorptionslinie in den blauen Spektralbereich. Die Umwandlung zu weißem Licht wurde mittels blauen LEDs und blau emittierenden Nanostäbchen untersucht, welche mit dem organischen Material beschichtet wurden. Bestimmung des Farbwiedergabeindexes und Farbtemperatur ergab Werte von 70 bzw. 3220 K, welche warm weißem Licht entsprechen.

Acknowledgments

This is the moment where I would like to extend my gratitude and thanks to all the people who helped and supported me during the course of my PhD.

First and foremost I would like to thank my *Doktorvater* **Prof. Rob Martin**, who provided me with guidance, support and advise throughout my research. His constant encouragement and patience made me always look forward and this work would not have been possible without it.

Thank you to **Prof. Kevin O'Donnell** for his vast knowledge in spectroscopy and making a conference visit an educating experience.

I am very grateful to **Dr. Carol Trager-Cowan** for her inexhaustible readiness to help in every kind of situation and her support and guidance throughout the last few years.

I would like to thank **Dr. Paul Edwards**, who taught me the art of cathodoluminescence and his near unlimited patience whenever I broke something, which he needed to fix afterwards. In addition, he introduced me to the ~~English~~ British culture, etiquette and way of life.

Dr. Ben Hourahine, who always shared his knowledge and advice in countless discussions.

I would also like to extend a big thank you to **Dave Clark**, who is the one with the right tools to build and fix anything imaginable. His resourcefulness and kind and caring manner towards PhD students is exceptional.

My collaborators in the Department of Pure & Applied Chemistry, who are **Prof. Pete Skabara**, **Dr. Neil Findlay** and **Dr. Anto R. Inigo**, I would like to thank for developing and synthesising the organic materials used and their support.

Another big thank you goes to all the people, who have provided me with samples during the course of my PhD. Firstly, there is **Prof. Tao Wang**,

Dr. Jie Bai, **Paul Renwick**, **Rick Smith**, and **Yipin Gong** at the University of Sheffield, who constantly provided me with custom-grown planar InGaN/GaN samples and specially fabricated nanorods. Secondly, **Dr. Duncan Allsopp**, **Dr. Philip Shields** and **Yiding Zhuang** at the University of Bath for various blue LEDs and nanorods. Lastly, **Dr. Lata Sahonta**, **Dr. Menno Kappers**, **Dr. Ted Thrush** and **Dr. Rachel Oliver** at the University of Cambridge for the 'trench-infested' material and various LEDs.

For the financial support I would like to acknowledge **EPSRC** and the **University of Strathclyde**.

The remaining people in my group **Michael**, **Simon**, **Naresh**, **Elaine**, **Martin**, **Franziska**, **Mike**, **Lethy**, **Gunnar**, **Nouf**, **Stefano** and **Fathi**, I would like to thank for an always interesting and entertaining time on Level 2 around the coffee table.

My friends, **Nikhil**, **Aline**, **Ina**, **Katrin**, **Jeni** and **David**, who haven't been mentioned above, for countless hiking, camping, climbing trips throughout Scotland and other interesting adventures, which made the last few years here enjoyable. As it turned out most of them–as it happened by coincidence–are in my group or just an earshot away somewhere else in the Department of Physics.

I would also like to thank my parents, **Maria** and **Helmut**, for their continued support throughout my entire studies; especially my mom to whom I dedicate this work.

Finally, **Lada** for her love, support and belief in me to achieve my aims.

Jochen Bruckbauer Glasgow, 9th July, 2013

List of publications

1. J. Bruckbauer, P. R. Edwards, T. Wang and R. W. Martin: *"High resolution cathodoluminescence hyperspectral imaging of surface features in InGaN/GaN multiple quantum well structures"*, Appl. Phys. Lett. **98**, 141908 (2011)

2. P. R. Edwards, L. K. Jagadamma, J. Bruckbauer, C. Liu, P. Shields, D. Allsopp, T. Wang and R. W. Martin: *"High-resolution cathodoluminescence hyperspectral imaging of nitride nanostructures"*, Microsc. Microanal. **18**, 1212 (2012)

3. N. J. Findlay, C. Orofino-Peña, J. Bruckbauer, S. E. T. Elmasly, S. Arumugam, A. R. Inigo, A. L. Kanibolotsky, R. W. Martin, and P. J. Skabara, *"Linear oligofluorene-BODIPY structures for fluorescence applications"*, J. Mater. Chem. C **1**, 2249 (2013)

4. G. Naresh-Kumar, C. Mauder, K. R. Wang, S. Kraeusel, J. Bruckbauer, P. R. Edwards, B. Hourahine, H. Kalisch, A. Vescan, C. Giesen, M. Heuken, A. Trampert, A. P. Day, and C. Trager-Cowan, *"Electron channeling contrast imaging studies of nonpolar nitrides using a scanning electron microscope"*, Appl. Phys. Lett. **102**, 142103 (2013)

5. Y. D. Zhuang, S. Lis, J. Bruckbauer, S. E. J. O'Kane, P. A. Shields, P. R. Edwards, J. Sarma, R. W. Martin, and D. W. E. Allsopp, *"Optical Properties of GaN Nanorods Containing a Single or Multiple InGaN Quantum Wells"*, Jpn. J. Appl. Phys. **52**, 08JE11 (2013)

6. J. Bruckbauer, P. R. Edwards, J. Bai, T. Wang and R. W. Martin: *"Probing light emission from quantum wells within a single nanorod"*, Nanotechnology, submitted

7. J. Bruckbauer, P. R. Edwards, S.-L. Sahonta, F. C.-P. Massabuau, M. J. Kappers, C. J. Humphreys, R. A. Oliver, and R. W. Martin, *"Cathodoluminescence hyperspectral imaging of trench-like defects in InGaN/GaN quantum well structures"*, Nanotechnology, submitted

8. G. Naresh-Kumar, J. Bruckbauer, P. R. Edwards, S. Kraeusel, B. Hourahine, R. W. Martin, M. J. Kappers , M. J. Moram, S. Lovelock, R. A. Oliver, C. J. Humphreys, and C. Trager-Cowan, *"Coincident electron channeling and cathodoluminescence studies of threading dislocations in GaN"*, Microsc. Microanal., submitted

9. N. J. Findlay, J. Bruckbauer, A. R. Inigo, S. Arumugam, R. W. Martin, and P. J. Skabara, *"An organic down-converting material for hybrid white-light emission"*, in preparation

Contents

List of abbreviations

AFM	Atomic force microscope
AlN	Aluminium nitride
BSE	Backscattered electron
BSF	Basal plane stacking fault
B–W	Black–white
CL	Cathodoluminescence
CRI	Colour rendering index
CCT	Correlated colour temperature
ECCI	Electron channelling contrast imaging
EL	Electroluminescence
EQE	External quantum efficiency
FWHM	Full width at half maximum
GaN	Gallium nitride
InGaN	Indium gallium nitride
InN	Indium nitride
IQE	Internal quantum efficiency
LD	Laser diode
LED	Light-emitting diode
LO	Longitudinal optical
MBE	Molecular beam epitaxy
MOCVD	Metal-organic chemical vapour deposition
MOVPE	Metal-organic vapour phase epitaxy
MQW	Multiple quantum well
PL	Photoluminescence
SE	Secondary electron

SEM	Scanning electron microscope
SMB	Stacking mismatch boundary
SSL	Solid-state lighting
SQW	Single quantum well
TD	Threading dislocation
TEM	Transmission electron microscope
UV	Ultra-violet
QW	Quantum well

Chapter 1

Introduction

Electric lighting was invented over 130 years ago and the incandescent light bulb still is the main source for light in this current day and age; the technology though has barely improved over the last century. Current estimates show that 19–21% of the global electricity consumption is used for electric lighting [1, 2], which is an alarmingly high number because of the inefficiency of current light sources. Because of this inefficiency lighting is responsible for a considerable contribution to the present energy wastage. An implication is the emission of greenhouse gases since a large amount of the energy is produced by burning fossil fuels [3]. It is clear that new and more energy-efficient light sources must be developed when the global need to conserve energy supplies and the threat of global warming are considered.

Contrary to common belief, the incandescent light bulb was not invented by Thomas Edison, but he successfully commercialised the first practical light bulb. Earlier designs for incandescent lights, however, were patented by English physicist and chemist Sir Joseph Swan around 1860–80 [4, 5]. This ambiguity led to various patent law suits. Electricity is passed through a tungsten wire in a evacuated glass bulb, which heats up and emits light. The light bulb is extremely inefficient in converting electrical power into light. Although, it emits light across the visible spectrum, a considerable fraction is also emitted in the infrared as heat, which accounts for 95% of the consumed power. Significant improvements are achieved by using fluorescent tubes with an efficiency of about 25%. An additional drawback, however, is the use of toxic material (mercury),

which poses an environmental hazard upon disposal.

In 1962 the first visible light-emitting diode (LED) was introduced by Holonyak et al. and was made of a GaAsP p-n junction emitting in the red [6]. Soon after his discovery he envisioned that it should be possible to create an LED emitting white light [7]. This paved the way for what is now known as *solid-state lighting* (SSL). SSL is mainly based on inorganic LEDs using semiconductors, such as the III-nitride material system, and organic LEDs (OLEDs), which utilise light emission from polymers, small molecules or organic thin films [8]. There are, however, remaining challenges for white LEDs, which are their higher cost and their lower light output compared with current conventional light sources [9]. Haitz's law, similar to Moore's law for transistors, describes the light flux per lamp and the cost per lumen over the last 40 years [10]. The trend showed a cost decrease by a factor of 10 per decade, whilst the light flux increased by a factor of 20. This predicts a bright future for white LEDs. Reviews on SSL can be found in Refs. [11, 3, 12].

The material systems most suitable for LEDs, emitting at different colours, are the III-nitrides and their compounds due to their flexibility to emit light over the entire visible spectrum and beyond. Over two decades ago two major advances revolutionised the III-nitride field. First, a drastic improvement of the crystal quality was achieved by using an aluminium nitride (AlN) buffer layer [13, 14, 15]. Second, effective p-type doping using magnesium (Mg) was realised using either low-energy electron beam irradiation or thermal annealing for activation of the Mg dopant [16, 17]. Building on these advancements Nakamura et al. fabricated the first high-brightness blue LED in 1994 at Nichia Chemical Industries [18].

Alloying gallium nitride (GaN) with indium nitride (InN) or AlN to form ternary and quaternary compounds, such as $In_xGa_{1-x}N$, $Al_yGa_{1-y}N$, $Al_zIn_{1-z}N$, $Al_yIn_xGa_{1-x-y}N$, it is possible to achieve light emission from the infrared, through the visible to the ultraviolet (UV) spectral region. This makes them attractive for opto-electronic devices, e.g. LEDs and laser diodes (LDs) [18, 19]. The first III-nitride LEDs were heterojunctions, double heterostructures and then multiple quantum well (MQW) structures were developed for increased light emission [20]. The main application for these light emitters is SSL, which includes room lighting, traffic lights, street lights, backlighting of screens, vehicle headlights, general illumination and many more [21]. Further uses in other areas are water

purification [22], data storage (Blu-ray technology) [23], colour printing, solar blind UV detectors [24], biosensors [25] and solar cells [26]. Additional properties of GaN, such as its wide band gap, high temperature stability, inertness to corrosive chemicals and high breakdown voltages, also make this material system a favoured option for high-power/high-frequency electronics or applications in challenging environments [27, 28, 29].

In late 1959 Richard Feynman gave a lecture entitled *"There's Plenty of Room at the Bottom"*, where he considered the possibility to manipulate individual atoms or the construction of a nanomotor [30]. It took more than another decade, however, before the term *nanotechnology* started to evolve [31]. In the field of III-nitrides, nanostructures have become of interest due to their ability to increase the efficiency of opto-electronic devices based on MQW structures [32, 33]. InGaN/GaN nanorods have been realised with emission wavelengths from the blue to the red spectral region making them attractive for white LEDs [34, 35]. Other applications employing nitride-based nanostructures include photonic crystals [36] and various sensors for chemical or biological species [37, 38, 39].

In this work, the luminescence characteristics and behaviour of III-nitride epitaxial layers, planar MQW structures, nanostructures containing MQWs and LEDs are investigated.

After a short introduction to the III-nitride system and its structures and devices in *Chapter 2*, the experimental methods used in this thesis are described in *Chapter 3*. In *Chapter 4* three techniques (cathodoluminescence, electron channelling contrast imaging and atomic force microscopy) are combined to investigate the luminescence behaviour of threading dislocations in a GaN thin film. The optical characteristics of planar InGaN/GaN MQW structures and defects on their surfaces are studied in *Chapter 5*. These structures were used to fabricate nanorods whose luminescence was characterised by cathodoluminescence hyperspectral imaging and photoluminescence spectroscopy in *Chapter 6*. White light emission from blue LEDs and blue-emitting nanorods coated with a newly-synthesised organic compound emitting yellow light was investigated in *Chapter 7*. Finally, *Chapter 8* gives a summary of the main results of this thesis and suggestions for future work are proposed.

Chapter 2

Background

2.1 Properties of III-nitrides

The group III-nitride system has gained a lot of interest due to the tuneable band gap of the ternary and quaternary alloys of GaN, AlN and InN. The band gap ranges from the UV for AlN through the visible spectrum to the near infrared spectrum for InN. Fig. 2.1 shows the room temperature band gap of hexagonal AlN, GaN and InN plotted against their a lattice constant, which is the in-plane lattice constant important for the growth as explained later in this section. When alloying GaN with AlN or InN to grow a ternary alloy such as $In_xGa_{1-x}N$, the band gap E_g does not change linearly with composition. Band gap bowing can be empirically approximated by the following equation with a constant term, a linear term proportional to the composition x, and a quadratic term proportional to $x(1-x)$ whose coefficient b is termed bowing parameter:

$$E_g^{AB} = E_g^A + x \cdot \left(E_g^B - E_g^A\right) + bx\,(1-x)\,. \tag{2.1}$$

For $In_xGa_{1-x}N$ the equation was determined to be [40]

$$E_g^{InGaN} = 3.42\text{ eV} - x \cdot 2.65\text{ eV} - 2.4\text{ eV} \cdot x(1-x). \tag{2.2}$$

GaN is a direct gap semiconductor with a wide band gap. The conduction band minimum and valence band maximum, which is split into three sub-bands, are located at the Γ-point with a separation of 3.42 eV for the wurtzite structure at

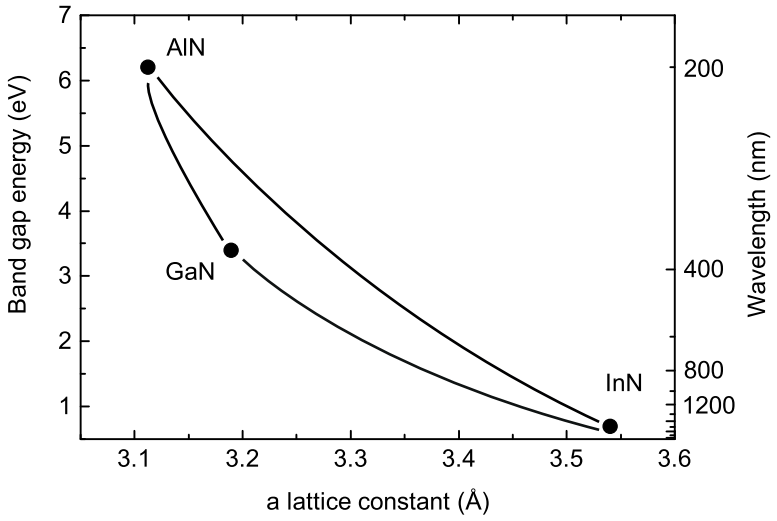

Figure 2.1: *Band gap E_g versus a lattice constant of hexagonal AlN, GaN and InN at room temperature. Band gap bowing is schematically shown by solid lines.*

room temperature. The hexagonal symmetry of the wurtzite structure causes the crystal field splitting leading to the split-off band C. Furthermore, the degeneracy of the upper valence band is lifted by the spin-orbit coupling, which splits the heavy and light hole band into the A and B bands. Fig. 2.2 shows a simplified diagram of the band structure of GaN at the Γ-point. The energy split due to spin-obit coupling is much smaller than the split due to the influence of the crystal field in III-nitrides [41]. The curvature of a given band in the band structure defines the effective masses of electrons and holes with a strong (weak) curvature resulting in a small (large) effective mass. The values for the effective masses are $m_e = 0.2m_0$ for the electron, $m_{hh} = 1.4m_0$ for the heavy hole, $m_{lh} = 0.3m_0$ for the light hole and $m_{so} = 0.6m_0$ for electrons in the split-off band with m_0 being the electron mass [42].

When an electron is removed from the valence band and promoted across the band gap it leaves a hole behind. These two particles can be bound together via the Coulomb interaction creating an exciton. The A exciton binding energy in GaN, where the hole originates in the A valence band, can be measured by different techniques and is between 20–30 meV [43, 44]. Since the binding energy is of the order of the thermal energy at room temperature (≈25 meV), free excitonic

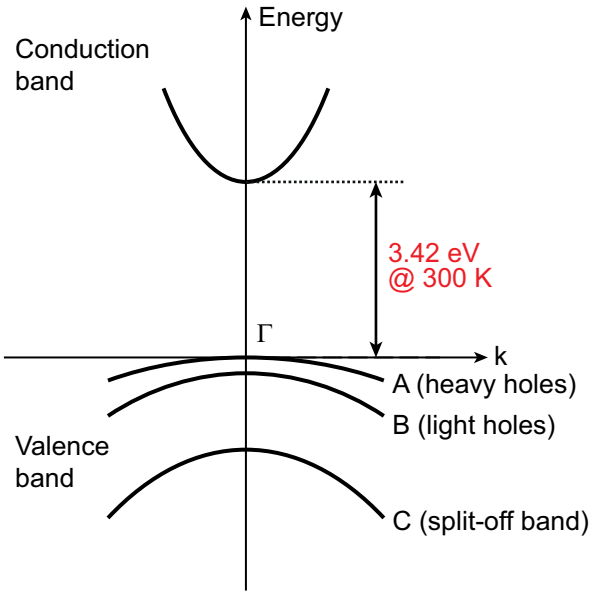

Figure 2.2: *Simplified diagram of the band structure of GaN at the Γ-point showing the split of the valance band into three sub-bands due to the crystal field and spin-orbit coupling.*

emission can be observed at room temperature. Photoluminescence (PL) spectra of GaN exhibit periodically spaced peaks on the low-energy side. GaN, being a polar material, exhibits a strong interaction between excitons and longitudinal optical (LO) phonon via the Fröhlich polar interband scattering [45]. This leads to so-called phonon replicas, which appear as periodically spaced low energy peaks in a GaN PL spectrum. The LO phonon energy in GaN is 92 meV [46], whereas InGaN MQW structures exhibit a slightly reduced LO phonon energy of 89 meV [47].

III-nitrides possess two possible crystal structures, the thermodynamically stable hexagonal wurtzite structure and the metastable cubic zincblende structure. A section of the wurtzite structure conventionally used to illustrate the symmetry elements is shown in Fig. 2.3(a) containing six Ga and six N atoms. It is described by the a and c lattice constants, with a being the length of one of the six sides of the hexagon in the basal plane and c being the height of the hexagon. Each Ga or N atom is surrounded by four atoms of the other kind forming a tetrahedral bonding structure (Fig. 2.5). This arrangement of atoms

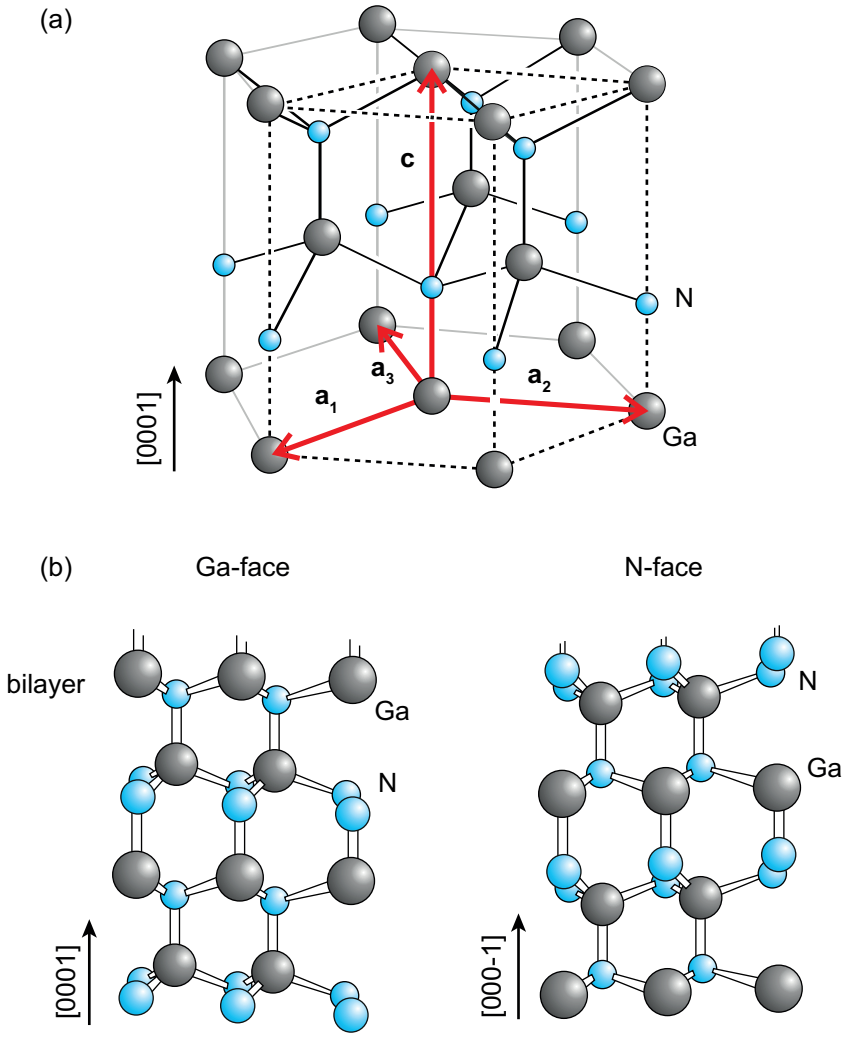

Figure 2.3: *(a) Illustration of the wurtzite structure of GaN. The unit cell is marked by dashed lines. (b) Polarities of wurtzite GaN: Ga-face (or* [0001] *polarity) and N-face (or* [000$\bar{1}$] *polarity).*

results in a Ga–N bilayer as seen in Fig. 2.3(b) along the c direction. The bilayer consists of two close-spaced hexagonal layers of Ga and N atoms. Due to the lack of an inversion symmetry the wurtzite structure is a polar material. The reason for the missing inversion symmetry is the presence of the Ga–N bilayer. By convention the [0001] direction (or c direction) is given by a vector pointing from a Ga atom to the nearest neighbouring N atom. This leads to two different polar directions depending on which atom is on top of the bilayer. This in particular is

Material	a_0 (Å)	c_0 (Å)	E_g (eV) @ 300K
AlN	3.112	4.982	6.2
GaN	3.189	5.185	3.4
InN	3.54	5.705	≈0.7

Table 2.1: *a and c lattice constants and room temperature band gaps of the AlGaInN material system. Parameters taken from Ref. [50]. InN band gap taken from Ref. [51].*

of importance for materials which are grown along the c direction. If Ga (N) is in the top position the material is considered to be Ga-face (N-face) or of [0001] ($[000\bar{1}]$) polarity as seen in Fig. 2.3(b). High quality GaN on c-plane sapphire grown by metal-organic chemical vapour deposition commonly exhibits Ga-face surfaces, whereas growth by molecular beam epitaxy typically results in N-face surfaces [48, 49].

Both lattice constants and the band gaps of the AlGaInN system are summarised in Tab. 2.1.

2.2 Quantum confinement

Common structures for opto-electronic devices are single quantum wells (SQWs) and MQWs. A quantum well (QW) structure is fabricated by growing alternating layers of a few nanometers of material with different band gaps and (preferably) similar in-plane lattice constants. Common materials based on the III-nitride system are InGaN/GaN with InGaN as the well layer and GaN as the barrier due to its higher band gap or GaN/AlGaN, where the high band gap AlGaN layer constitutes the barrier.

The one dimensional infinite potential well gives a simple, descriptive approximation for the dependency of the transition energy on the width of the well and the quantisation of energy levels. In this case the potential of width d has the following form

$$V(x) = \begin{cases} 0 & 0 < x < d \\ \infty & x > d \ \wedge \ x < 0 \end{cases} \tag{2.3}$$

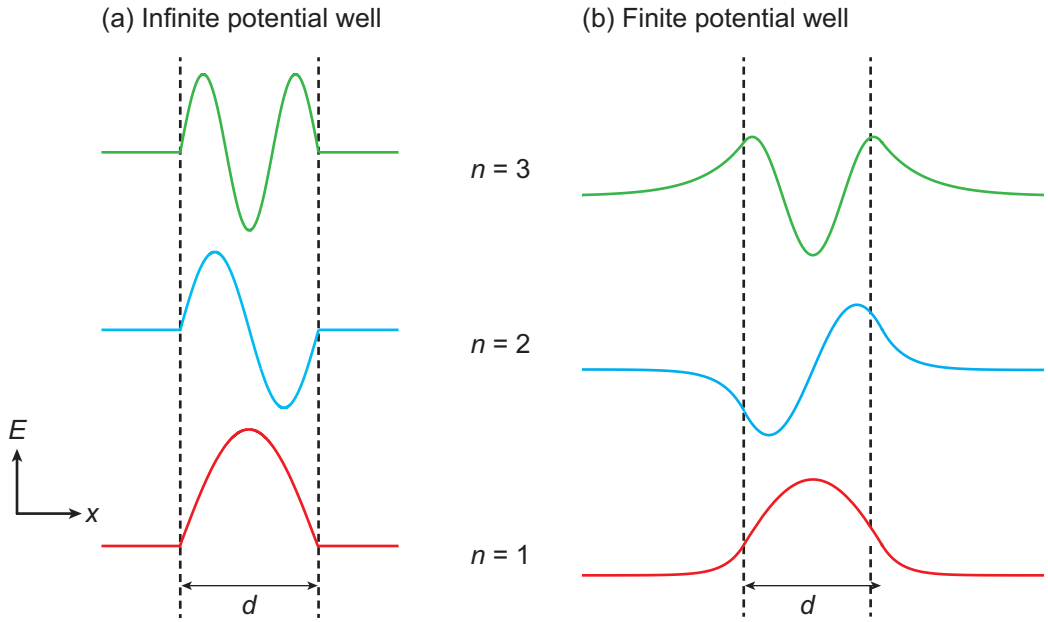

Figure 2.4: *Solutions for the wave functions for the one dimensional time-independent Schrödinger equation for an (a) infinite potential and (b) finite potential well. The solutions are shown for $n = 1 - 3$. In case of a finite potential the wave functions exhibit an exponential decay outside the well.*

with boundary conditions $\psi(0) = 0$ and $\psi(d) = 0$. These boundary conditions forbid states outside the potential. This system can be described using the time-independent Schrödinger equation in one dimension

$$\left(-\frac{\hbar^2}{2m}\frac{d^2}{dx^2} + V(x)\right)\psi(x) = E\psi(x). \tag{2.4}$$

with the reduced Planck constant $\hbar$ and the mass m of the particle. The solutions of the Schrödinger equation considering the boundary conditions and an Ansatz using plane waves result in a quantisation of allowed energy levels. The solutions for the energy levels E_n and wave functions $\psi_n(x)$ are

$$E_n = \frac{\hbar^2 k_n^2}{2m} = \frac{\hbar^2\pi^2}{2m}\cdot\frac{n^2}{d^2}, \qquad \psi_n(x) = \sqrt{\frac{2}{d}}\sin\frac{n\pi x}{d} \tag{2.5}$$

with the wavenumber k_n and $n = 1, 2, 3, \ldots$.

The quantised energy is indirectly proportional to the squared well width d, so

for a decreasing well width the allowed energy levels are shifted to higher energies. The solutions for the wave function for $n = 1 - 3$ of the infinite potential well are displayed in Fig. 2.4(a). However, an infinite well is an unrealistic description. A real structure, where the potential well is formed by a lower band gap semiconductor is better described by a finite potential well approach. Due to the finite barriers there is a non-vanishing probability of finding carriers outside the potential well. This problem cannot be solved analytically, but a graphical or numerical approach is used. Fig. 2.4(b) shows the solutions for the wave functions for the finite potential well. Compared to infinite barriers the wave functions exhibit an exponential decay into the barrier and the energy levels are slightly lower.

2.3 Polarisation and quantum-confined Stark effect

An important property of III-nitrides with the wurtzite structure is the presence of spontaneous and piezoelectric polarisation. Because of the crystal structure both types of polarisation only exist along the $\pm c$ direction. Orientations are very important when dealing with polarisation, i.e. the polarisation depends on growth direction, type of strain and polarity (Ga- or N-face) of the material. Opto-electronic devices are strongly influenced by the polarisation as will be explained in the following.

The spontaneous polarisation is an intrinsic property caused by deviations from the ideal crystal structure. In an ideal wurtzite crystal the ratio of the lattice constants is $\frac{c}{a} = \sqrt{\frac{8}{3}} = 1.633$. Calculated values of this ratio for AlN, GaN and InN are given in Tab. 2.2 using the relaxed lattice constants a_0 and c_0. The observed spontaneous polarisation is caused by a deviation of less than 1% from the ideal c/a ratio. Fig. 2.5 shows a schematic representation of the origin of the spontaneous polarisation. It shows one Ga atom tetragonally bound to four neighbouring N atoms. The polarity is Ga-face, defining the direction of the polarisation. The contributions from the bottom three polarisations ($\mathbf{P}_{2,\perp} - \mathbf{P}_{4,\perp}$) in the basal plane compensate each other, whereas the parallel components ($\mathbf{P}_{2,\parallel} - \mathbf{P}_{4,\parallel}$) together with $\mathbf{P}_1$ form a non-vanishing polarisation along the $[000\bar{1}]$

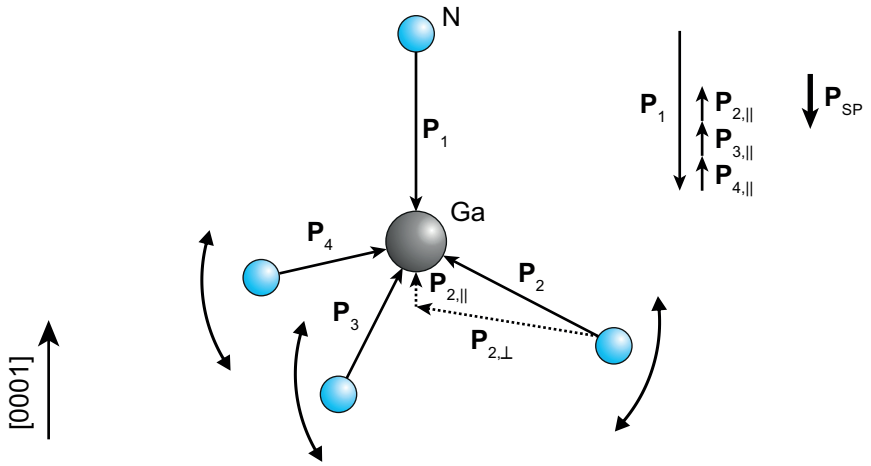

Figure 2.5: *Origin of the spontaneous polarisation. One Ga atom is surrounded by four tetragonal bounded N atoms. The polarity is Ga-face. The arrows on the right show the ratio of the polarisation contributing to the non-vanishing polarisation along the c direction.*

direction pointing away from the surface. In the case of N-face the direction of the spontaneous polarisation would be towards the surface. The values for the spontaneous polarisation for the III-nitrides are all negative and are summarised in Tab. 2.2. It should be noted that the piezoelectric constants are up to ten times larger for nitrides than for conventional III–V and II-VI materials. The spontaneous polarisation in nitrides is found to be negative, very large, and only 3–5 times smaller than in ferroelectric perovskites and comparable to II–VI oxides, such as ZnO [52, 53]. AlN has the largest spontaneous polarisation and it increases from GaN to InN and AlN.

The second contribution to the total polarisation comes from the strain-induced piezoelectric polarisation. Piezoelectric polarisation occurs in (0001)-orientated heterostructures, such as SQW or MQW structures, where each of the layers are grown pseudomorphically on top of each other. Pseudomorphic means that the top layer adopts the in-plane or a lattice constant of the layer it is grown upon, which leads to tensile or compressive strain in the top layer. This strain is biaxial and perpendicular to the c direction.

The piezoelectric tensor of the wurtzite system has three non-vanishing (independent) components e_{15}, e_{31} and e_{33}. The e_{15} component is related to the

Material	c_0/a_0	P_{SP} (C/m^{-2})	e_{31} (C/m^{-2})	e_{33} (C/m^{-2})
AlN	1.6190	-0.081	-0.60	1.46
GaN	1.6336	-0.029	-0.49	0.73
InN	1.6270	-0.032	-0.57	0.97
AlAs			0.01	-0.01
GaAs			0.06	-0.12
InAs			0.01	-0.03
AlP			-0.02	0.04
GaP			0.03	-0.07
InP			-0.02	0.04

Table 2.2: *Calculated c_0/a_0 parameter using the relaxed values for the lattice constants and spontaneous polarisation P_{SP} for the wurtzite AlGaInN system. Calculated values for the piezoelectric constants e_{31} and e_{33} for the wurtzite III-nitride, zincblende phosphide and arsenide material system. Taken from Ref. [52].*

polarisation induced by a shear strain and will not be considered here. Using the e_{31} and e_{33} components leads to the following expression for the piezoelectric polarisation

$$P_{\mathrm{PE}} = e_{31}\left(\varepsilon_x + \varepsilon_y\right) + e_{33}\varepsilon_z \tag{2.6}$$

with a_0 and c_0 being relaxed values for the lattice constants, $\varepsilon_z = (c - c_0)/c_0$ the strain along the c direction and $\varepsilon_x = \varepsilon_y = (a - a_0)/a_0$ the strain in the basal plane, which is expected to be isotropic [52]. Calculated values for for the piezoelectric constants e_{31} and e_{33} for the III-nitride materials are quite high. Tab. 2.2 shows a comparison between the piezoelectric constants of the III-nitrides with those of the phosphide and arsenide material systems, which exhibit a zincblende crystal structure. The relationship between the lattice parameters for wurtzite GaN can be expressed as

$$\frac{c - c_0}{c_0} = -2\,\frac{C_{13}}{C_{33}}\frac{a - a_0}{a_0} \tag{2.7}$$

with elastic constants C_{31} and C_{33} [50]. Inserting Eq. (2.7) into Eq. (2.6) leads

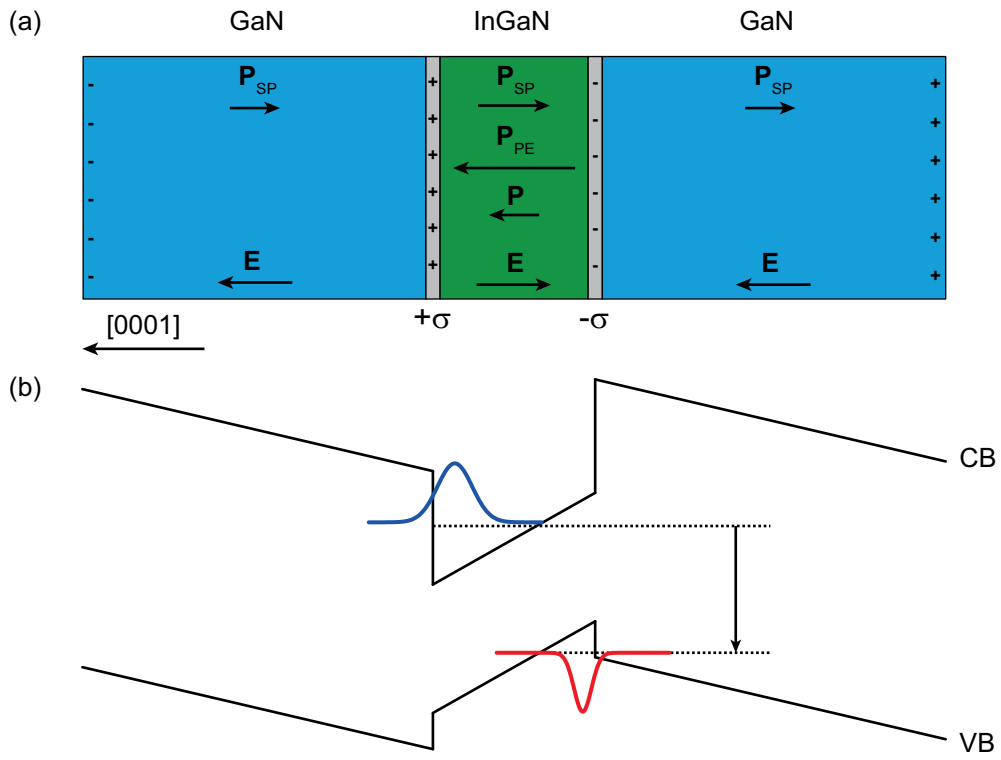

Figure 2.6: *(a) Schematic of a Ga-polar InGaN/GaN quantum well structure. The directions of spontaneous and piezoelectric polarisations and the internal electric fields are marked. (b) Resultant band diagram showing the influence of the internal electric fields.*

to the following expression for the piezoelectric polarisation

$$P_{\mathrm{PE}} = 2\,\frac{a - a_0}{a_0}\left(e_{31} - e_{33}\frac{C_{13}}{C_{33}}\right). \tag{2.8}$$

The expression in round brackets in Eq. (2.8) is < 0 for the entire composition range of AlGaN, InGaN and AlInN. This means that the direction of the piezoelectric polarisation is determined by the in-plane lattice constant (a lattice constant), which is governed by strain. For compressive strain the piezoelectric polarisation is positive and for tensile strain negative. The total polarisation P is simply the vector sum of spontaneous and piezoelectric polarisation

$$P = P_{\mathrm{SP}} + P_{\mathrm{PE}}. \tag{2.9}$$

Fig. 2.6(a) shows a Ga-polar InGaN/GaN quantum well structure, where the InGaN well layer is compressively strained. It shows the directions of the spontaneous polarisation in the three layers as well as the strain-induced piezoelectric polarisation in the InGaN layer. Since the strain is compressive the piezoelectric polarisation points in the opposite direction to the spontaneous polarisation.

The difference in polarisation between each of the two interfaces results in a gradient of the polarisation. This change of polarisation induces a fixed sheet charge density at the two interfaces with opposing charge given by

$$\begin{aligned} \sigma(P_{\mathrm{SP}} + P_{\mathrm{PE}}) &= P(\mathrm{bottom}) - P(\mathrm{top}) \\ &= P_{\mathrm{SP}}(\mathrm{bottom}) - [P_{\mathrm{SP}}(\mathrm{top}) + P_{\mathrm{PE}}(\mathrm{top})]\,. \end{aligned} \tag{2.10}$$

These sheet charges give rise to an internal electric field causing the band structure to tilt. Fig. 2.6(b) shows the resulting band diagram where band bending of the GaN and InGaN layers was caused by their opposing electric fields. These electric fields can reach strengths from a few 100 kV/cm up to a few MV/cm in InGaN/GaN quantum well structures [54].

The internal electric fields have a detrimental influence on the emission properties of a QW structure. This is known as the *quantum-confined Stark effect* (QCSE). The emission energy is redshifted, the radiative recombination time is increased and the emission peak is broadened. The electric field causes a spatial separation of electron and holes inside the quantum well. Because of this separation a reduced overlap of the electron and hole wave functions occurs leading to a reduced radiative recombination time or increased excitonic lifetime. The decreased emission energy (redshift) is simply caused by band bending forming triangular wells. These two effects are illustrated in Fig. 2.7 where the flat band condition without any internal electric field is shown next to the case for an electric field along the [0001] direction. In the wurtzite structure the internal electric field can only occur in the $\pm c$ direction for the above stated reasons. The flat band condition can be achieved by choosing so-called non-polar directions, which are perpendicular to the c direction, because no polarisation fields exist in these directions. Possible directions are $\langle 11\bar{2}0 \rangle$ and $\langle 1\bar{1}00 \rangle$, which correspond to the a- and m-planes.

The strength of the QCSE is influenced by different material parameters,

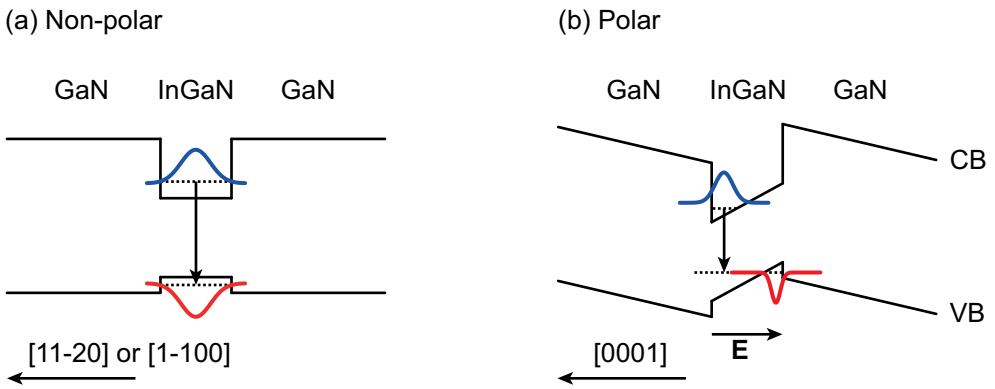

Figure 2.7: *Band structure for (a) non-polar and (b) polar directions in a InGaN/GaN quantum well. The polar direction is parallel to the c direction, whereas non-polar directions are perpendicular to it, such as* $\langle 11\bar{2}0 \rangle$ *and* $\langle 1\bar{1}00 \rangle$*. Electron and hole wave functions are drawn to show the influence of the internal electric fields, which causes a spatial separation of the charge carriers.*

such as well width, composition and of course strain, which is coupled to the composition. With increasing composition the lattice mismatch becomes larger and hence the compressive strain increases as well resulting in a stronger redshift of the emission. Increasing the well width leads to a decrease in the emission energy and a stronger separation of the electron–hole wave functions leading to much larger QCSE-related redshifts.

One of the first reports on the QCSE was described by Miller et al. for GaAs/AlGaAs QW structures [55]. The influence of the QCSE on the optical transition of nitride-based structures has been extensively studied and can be found in Refs. [56, 57, 58].

The presence of the QCSE can be confirmed by measuring PL spectra as a function of laser excitation power. With increasing excitation power more carriers are generated, which screen the internal electric fields. This results in a reduction of the QCSE and the emission energy is blueshifted with increasing excitation power.

2.4 Extended defects

Extended defects in a solid are deviations from the ideal crystal structure and they are classified, according to their dimensionality, into point defects, line defects, planar defects and bulk defects. In a real crystal, such as an epitaxial grown semiconductor, all of these defects can have a crucial influence on the optical and electrical properties.

Point defects are zero-dimensional defects which involve irregularities of single atoms and their lattice sites. A vacancy is an atom missing from its lattice position, while an interstitial constitutes an additional atom on an irregular lattice position. An antisite occurs in compounds or alloys where an atom is located on the lattice site of another atom constituting the compound. Dopants in a semiconductor are common point defects, where the substitution of a regular atom by an impurity atom leads to a change in electrical conductivity.

Dislocations are one-dimensional line imperfections, which may be created for example by a shear stress misplacing a row of atoms in a perfect crystal. Dislocations are classified by two vectors; their line direction $\mathbf{L}$ and their Burgers vector $\mathbf{B}$. The line direction defines the path of the defect through the material, whereas the Burgers vector gives a measure of the crystal deformation caused by the defect. The Burgers vector $\mathbf{B}$ is defined by the following line integral around the defect line $\mathbf{L}$ [59]

$$\mathbf{B} = \oint_C \frac{\partial \mathbf{U}}{\partial s} ds \tag{2.11}$$

with $\mathbf{U}(r)$ being the displacement field, which describes the deviation from the ideal crystal. If $\mathbf{B} \neq 0$ the defect is called a dislocation. Two extreme cases are defined using these two vectors. If the Burgers vector and the line direction are orthogonal the dislocation is called an *edge-type* dislocation. When both vectors are parallel the dislocation is called a *screw-type* dislocation. In all other cases the dislocation is composed of an edge- and screw-component and it is referred to as a *mixed-type* dislocation. An edge dislocation can relax sheer stress perpendicular to its line direction. These dislocations correspond to the addition or removal of part of a lattice plane. For a screw dislocation its strain is in the same direction as the dislocation line and a part of the crystal is moved, but no additional plane is

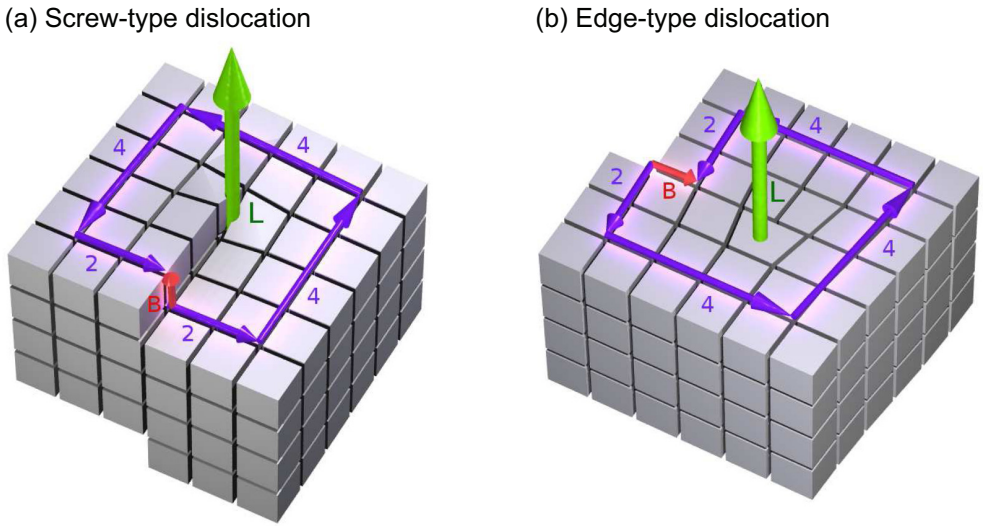

Figure 2.8: *(a) Screw-type and (b) edge-type dislocation in a cubic crystal. The line direction L is shown as a green arrow, the Burgers vector B as a red arrow and the Burgers circuit is shown in purple. Taken from Ref. [60].*

inserted in this case. This results in a spiral in the planes normal to the dislocation line, hence the name screw dislocation. Figs. 2.8(a) and (b) show a schematic of a screw-and edge-type dislocation in a cubic crystal. The line direction **L**, Burgers vector **B** and Burgers circuit, defined by the integral in Eq. (2.11) are also shown.

In III-nitrides *threading dislocations* (TDs) are generated during the growth at the substrate–semiconductor interface due to the large mismatch in lattice constants and thermal expansion coefficients. TDs can propagate (or thread) to the surface and have screw, edge or mixed character [61]. If the dislocation moves parallel to the interface it is referred to as a *misfit dislocation* [62].

Planar defects are two-dimensional defects and include stacking faults and grain boundaries. A *stacking fault* occurs when the periodic stacking sequence is altered. In a hexagonal closed-packed (hcp) structure, such as the wurtzite structure, the stacking order is ABABABAB. Because of the hexagonal symmetry the stacking order could also be BCBCBCBC, which is equivalent to ABABABAB, but rotated by 60°. A stacking fault would occur, for example, when the stacking order changes from AB to AC, such as ABABCBCBC. If the stacking order changes to ABCABCABC the crystal structure is altered from hcp and it becomes face-centred cubic (fcc). A basal plane stacking fault (BSF) propagates

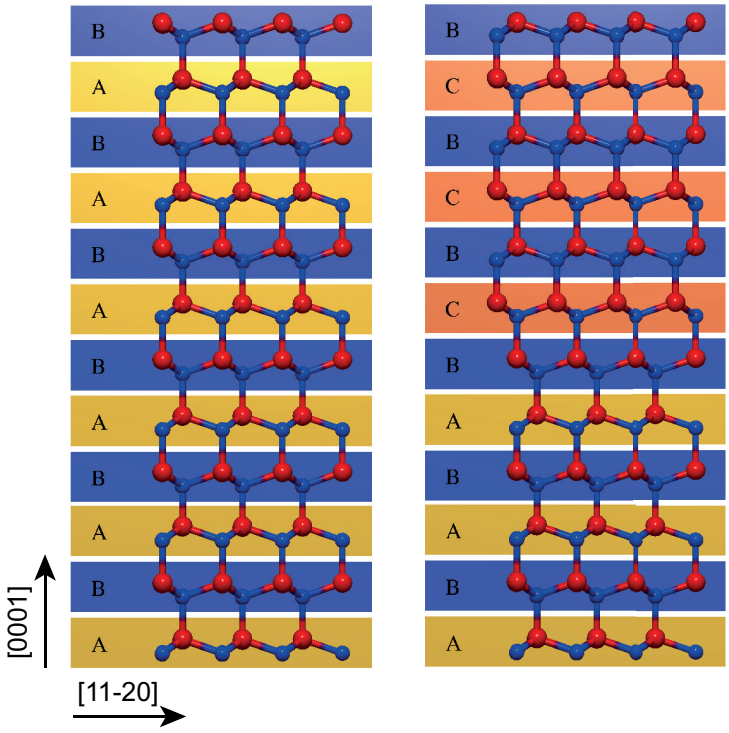

Figure 2.9: *Example of a stacking fault in the wurtzite structure. The stacking sequence is altered from ABABABAB to ABABCBCB along the* [0001] *direction. Image courtesy of S. Kraeusel.*

through the basal plane of the crystal, whereas a prismatic stacking fault (PSF) propagates through a prismatic plane, which is perpendicular to the basal plane. In (0001)-orientated GaN a BSF propagates through the (0001) plane and a PSF through the $(1\bar{1}00)$ plane, for example. An illustration of a stacking fault in the wurtzite structure is shown in Fig. 2.9.

The interface between crystallites of different orientation, which have coalesced during growth, are referred to as *grain boundaries*. The difference in orientation can be caused by a tilt or twist (rotation) of the grains or crystallites [63], as shown in Fig. 2.10. The degree of misorientation classifies them into low-angle ($<10°$) and large-angle grain boundaries [64].

Finally, three-dimensional *bulk defects* consist of voids, where a group of atoms is missing, or clusters of impurities, which are also referred to as precipitates [65].

Further information on extended defects and the theory of dislocations can be found in Refs. [64, 59].

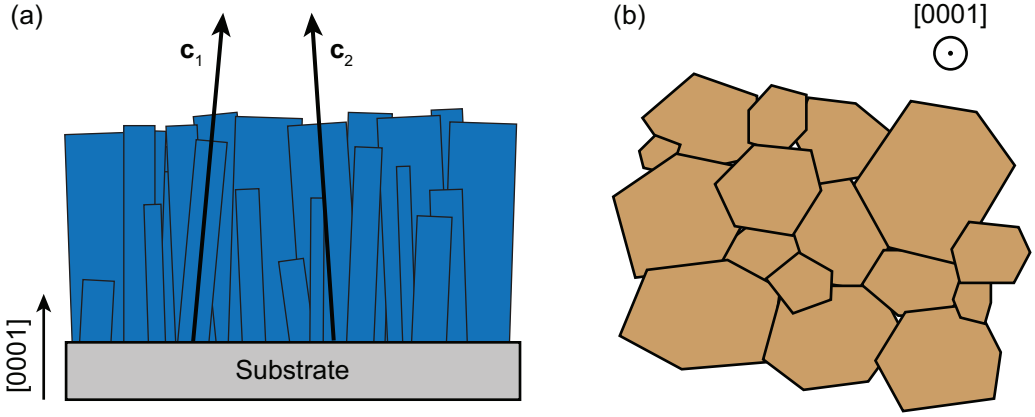

Figure 2.10: *(a) Side view of an epitaxial film with crystallites of different tilt. (b) Top view showing a twist (rotation) of the crystallites causing grain boundaries between these crystallites.*

2.5 Colorimetry and photometry

The "science of colour", or *colorimetry*, describes the quantification and perception of light by the human eye. Unlike other physical quantities, the perception of light is a subjective quantity, depending strongly on each individual. To standardise the measurement of colours, the *Commission Internationale de l'Eclairage* (CIE, International Commission for Illumination) has introduced the *chromaticity diagram* [66].

The chromaticity diagram essentially describes the quality of colour. It uses three colour-matching functions to calculate the chromaticity coordinates x and y, which span the chromaticity diagram. The colour-matching functions correspond to the response of the three cone cells in the human eye, which are sensitive in the red, green and blue spectral range. Additionally, the response of the human eye is taken into account by defining the green colour-matching function to be identical to the *eye sensitivity function* $V(\lambda)$ (CIE 1978), which has its maximum at 555 nm [67]. The red and blue colour-matching functions are mathematically transformed into a new set with the green colour-matching function fixed. Any spectrum can be described by the colour-matching functions, with three *tristimulus values* X, Y, Z specifying the contribution of each colour-matching function. The chromaticity coordinates x, y, z are calculated by normalising the tristimulus

values according to

$$x = \frac{X}{X+Y+Z} \tag{2.12}$$

$$y = \frac{Y}{X+Y+Z} \tag{2.13}$$

$$z = \frac{Z}{X+Y+Z} = 1-x-y. \tag{2.14}$$

The z chromaticity coordinate is redundant, because it can be calculated from the x and y chromaticity coordinates and does not provide any additional information.

It was shown that the CIE 1931 chromaticity diagram (x, y) possesses small areas of colour, which appear identical to the human eye [68]. These areas are elliptical in shape. Taking these geometrical features into account, the modified CIE 1976 (u', v') uniform chromaticity diagram was introduced, which is shown in Fig. 2.11 [69]. Monochromatic light can be found on the perimeter, whereas white light is located in a region closer to the centre of the diagram. Every colour can be described by chromaticity coordinates, i.e. its location in the chromaticity diagram. Although the light from LEDs is almost monochromatic, is has a spectral linewidth. The coordinates of LEDs, therefore, can be found in close proximity to the perimeter of the chromaticity diagram. If the linewidth becomes broader the location moves towards the centre of the diagram, such as for white light, which covers most of the visible spectrum.

White light can be generated from a combination of numerous potential spectra. For its characterisation standards are used. One unique standard is the *Planckian black body radiator*, because it can be described with only one parameter, namely the colour temperature. The black body spectrum is described by [70, 71]

$$I(\lambda) = \frac{2hc^2}{\lambda^5\left(e^{\frac{hc}{\lambda k_B T}}-1\right)}. \tag{2.15}$$

Fig. 2.12 shows Planckian black body spectra for various temperatures. The maximum of the peak can be described by *Wien's displacement law* [72]

$$\lambda_{\max} = \frac{2889\ \mu\text{m K}}{T}. \tag{2.16}$$

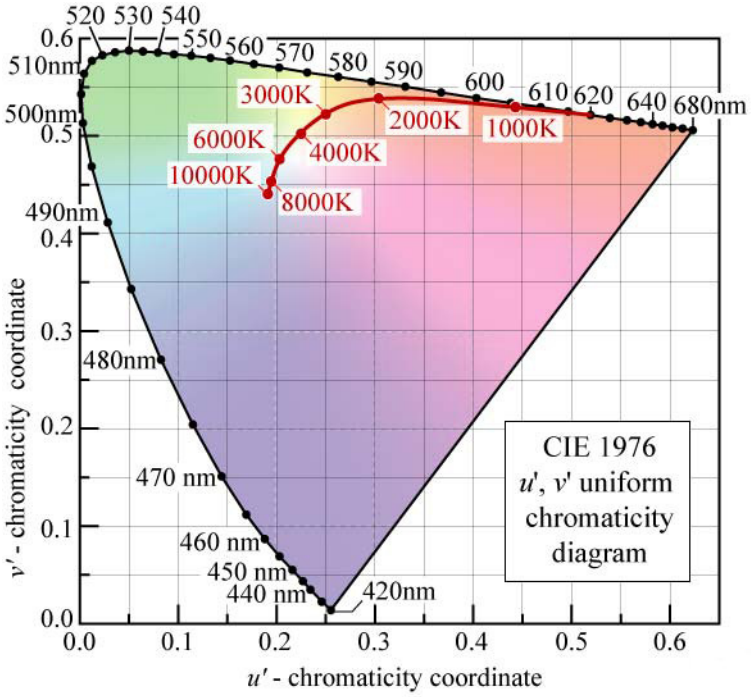

Figure 2.11: *CIE 1976 (u', v') uniform chromaticity diagram calculated using the CIE 1931 2° standard observer. Monochromatic colour is located on the perimeter, whereas white light is close to the centre of the diagram. The Planckian locus for colour temperatures between 1000 K and 10000 K is also shown. Taken from Ref. [20].*

With increasing temperature the maximum of the peak shifts towards shorter wavelengths. The temperature, also referred to as *colour temperature* can be used to describe the emission spectra of a Planckian black body radiator.

Each Planckian black body spectrum for different colour temperatures can be described with chromaticity coordinates, spanning a curve in the chromaticity diagram. This curve is known as the *Planckian locus*, displayed in Fig. 2.11. The spectrum of a black body with very low colour temperatures contains more infrared light and its location in the chromaticity diagram can be found near the perimeter of red light. With increasing colour temperature, the spectrum shifts into the range of the visible light and the position in the chromaticity diagram moves to the region where white light is located.

The term colour temperature stems from the fact that with increasing temper-

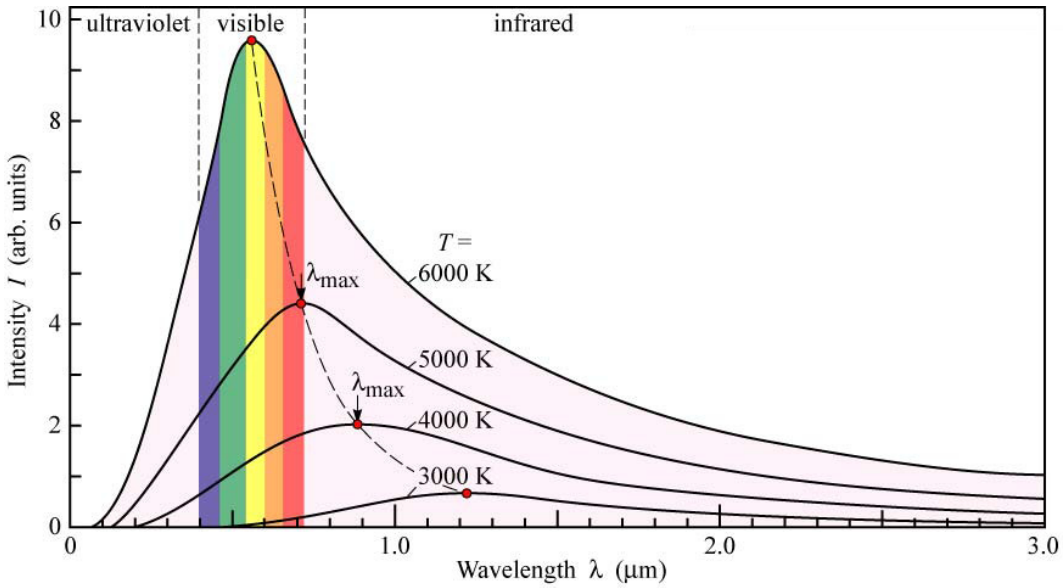

Figure 2.12: *Intensity distribution of a Planckian black body radiator as a function of wavelength for different temperatures. The position of the maximum is described by Wien's law. Taken from Ref. [20].*

ature a black body glows red, orange, yellow, white, and then blueish. Therefore, the *colour temperature* (unit: K) of a white light source corresponds to the temperature of a Planckian black body radiator of the same chromaticity coordinates. Not all white light sources, however, can be described with a Planckian black body radiator, i.e. they are not located on the Planckian locus. Hence, the *correlated colour temperature* (CCT, unit: K) of a white light source is the temperature of a black body radiator whose colour has the best resemblance to the white light source [73]. The choice of white light with a certain CCT depends strongly on the individual preference. In Japan white light with higher CCTs (around 5000 K) describing cold white light is preferred, whereas warm white light (CCTs below 3000 K) is generally desired in the UK and US [74].

A true white light source needs to have the ability to reproduce the real colour of the illuminated object accurately. The *colour rendering index* (CRI) is a measure of the ability of a light source to render or reproduce the colour of an object faithfully in comparison with the light of an ideal or natural source [75, 69]. The CRI is dimensionless and its maximum value is 100, representing an ideal colour rendering source. The CRI is an important parameter to describe the

quality of a light source. Light sources in homes or offices should have high colour rendering capabilities (high CRI), whereas colour rendering is less crucial (lower CRI) for street lights or lights for general illumination. The CRI of a Planckian black body radiator is defined to have the highest colour rendering capabilities (CRI of 100), because it most closely resembles natural daylight. The closest light source to a black body radiator is the incandescent light bulb, which (as a black body emitter) has the highest possible CRI of 100, as a consequence all other light sources have a lower CRI.

Photometry describes the science of the measurement of light, which takes the human eye response into account. For the characterisation of white light generation the *luminous efficacy* is an important parameter, which describes the efficiency of the energy conversion. The luminous efficacy is the ratio of the luminous flux and power. The unit of luminous efficacy is lumen per watt (lm/W). For optical radiation the power is equivalent to the total power of the electromagnetic radiation. For electrically driven devices, such as LEDs, it is the total consumed electrical power of the light source.

2.6 Light-emitting diodes

The basic building block of an LED is a p-n junction consisting of a p- and n-type doped semiconductor.

In an unbiased p-n junction in thermal equilibrium electrons originating from donors on the n-side diffuse towards the p-side where they recombine with holes. The same process happens with holes diffusing to the n-side. This creates a depletion region in the vicinity of the junction free from free carriers. Ionised donors and acceptors (the dopants), however, stay behind forming a space charge region, which creates an electric field across the junction. This electric field counteracts the diffusion current and leads to a drift current of electrons (holes) from the p-side (n-side) to the n-side (p-side). In thermal equilibrium both currents cancel each other, meaning there is no total current flowing across the junction. Fig. 2.13(a) shows the band bending caused by the internal electric field, which represents a barrier for free carriers. In the case of a positively biased p-n junction (forward bias) the externally applied electric field opposes the internal field and lowers the barrier created by it. Injected free carriers diffuse across the junction

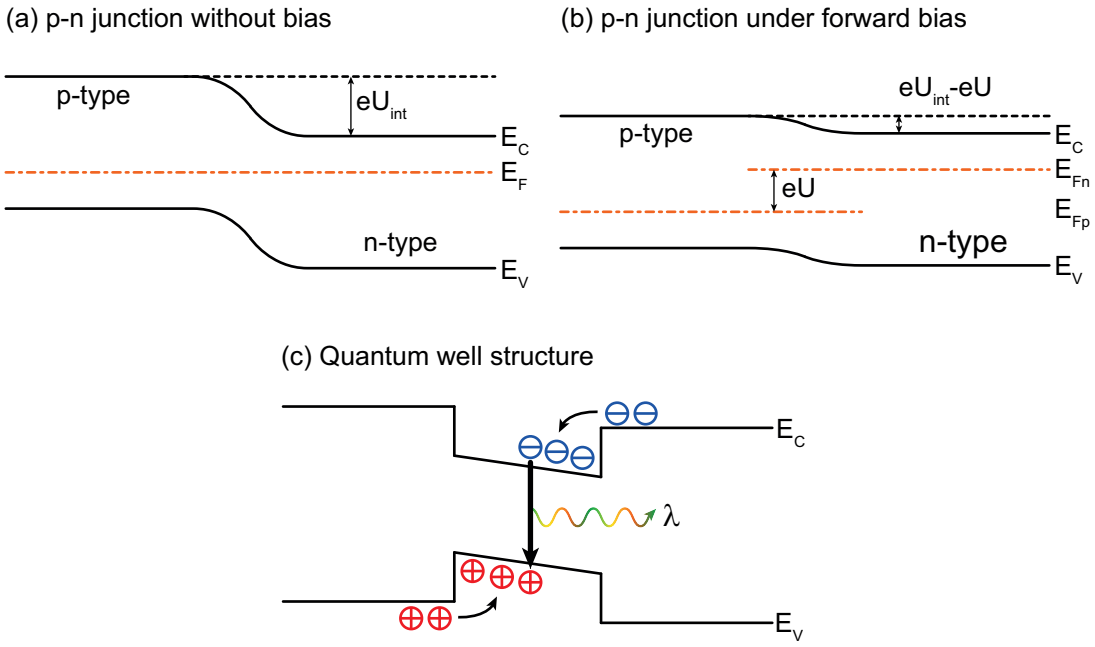

Figure 2.13: *(a) p-n junction without bias with U_{int} caused by the internal electric field, (b) p-n junction under forward bias U and (c) quantum well structure.*

into the region of opposite conductivity and recombine there by emitting light as shown in Fig. 2.13(b). In the case of a negatively biased p-n junction the potential barrier is increased and no current flows across the junction.

In a p-n junction the area where recombination occurs is defined by the diffusion length, which is the mean distance a carrier diffuses until recombination. This reduces the electron (n) and hole densities (p) and hence radiative recombination rate. To make the recombination process more efficient most modern LEDs possess a QW structure, which is a semiconductor with lower band gap, positioned between the p- and n-type semiconductor of larger band gaps as displayed in Fig. 2.13(c). Here injected carriers are trapped or confined in the well region, because of the lower potential. The QW width is in general of a few nanometers and therefore much smaller than the diffusion length, which is 50–60 nm in GaN and could be of a few tens of μm in the case of GaAs [76, 77, 78, 79]. The result is a higher carrier density, which is proportional to the radiative recombination rate $R \propto np$ in comparison with a p-n junction where the area is defined by the diffusion length. LEDs commonly consist of multiple wells to further increase

confinement, which is referred to as a MQW structure .

The light emitted by LEDs is defined by the band gap of the semiconductor. Commonly, there are two approaches to achieve white light. Either a combination of LEDs emitting at different wavelengths is used or a single blue or UV LED is covered by a down-converting material. White light can be generated by different combinations of emission spectra as described below.

The trivial approach is using two or more LEDs on separate chips, each emitting nearly monochromatic light, which combined emit white light. When using two LEDs (*dichromatic*) their wavelengths have to be complementary and at a certain power ratio in order to be perceived as white. Dichromatic light sources in general have high luminous efficacy (ratio of luminous flux to power in units of lumen per watt), but a low colour rendering index. The CRI can be improved by adding more LEDs of a different emission wavelength; however this comes with a trade-off in luminous efficacy [1, 20]. Examples would be a blue and yellow LED or a combination of three LEDs emitting in the red, green and blue (RGB) spectral region.

In a more complicated approach the active regions emitting at different wavelengths of the same material system are integrated into one structure, which is described as *monolithic*. A structure using this principle can consists of two or more active regions, i.e. MQW stacks, which are designed to emit at different wavelengths [80, 81, 82]. In the case of an InGaN-based LED this can be achieved by varying the width or InN content of the QWs. Increasing the InN content, however, leads to a decline of crystal quality and an increase in piezoelectric fields, which in turn have a detrimental influence on the emission properties. It is possible to grow catalyst-free GaN nanorods without dislocations and reduced strain along the axis of the nanorod [83, 84]. These rods can provide a template for the growth of InGaN nanodisks emitting from the UV to the red [35]. White light can then be produced by a combination of stacks of InGaN MQW disks emitting at different wavelengths [84]. Another method for white light generation is based on varying the nanorod diameter, which has an influence on the InN incorporation into the InGaN/GaN MQWs through a shadowing effect [34].

The currently leading approach for white LEDs, however, consists of a single LED, emitting in the UV or the visible spectrum, coated with one or more energy down-converting phosphors. The most commonly used combination is a blue

LED, using InGaN/GaN MQWs as the active region, pumping a yellow emitting phosphor.

The conversion efficiency using a converter is limited by two factors. The external quantum efficiency (EQE), η_{EQE}, of the phosphor describing the ratio of numbers of photons emitted and absorbed by the converter. The EQE is also the product of internal quantum efficiency (IQE), η_{IQE}, and extraction efficiency $\eta_{\mathrm{extraction}}$

$$\eta_{\mathrm{EQE}} = \eta_{\mathrm{IQE}} \cdot \eta_{\mathrm{extraction}}. \tag{2.17}$$

The second limitation is the Stokes shift, which is an inherent energy loss due to the conversion of the absorbed photon with wavelength λ_1 to the emitted photon with wavelength λ_2 ($\lambda_1 < \lambda_2$). This energy loss is fundamental and cannot be overcome and is given by

$$\Delta E = E_1 - E_2 = hc\left(\frac{1}{\lambda_1} - \frac{1}{\lambda_2}\right). \tag{2.18}$$

The efficiency of the wavelength conversion can be expressed as

$$\eta_{\mathrm{Stokes}} = \frac{E_2}{E_1} = \frac{\lambda_1}{\lambda_2}. \tag{2.19}$$

The total efficiency of the conversion process of the wavelength converter is the product of Eqs. (2.17) and (2.19)

$$\eta_{\mathrm{converter}} = \eta_{\mathrm{EQE}} \cdot \eta_{\mathrm{Stokes}} = \eta_{\mathrm{EQE}} \cdot \frac{\lambda_1}{\lambda_2}. \tag{2.20}$$

Due to the additional energy loss from the Stokes shift, white LEDs employing a phosphor for the conversion process show lower efficiencies than white LEDs using multiple single LEDs of different colours. The highest energy losses occur when UV light is converted into red light.

Materials suited as wavelength converters include phosphors, organic dyes and semiconductors. The EQE for all three converters can be close to 100%.

Phosphors possess a broad emission band making them very suitable for white light generation and are very stable. They are made of an inorganic host doped

with an optically active element. Common hosts are garnets, such as yttrium aluminium garnet (YAG), $Y_3Al_5O_{12}$ [85, 86]. The optically active element can also be a rare earth element, rare earth oxide or other rare earth compound. For white light generation cerium (Ce) is used, whereas neodymium (Ny) is utilised for lasers. By adding gadolinium (Gd) and/or gallium (Ga) to fabricate Ce-doped $(Y_{1-x}Gd_x)_3(Al_{1-y}Ga_y)_5O_{15}$ the emission of the phosphor can be shifted [87]. This makes it possible to change and adapt the chromaticity of the white light when used together with a blue LED. For the fabrication of white LEDs, the YAG phosphor is incorporated in epoxy resin. The epoxy is then deposited on the blue LED die. The fraction of the absorbed blue light by the phosphor depends on the thickness of the epoxy–phosphor layer and its concentration, which also defines the yellow emission intensity of the phosphor.

Another possibility is to replace the phosphor with a wavelength converter based on another semiconductor heterostructure. In this case the light from the blue LED will be absorbed by a second active region, such as an AlGaInP/GaAs double heterostructure, which will emit light in the amber spectral range [88, 89]. The AlGaInP/GaAs structure cannot be directly grown on top of the blue LED, because of the different lattice constants. Before bonding these two materials together, the GaAs substrate needs to be removed due to unwanted absorption of the blue light. Either the blue LED is electrically contacted and optically pumps the the AlGaInP/GasAs structure or the contacts are placed on the top and the bottom of the structure for carrier injection into the entire structure. To obtain white light the intensities of the two light sources need to be carefully balanced.

The third type of converter is made of organic dye molecules, which are commercially available and possess good absorption and emission characteristics. In contrast to their inorganic counterparts, however, their organic nature can limit their lifetime and stability [90, 86].

Dichromatic white LEDs have the highest luminous efficiency, but low CRI. By using trichromatic sources the CRI can be improved, however its luminous efficiency will decrease. This is a fundamental trade-off between the colour rendering capabilities and the luminous efficiency of an LED, which cannot be eliminated [1].

An extensive introduction on the principle of LEDs, operation, design, packaging and applications can be found in Refs. [1, 20].

Chapter 3

Experimental methods

This chapter introduces the growth methods and experimental techniques used in this study of III-nitride semiconductor samples. The different spectroscopy and microscopy techniques will be illustrated and the principles of photoluminescence (PL), scanning electron microscopy (SEM), cathodoluminescence (CL) and electron channelling contrast imaging (ECCI) will be described.

3.1 Sample fabrication

The epitaxial semiconductor samples in this study are fabricated by the group of Prof. T. Wang at the University of Sheffield and the group of Prof. C. Humphreys at the University of Cambridge. Planar InGaN/GaN MQW structures are grown by metal-organic chemical vapour deposition (MOCVD).

This is the most commonly used growth method for III-nitrides and is also known as metal-organic vapour phase epitaxy (MOVPE) [91, 50, 92]. In contrast to molecular beam epitaxy (MBE) the growth of epilayers takes place as a chemical reaction from the gas phase. The solid and liquid precursors are stored in bubblers. A suitable carrier gas, typically hydrogen or nitrogen, is passed through the bubblers to transport the reagents into the growth chamber. Precursors which are already gaseous are directly introduced into the chamber. Source materials for the growth of GaN and InGaN-based structures are trimethylgallium (TMGa) for gallium, trimethylindium (TMIn) for indium and ammonia (NH_3) for nitrogen. The source material is dissociated in the growth chamber and deposited on

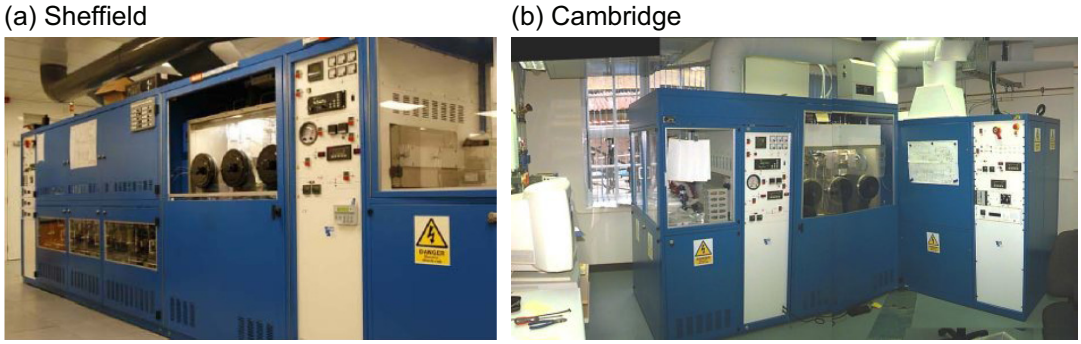

Figure 3.1: *Photographs of the MOCVD growth reactors at the (a) University of Sheffield and (b) University of Cambridge. The MOCVD systems at both universities are Thomas Swan showerhead reactors. Both growth facilities are part of the EPSRC National Centre for III-V Technologies. Images from www.epsrciii-vcentre.com.*

a heated substrate.

The key components of the planar MQW samples are as follows. For the growth of all the samples (0001) sapphire was used as the substrate. To overcome the large lattice mismatch between the sapphire and GaN (14% for (0001) orientation) a buffer (or nucleation) layer was grown followed by a thick GaN layer (a few μm). The group at the University of Sheffield, for example, uses a high-temperature atomically flat AlN layer as a buffer [93]. Alternating thin layers of InGaN, forming the QW, and GaN, forming the barriers, are the key components of the active region. The capping layer consists of GaN. Typical well and barrier widths are 2–3 nm and 8–11 nm, respectively, with five to ten periods and the InN content ranges between 10% and 25%. For the growth of the MQW structure a quasi two-temperature step was used by the group at the University of Cambridge. After each InGaN well layer a 1 nm protective GaN layer was grown at the same temperature. The growth was then continued while the temperature was ramped to a higher temperature for the GaN barrier growth.

The MOCVD growth reactors at the Universities of Sheffield and Cambridge are shown in Fig. 3.1. The specific sample structures will be introduced in the respective chapters.

Nanorods are fabricated in a top-down approach at the University of Sheffield (group of Prof. Tao Wang) from planar MQWs using a self-assembled metal

nanomask. A more detailed description of the fabrication process can be found in Section 6.2.

The organic materials for the colour conversion process for the generation of white light are synthesised in the group of Prof. Peter Skabara at the Department of Pure & Applied Chemistry at the University of Strathclyde. The organic compounds are described in Section 7.3.1 and 7.4.1.

3.2 Photoluminescence

Photoluminescence (PL) is the emitted light from a material excited by photons. In the case of a semiconductor an electron–hole pair is formed when an electron is excited across the band gap of the material from the valence band into the conduction band leaving behind a hole. These electrons and holes thermally relax to the bottom of the conduction band and top of the valence band, respectively, before recombining. This recombination might happen radiatively via the emission of photons or non-radiatively via the emission of phonons or electrons. Radiative recombination in a semiconductor can involve impurity related transitions. One of the charge carriers can be bound to an impurity with an energy level just below the conduction band or above the valence band. Examples are excitons bound to a neutral (D^0X) or ionised donor (D^+X); the same applies to acceptors. Recombination can also occur when both carriers are bound to impurities, such as a donor-acceptor pair (DAP) transition. Non-radiative recombination processes can involve: the emission of multiple phonons; the Auger effect, where the energy is transferred to another electron that is raised to a higher energy level with subsequent ejection of the electron or thermalisation of its energy via phonon emission; or recombination at surface states and defects. The energy of the PL excitation source, usually a laser, has to be higher than the band gap of the investigated material in order for excitation to take place.

A schematic diagram of the used PL setup is shown in Fig. 3.2. The 325 nm line of a helium-cadmium laser (*JSC Plasma HCL-10U*) or a 405 nm laser diode (*CrystaLaser*) was used as an excitation source. The maximum output power at the sample position is 0.8 mW for the He-Cd laser and 44 mW for the laser diode. A Pellin Broca prism was used to remove the unwanted plasma lines from the He-Cd laser. The laser diode is positioned after the prism on a magnetic

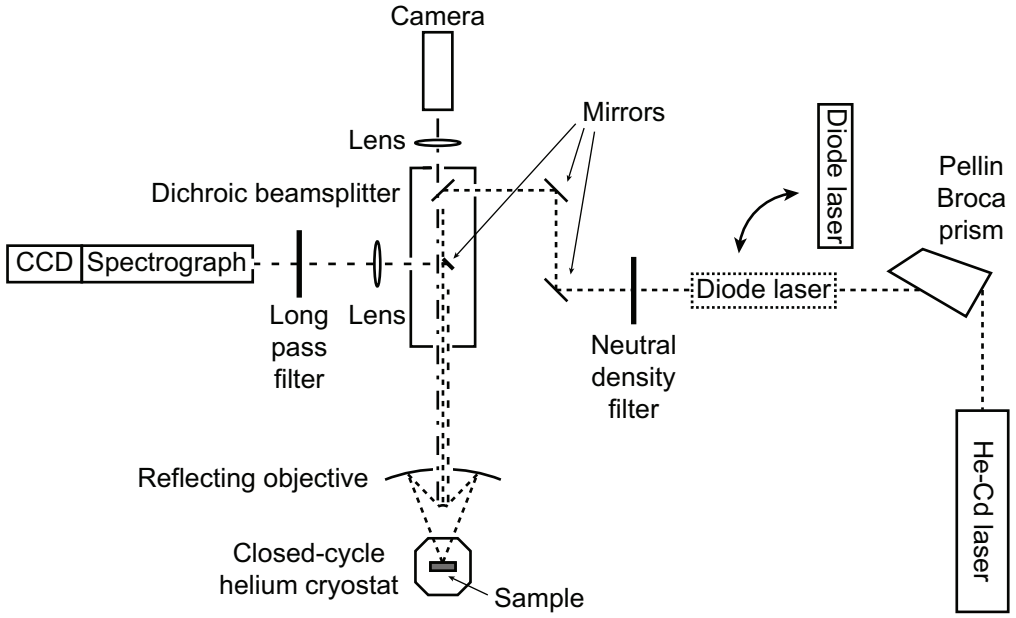

Figure 3.2: *Schematic diagram of the PL setup. The 405 nm laser diode is fixed on a magnetic mount for easy removal when the He-Cd laser is used.*

mount for easy removal when the Hd-Cd laser is used. Furthermore, the dichroic beamsplitter can be changed to be suitable for both lasers. For power-dependent PL measurements neutral density (ND) filters were inserted into the beam path. The sample was placed in an evacuated closed-cycle helium cryostat with a cold head, which could be cooled down to approximately 16 K. For temperature-dependent measurements a heater was attached to the cold head and operated via a temperature controller (*Oxford Instruments ITC4*). The light emitted from the sample was dispersed in a 1/8 m spectrograph (*Oriel MS125*) with a 25 μm slit and interchangeable gratings, 400 lines/mm (spectral resolution: 0.65 nm), 1200 lines/mm (resolution: 0.22 nm) or 2400 line/mm (resolution: 0.11 nm), and then collected by a 1024-channel charge-coupled device (CCD, *Andor Technology DV420-OE*). A suitable long pass filter was placed in front of the spectrometer to remove the unwanted laser line from the detected spectra.

For electroluminescence (EL) measurements the same setup was used and slightly modified. Electrical leads were fitted to the cryostat and connected to a source measure unit (*Keithley Instruments 236*). The light collection system remained the same.

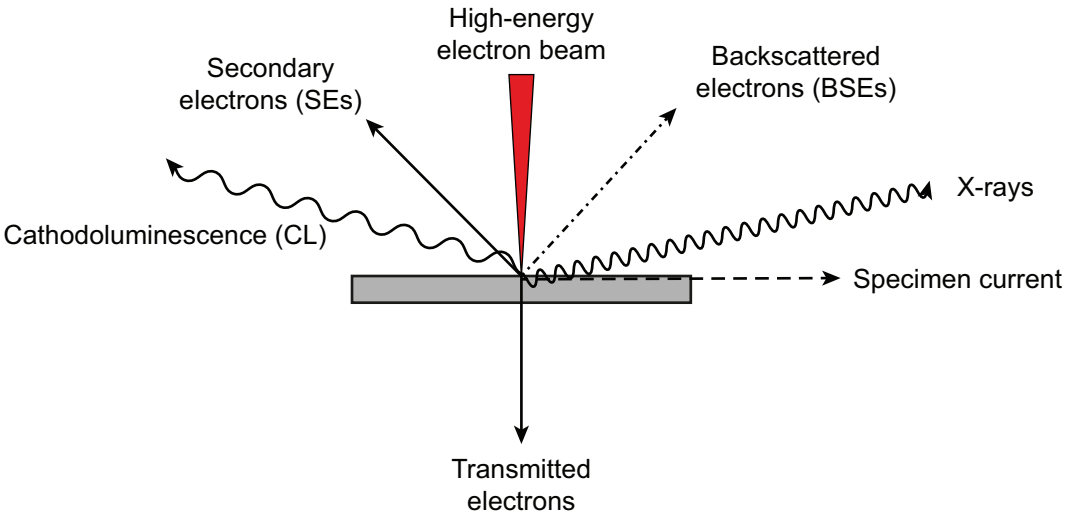

Figure 3.3: *Signals generated by the interaction of an energetic electron beam with the surface of a solid material.*

3.3 Interaction of electrons with solids

When a high-energy electron beam hits a solid various signals are produced as shown in Fig. 3.3, including: secondary electrons (SEs), backscattered electrons (BSEs), transmitted electrons, characteristic X-rays, specimen current and cathodoluminescence (CL). Electrons leaving the surface with energies less than ≈50 eV are referred to as SEs (by comparison with the electrons from the beam, which are referred to as primary electrons) [94]. SEs are outer shell electrons emitted from atoms that have been ionised. The low energy (and therefore high surface sensitivity) makes them most suitable for creating a topographical image of the sample. BSEs are inelastically or elastically scattered primary electrons. Their energy ranges between 50 eV and the energy of the incident beam electrons. Because their scatter cross-section is proportional to Z^2 (Z: atomic number), atoms with increasing atomic number scatter a higher fraction of electrons and this can be used for differentiation between elements of significantly different atomic number. Characteristic X-rays are generated after a core shell electron is ejected and an electron from a higher energy level fills its place. The energy lost by the electron, defined by the difference in the energy levels involved, can be released by the emission of an X-ray. The resulting X-ray spectrum is char-

acteristic of each element, because the energy of the emitted X-ray depends on the electron energy levels. Measurements of the X-ray spectrum can be used for compositional analysis.

3.3.1 Scanning electron microscopy

The discussion below is a short summary of electron detection and image formation using an SEM following Refs. [95, 96].

SEs are commonly detected using an Everhart–Thornley detector (E–T), placed above and to one side of the sample, or a "through-the-lens" (TTL) detector, built into the pole piece. The E–T detector consists of a Faraday cage biased at a positive potential (up to 250 V) to collect the SEs over a large solid angle. A second, isolated and larger positive potential accelerates them to a high enough energy to generate photons when they hit a scintillator. A photomultiplier tube is then used for amplification and detection of the light emitted from the scintillator. The TTL detector uses the magnetic field from the last lens inside the pole piece extending to the sample at small working distances. SEs spiral upwards through the pole piece in this field and a strong positive bias accelerates them towards a scintillator. BSEs can be detected using a negatively biased E–T detector. The negative bias causes the low-energy SEs to be rejected and only high-energy BSEs in direct line-of-sight are collected. Dedicated BSE detectors can be simple diodes, which can collect BSEs over a larger angle, such as the one used for ECCI as discussed in Section 3.5.

The electron beam scans across the sample surface and a topographical image is created from the SE and/or BSE signals. The number and trajectories of SEs and BSEs depend strongly on the angle between the sample and the incident electron beam and the orientation of the detector. Both the SE coefficient and the backscatter coefficient increase with sample tilt, which leads to an increased yield of SEs and BSEs from tilted surfaces. Furthermore, surfaces tilted away from the detector will appear darker, since electrons ejected from them are not in direct line-of-sight of the detector as discussed below.

SE images are easily interpreted, even by a viewer without any knowledge of electron microscopy. The reason for this is that the image formation process using a positively biased E–T detector has a correspondence to the image formation

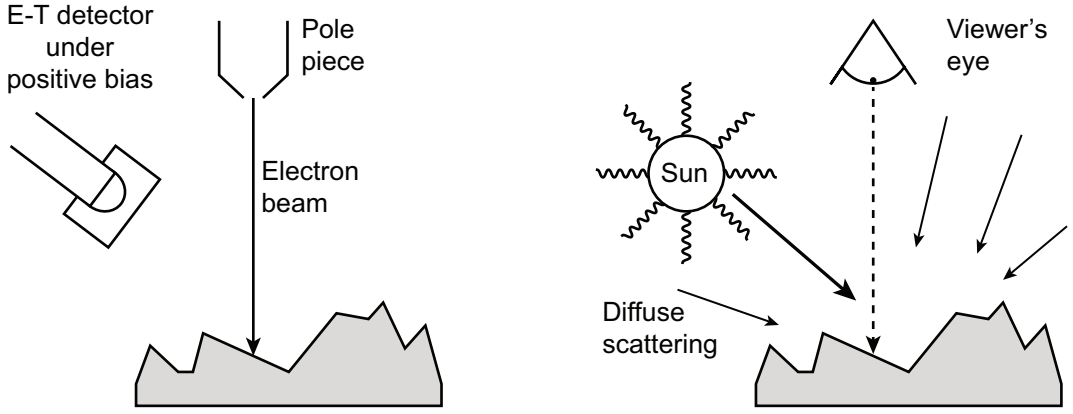

Figure 3.4: *Comparison of the image formation process using a positively bias E–T detector and the electron beam with the human eye and a light source.*

involving a human eye and an illuminated object from above. This is illustrated in Fig. 3.4. To understand this analogy the viewer is placed at the end of the electron column and the detector is substituted by the light source, such as the sun. Surfaces tilted away from the detector show contrast, because the SEs emitted from them are detected due to the positive bias. These surfaces, though, appear darker than the surfaces directly in line-of-sight of the detector. This is similar to surfaces, which are not directly illuminated by a light source, but still are seen by the human eye.

For high resolution or high magnification imaging, it is essential to have a small beam diameter. Without losing beam current this is only possible to achieve by increasing the brightness β of the gun. The brightness is defined as beam current per unit area per solid angle and is constant anywhere in the electron column. The brightness is defined by the following equation

$$\beta = \frac{\text{current}}{\text{area} \cdot \text{solid angle}} = \frac{4I_p}{\pi^2 d_p^2 \alpha_p^2} \tag{3.1}$$

with the beam current I_p, the cross-sectional area of the beam d_p and the angular beam spread α_p measured at the specimen. These requirements are fulfilled by a field emission gun, which will be described below.

Several types of electron guns exist in commercial SEMs. They are classified into two types; thermionic emitters or field emission guns. Thermionic emitters

consist of a tungsten or LaB_6 source. Thermionic emission is achieved when electrons can overcome the work function of a material when it is heated. Thermionic sources are inexpensive, but have low brightness and a limited lifetime. Newer high resolution SEMs use field emission guns, which are of cold, thermal or Schottky type. In a field emission gun a very fine tip is mounted on a tungsten wire operated under a negative bias generating an electric field at the tip. This bias lowers the potential barrier (or work function) and also makes it narrower, allowing electrons to tunnel through to escape from the tip. In a cold field emitter the gun is required to be at a very high vacuum to reduce deposition of gas molecules on the surface of the tip. Gas molecules on the surface lower the emission current, which requires the tip to be cleaned at elevated temperatures. A thermal field emitter is identical to a cold emitter except that it is operated at elevated temperatures to further limit the deposition of gas molecules on the tip. In a Schottky type field emitter thermionic emission is enhanced using the electric field to lower the work function barrier. The barrier is further decreased by depositing ZrO_2 on the tip. The high beam brightness, stability of the source, small beam size and simple operation makes it commonly used in SEMs.

An extensive review of scanning electron imaging, electron optics and detection analysis techniques can be found in Refs. [95, 97, 98, 96].

SE imaging, CL hyperspectral imaging and ECCI in this work are performed using a commercial field emission gun scanning electron microscope (FEGSEM, *FEI Sirion 200*). The SEM employs a Schottky type electron source and is fitted with custom-built components for CL and ECCI.

3.3.2 Cathodoluminescence

CL is the process of light generation by an impinging beam of electrons on a material. The primary electrons lose energy through impact ionisation, which is an inelastic process, generating electron–hole pairs. These pairs can then recombine radiatively generating light emission, as in PL. It is important to note that the electron energy is a few orders of magnitude larger than the band gap of the semiconductor, which makes it possible to even look at wide band gap materials, such as diamond, AlN or boron nitride (BN). There are, however, short wavelength

limits imposed on the wavelength detection, such as absorption by water vapour below 200 nm (spectrometer and detector are not inside the vacuum system) [99], the material and quantum efficiency of the detector and other optical elements (absorption of UV light by glass windows or lenses).

The interaction between the electron beam and the solid is very important for CL imaging. Electrons impinging on a solid undergo either elastic or inelastic scattering events, as discussed previously.

The elastic scatter process can be described by the Rutherford scattering cross-section for scattering angles between 0° and 180° [95], which has the form

$$Q = \frac{e^4}{4}\,\frac{Z^2}{E_i^2}\,\frac{\pi}{\delta(\delta+1)} \tag{3.2}$$

where e is the electron charge, Z the atomic number of the material, E_i the instantaneous electron energy at any point in the specimen and δ a screening parameter. For electron beam energies above about 50 keV Eq. (3.2) has to be modified to take relativistic effects into account.

The inelastic process, where primary electrons lose their energy through scatter events, is described by the Bethe expression [100]

$$\frac{dE}{ds}\left(\frac{\text{keV}}{\text{cm}}\right) = -2\pi e^4 N_A \frac{Z\rho}{AE_i}\ln\left(\frac{1.166E_i}{J}\right) \tag{3.3}$$

$$J\,(\text{keV}) = \left(9.76Z + 58.5Z^{-0.19}\right)\cdot 10^{-3} \tag{3.4}$$

where N_A stands for Avogadro's number, ρ for the density, A for the atomic weight, J for the average loss in energy per event or mean ionisation potential and E_i the instantaneous electron energy. dE/ds describes the rate of energy loss dE along the travelled distance ds.

Primary electrons impinging on the material go through multiple elastic and inelastic scattering events, which randomise their trajectories. This is a gradual process taking place in a certain three-dimensional (3D) volume, the so-called interaction volume (also referred to as excitation or generation volume). The Grün or electron beam range R_e, which is dependent on the electron beam energy E_b, gives an estimate of the depth of the extension of energy dissipation. This

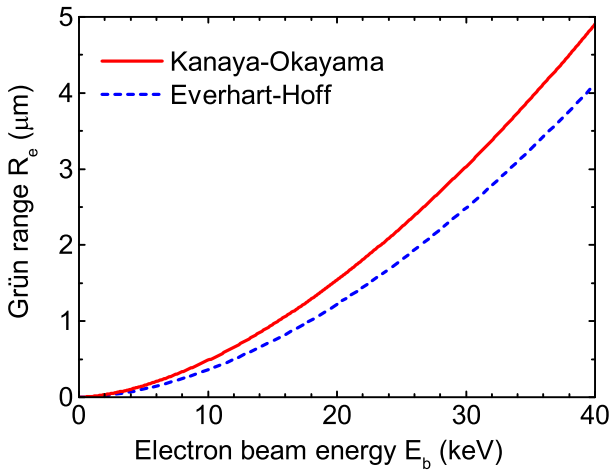

Figure 3.5: *Grün range R_e for GaN as a function of electron beam energy E_b calculated using Eqs. (3.6) and (3.7) derived from the Everhart–Hoff and Kanaya–Okayama models, respectively.*

range is empirically derived and can be expressed as [101]

$$R_e = \frac{k}{\rho} E_b^{\alpha} \tag{3.5}$$

with the parameters k and α both dependent on energy and atomic number and ρ being the density of the material. Everhart and Hoff derived the following equation for the electron beam range for electron energies between 5–25 keV and atomic numbers $10 < Z < 15$ [102]

$$R_e = \frac{0.0398}{\rho} E_b^{1.75} \, (\mu m) \tag{3.6}$$

with ρ in g/cm^3 and E_b in keV. Further modification by Kanaya and Okayama lead to a more generalised Grün range for a wider range of Z [103]

$$R_e = \frac{0.0276 \; A}{\rho Z^{0.889}} E_b^{1.67} \, (\mu m) \tag{3.7}$$

with E_b in keV and the atomic weight A in g/mol. A comparison between the

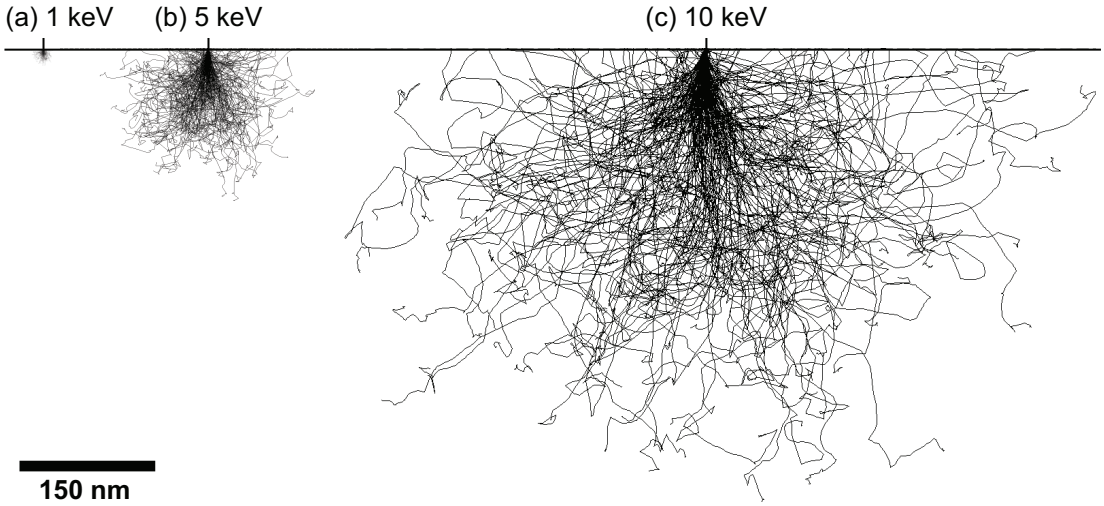

Figure 3.6: *Monte Carlo simulations of the electrons trajectories at (a) 1 keV, (b) 5 keV and (c) 10 keV beam energies impinging on a GaN layer. For clarity only 200 of the simulated electron trajectories are shown.*

range R_e calculated using Eq. (3.6) (Everhart–Hoff) and Eq. (3.7) (Kanaya–Okayama) for GaN is shown in Fig. 3.5.

Electron interactions and their trajectories in a solid can be simulated using a Monte Carlo method. The electron trajectories are simulated using random numbers for possible paths and durations until an elastic or inelastic scattering event using Eqs. (3.2) and (3.3). After this event the process starts again until the electron is absorbed, has left the specimen or its energy is no longer sufficient to ionise the material.

Monte Carlo simulations have been performed using the software package CASINO [104]. For these simulations the electron beam power was kept constant by adjusting the number of simulated electrons for each beam energy (1 keV: 2×10^6 electrons; 5 keV: 4×10^5 electrons; 10 keV: 2×10^5 electrons). Fig. 3.6 displays the results of the simulated electron trajectories, with only 200 shown for clarity, generated by an electron beam of 2 nm radius and energies of 1, 5 and 10 keV impinging on a GaN layer. From the simulations it is obvious that with increasing acceleration voltage, i.e. beam energy, the volume occupied by the interacting electrons becomes larger, up to a few 100 nm in GaN at 10 keV.

The electron trajectories are not a particularly good way to represent the in-

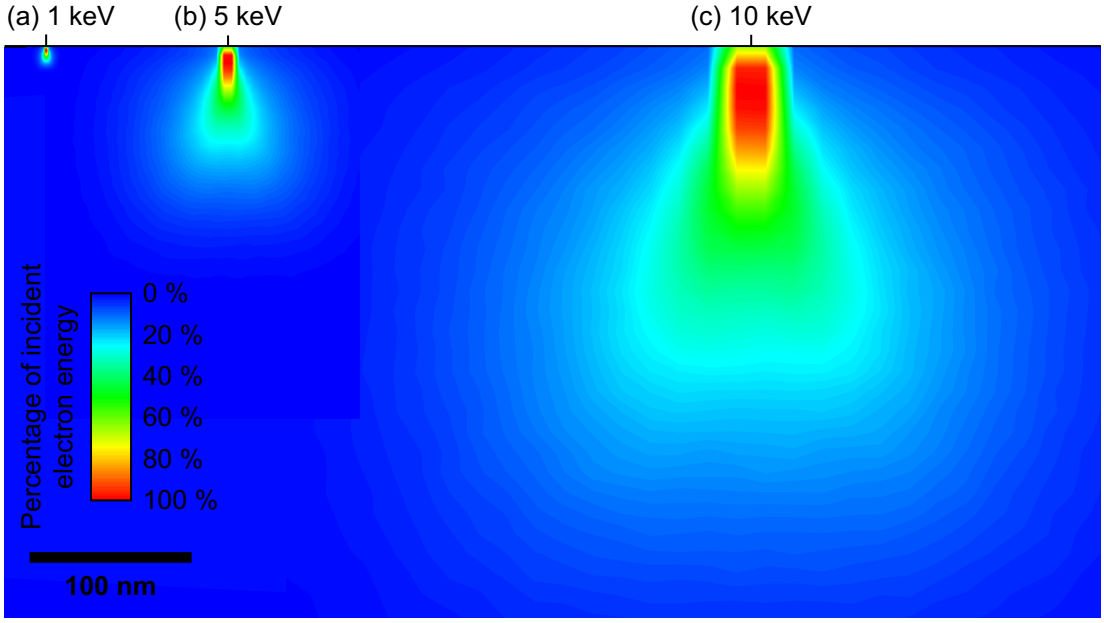

Figure 3.7: *Monte Carlo simulations of the electron energy deposition profile at (a) 1 keV, (b) 5 keV and (c) 10 keV beam energies impinging on a GaN layer.*

teraction volume, because the further away the electrons migrate from the entry point into the material the more energy they have lost through inelastic scattering. Fig. 3.7 displays the electron energy deposition profile of the electron beam obtained from the same Monte Carlo simulations as in Fig. 3.6. Similar to the trajectories the deposition profiles become larger with increasing beam energy. The contours represent the percentage of the total energy deposited within that region. Although the dimension of the energy deposition volume appears to be of a few 100 nm at 10 keV, most of the energy is deposited in a much smaller area. The electrons have already lost 90% of their energy over a few tens of nanometers. The electron beam radius used for these simulations is 2 nm, almost two orders of magnitude smaller than dimension of the energy deposition volume.

The shape of the interaction volume is dependent on the atomic number Z and beam energy E_b. For low atomic numbers it is pear shaped, for medium atomic numbers it is spherical and it is hemispherical for larger atomic numbers [96]. This can be explained by the dependence of elastic scattering on the atomic number and beam energy. For example, at low atomic numbers the beam penetrates deeper into the material forming a narrow neck at the top of the pear shape.

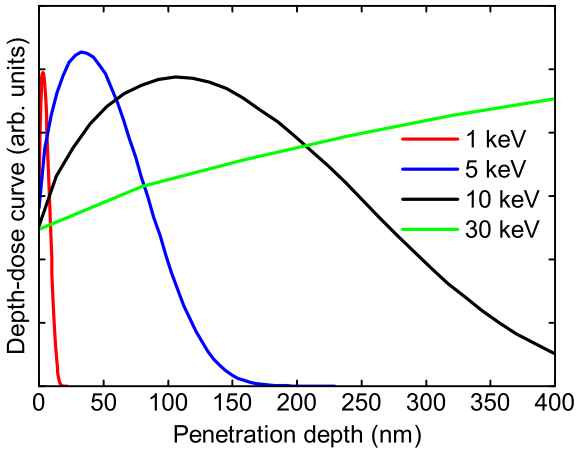

Figure 3.8: *Depth-dose function of GaN at various electron beam energies obtained by Monte Carlo simulations. The depth-dose curve is proportional to the number of electron–hole pairs generated per incident electron of energy E_b per unit time and per unit depth.*

This excitation volume defines the lateral dimension and the depth at which the electron beam generates electron–hole pairs. The generation rate of electron–hole pairs is expressed by the depth-dose function, which defines the number of electron–hole pairs generated per incident electron of energy E_b per unit time and per unit depth. Fig. 3.8 shows the depth-dose curves for GaN at various electron energies obtained by the above mentioned Monte Carlo simulations.

The volume where the CL signal is generated is related to the excitation volume. After the generation of electron–hole pairs, these pairs can diffuse before recombination. Their diffusion length increases the volume where the CL signal is generated compared with the volume the electron–hole pairs are formed in. In GaN the diffusion length of the charge carriers is 50–60 nm [76, 77]. The knowledge of the size of the interaction volume and which electron beam parameters influence it are crucial for CL imaging with high spatial resolution. Spatial resolution of the CL signal will be addressed in the following Section 3.4.

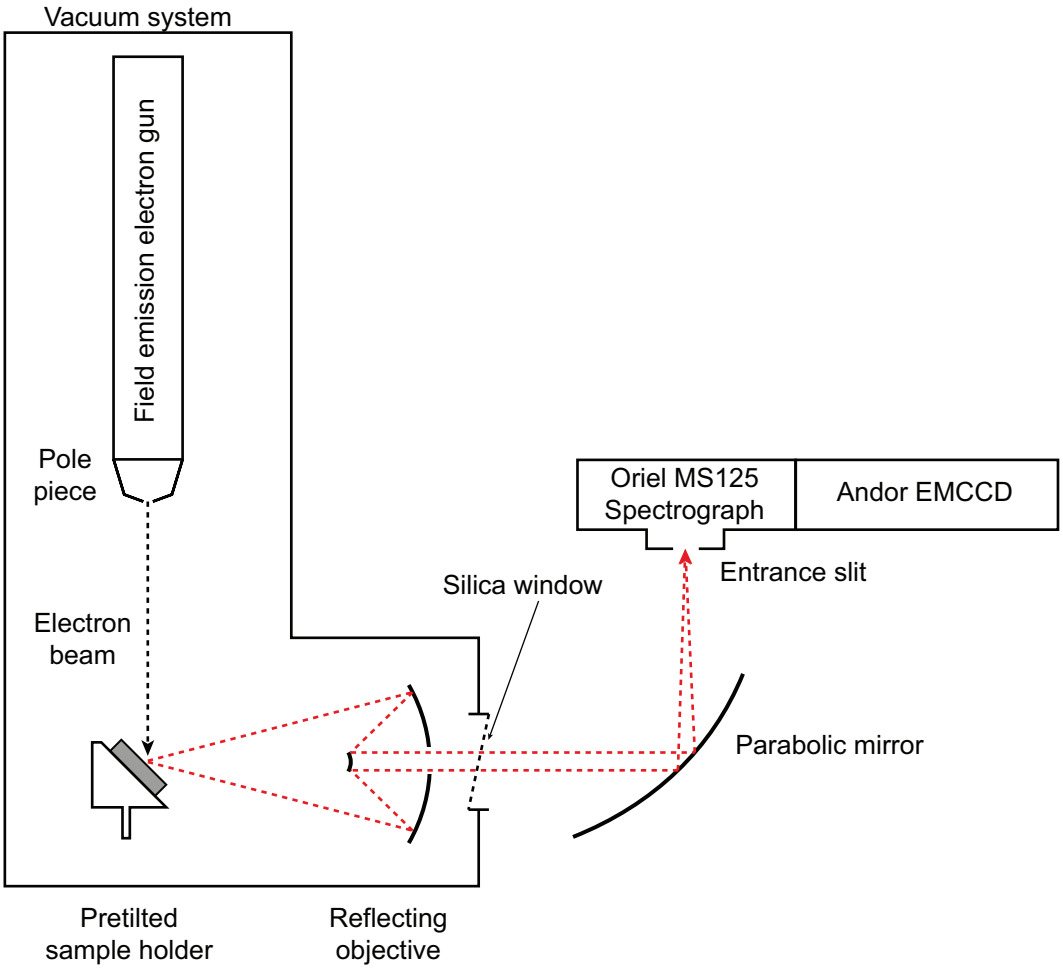

Figure 3.9: *Schematic diagram of the home-built CL system. The system is attached to a field emission gun electron microscope.*

The CL system used for hyperspectral imaging is a homebuilt system designed by Dr. Paul R. Edwards, which is attached to a commercial FEGSEM (*FEI Sirion 200*). A schematic of the system is shown in Fig. 3.9. The advantage of a FEGSEM is the possibility of using very small, high-brightness spots at low beam energy; the smallest electron beam spot diameter of the SEM used is approximately 1 nm. The electron beam is perpendicular to the axis of the detection optics. To facilitate better light collection the sample is mounted on a stub which is pretilted by 45°. The emitted light is collected and collimated by a Schwarzschild-type reflecting objective (numerical aperture of 0.28) and fo-

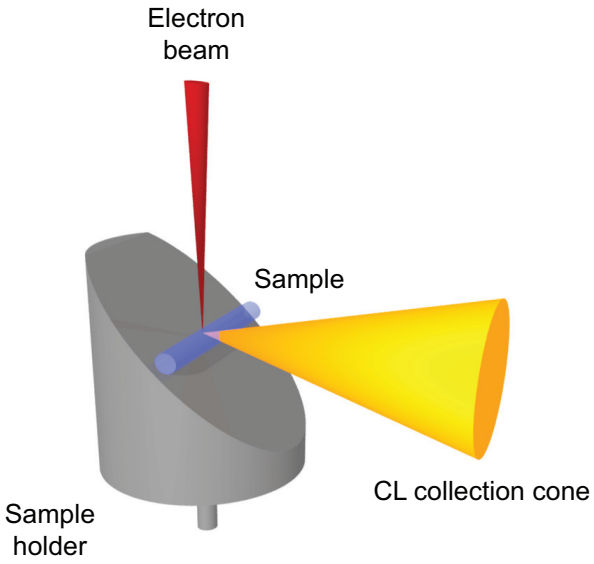

Figure 3.10: *Schematic diagram of the light collection geometry. The sample is placed on a pretilted (45°) holder. The axis of the light collection optics is perpendicular to the electron beam. The sample in the schematic shows a nanorod.*

cused onto the entrance slit (25, 50 or 100 μm) of a 1/8 m spectrograph (*Oriel MS125*) with exchangeable diffraction gratings using an off-axis paraboloidal mirror. The light is detected by an electron-multiplying CCD (*Andor Technology Newton DU971N*). The advantage of using a reflecting objective is the lack of either chromatic aberration or absorption at short wavelength. Additionally, the use of off-axis light collection means there is no object between the pole piece of the microscope and the sample and the use of smaller working distances or tilting of the sample is possible. The choice of an electron-multiplying CCD increases the signal-to-noise ratio and makes it possible to reduce the acquisition time, which is needed for high resolution imaging due to possible image drift. The CL measurements are performed at room temperature. The light collection geometry with the pretilted sample holder is illustrated in Fig. 3.10.

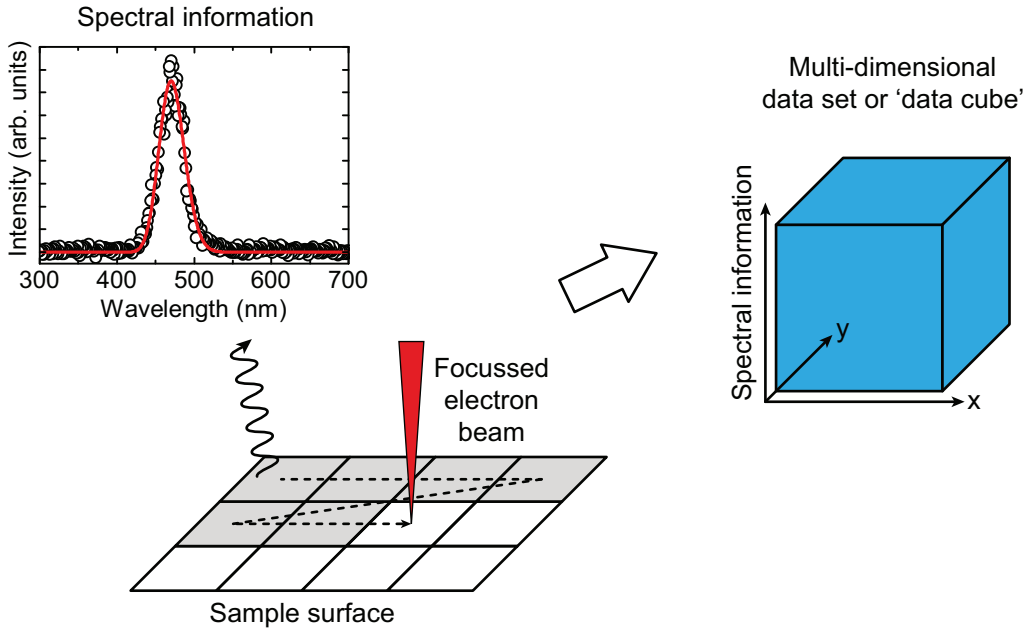

Figure 3.11: *Schematic diagram of the CL hyperspectral imaging process.*

3.4 Cathodoluminescence hyperspectral imaging

Conventional CL imaging either records a panchromatic or monochromatic CL image. For panchromatic CL the total luminescence intensity is measured, whereas for monochromatic CL the intensity within a specific wavelength interval is chosen. By contrast, CL *hyperspectral imaging* is a more powerful technique in which an entire luminescence spectrum is recorded at each pixel in an image created by a scanning electron beam [105, 106]. The result is a multi-dimensional data set allowing the maximum information to be extracted from variations in luminescence spectra across the sample. Having the entire spectral information stored in each pixel in a CL image makes it possible to extract information about intensity variations, changes in peak width and energy shifts, which is not possible in conventional CL mapping.

For collecting CL hyperspectral images the scanning capability within the SEM is exploited. A schematic of the acquisition process can be seen in Fig. 3.11.

Afterwards the data set can be treated mathematically to extract images describing subsets of the recorded data. In general, the peaks in each spectrum in the data set are numerically fitted by Gauss, Lorentz or Voigt functions and the re-

sulting fitting parameters (i.e. energy peak position, peak area, peak half-width) are plotted against the position on the sample surface to produce two-dimensional (2D) maps. Another mathematical tool is principal component analysis (PCA), a multivariate statistical analysis technique, which can be applied to transform a huge data set into a smaller one with only the most important components contributing to the information [107]. This is particularly useful when dealing with low signal-to-noise spectra, where curve fitting is not applicable [108].

The optimum parameters for high resolution CL imaging are a low acceleration voltage to minimise the excitation volume, a small electron beam size and short acquisition times to avoid image drift. In the following discussion, CL resolution refers to the spatial resolution of the measurement. The CL resolution is mostly influenced by the size of the excitation volume, the electron beam size and the carrier diffusion length in the studied material [109]. An electron beam spot size of about 1 nm can be achieved by using a modern FEGSEM. The spot size is smallest for large acceleration voltages and small beam currents. This, however, gives low resolution due to an increased excitation volume and a low intensity CL signal. As discussed previously, the excitation or interaction volume becomes smaller with decreasing acceleration voltage. The lateral size of this volume can be estimated to be roughly equal to the penetration depth of the electron beam [110]. If the features of interest in a sample are far below the surface of the sample, a higher electron beam energy is required and therefore the resolution is lowered. The volume where the CL signal is produced, however, is larger than the excitation volume due to the diffusion of the generated electron–hole pairs. The diffusion length is material dependent and for GaN it is 50–60 nm [76, 77]. The smallest spatial resolution of a CL measurement performed on bulk GaN will therefore be ultimately limited by the diffusion length. Calculations, however, show that the excess carrier density in the three-dimensional case decreases faster than exponential [111]. This means that carrier redistribution through diffusion does not significantly increase the excitation volume and therefore influence the spatial resolution. The diffusion length, though, is a bulk property. Confinement in nanostructures, such as QWs, small surface features or defects, further limits the diffusion of the generated carriers by either increasing or decreasing the probability of radiative or non-radiative recombination. This allows features several orders of magnitude smaller than the diffusion length to be

observed [110, 112, 113]. Other resolution limiting effects include surface contamination by carbon, charging of the sample, mechanical vibrations and electrical noise [112]. It should be noted that this description applies to CL resolution when using an SEM in contrast to a transmission electron microscope (TEM), where the samples are thinned down to a thickness of the order of 100 nm.

CL hyperspectral images were recorded by *Cathodoluminescence Hyperspectral Imaging and Manipulation Program* (CHIMP) a custom-written program by Dr. Paul R. Edwards, which externally controlled the electron beam for CL image acquisition. The software also includes image analysis tools, such as the previously described numerical peak fitting and PCA.

3.5 Electron channelling contrast imaging

In Chapter 4 results will be presented on CL and electron channelling contrast imaging (ECCI) performed on the same micron-scale area of a sample. All ECCI measurements were performed and the results analysed by Dr. G. Naresh-Kumar and Dr. Carol Trager-Cowan at the Department of Physics, University of Strathclyde. The following gives a short description of electron channelling following Refs. [114, 115].

Due to the electron's wave–particle duality electron channeling can be explained either using a simplified particle description or by Bloch waves. Fig. 3.12(a) shows a periodic crystal lattice with atoms lined up in planes. In contrast to an amorphous material where the packing density is uniform, the packing density appears to be reduced in certain directions in a crystalline material because of the line up of atoms into planes. For certain incident angles electrons can move parallel to these planes and the backscattering probability is reduced.

This picture is not an entirely complete description, especially when the electron beam energy is of a few tens of keV. In this case the wave nature of the electron is more significant and the channelling process is described by the diffraction of the electrons by the crystal lattice. The electron flux is mathematically described by a number of standing waves, referred to as Bloch waves, which have the periodicity of the lattice. The wave fronts are parallel to the surface normal and in the simplest case the current travelling through the lattice can be described by two Bloch waves. Type II Bloch waves have their intensity maxima in the centre

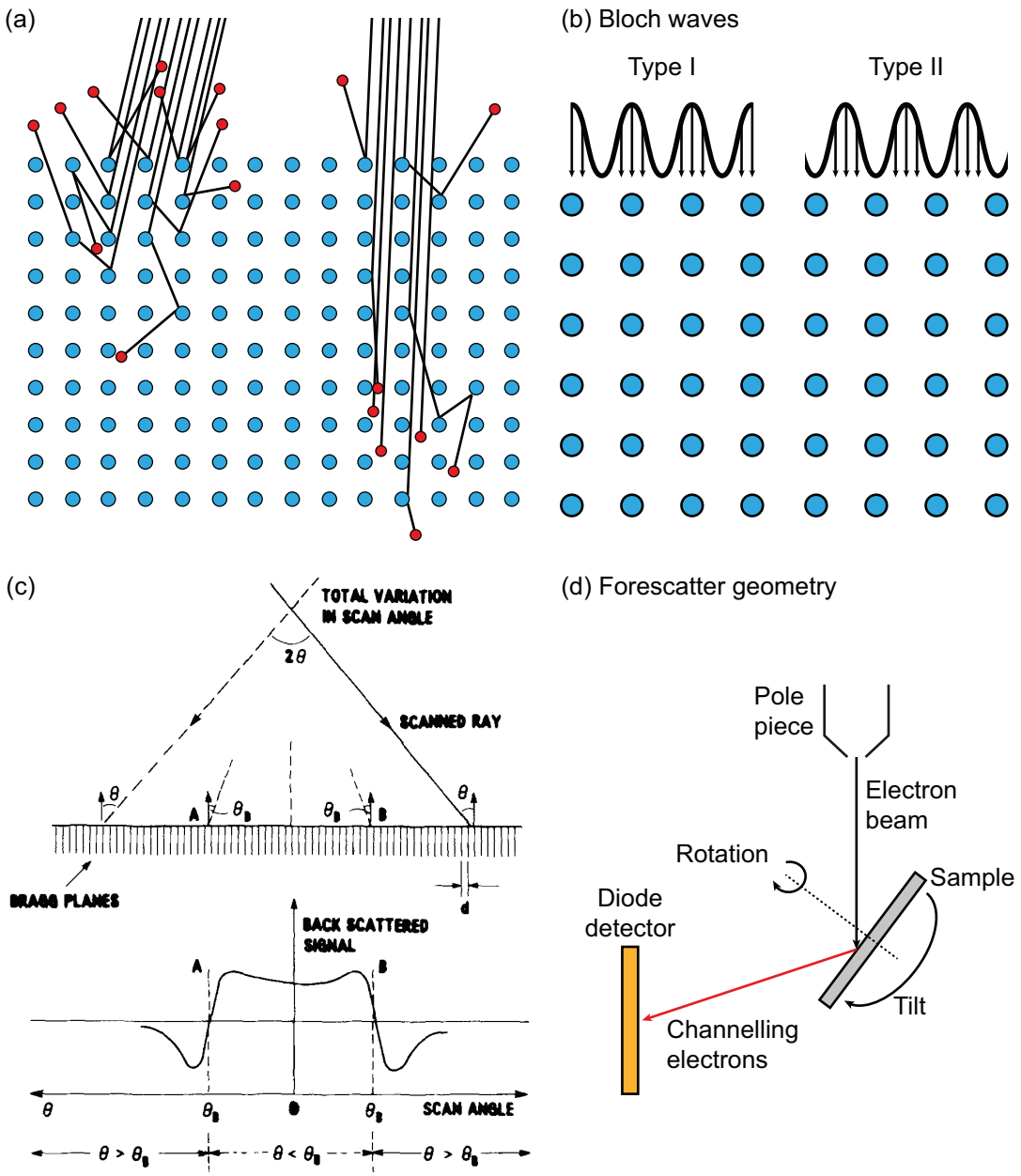

Figure 3.12: *(a) Electron channelling effect described by the particle model. For certain incident angles the electrons can move parallel to planes of atoms and the backscattering effect is reduced. (b) Wave description using Bloch waves of type I and II. (c) Backscattered signal as a function of incident angle θ. Points A and B on the sample are equivalent to $\theta = \theta_B$, where both types of Bloch waves have the same intensity. Illustration taken from Ref. [114]. (d) Schematic diagram of the ECCI geometry in forescatter configuration.*

between the lattice planes and therefore interact weakly with the lattice leading to a weak backscattering yield. Whereas type I Bloch waves have their maxima along the lines of atoms exhibiting strong backscattering due to the proximity to the atoms. Both types of Bloch waves are schematically shown in Fig. 3.12(b). The square of the amplitude of the Bloch waves corresponds to the probability of finding an electron at any point or, macroscopically, the current density. The intensity of each Bloch wave is determined by the incident angle θ of the electron beam and the lattice spacing d. When the Bragg condition

$$2d \sin \theta = \lambda \tag{3.8}$$

with λ being the electron wavelength, is satisfied, then both Bloch waves are of equal intensity. For angles smaller than the Bragg angle ($\theta < \theta_B$) the intensity of type I Bloch waves is greater the intensity of type II and the backscattered intensity is increased. For $\theta > \theta_B$ the opposite is observed. Scanning the electron beam over a sample surface, i.e. varying the incident angle, two points A and B are observed, which are equivalent to $\theta = \theta_B$, where the two Bloch waves are of equal intensity. Between point A and B ($\theta < \theta_B$) the backscattered signal is increased. This is illustrated in Fig. 3.12(c), which also shows the backscattered signal as a function of incident angle.

Performing a two-dimensional scan in an SEM will show diffraction from sets of planes (nearly) parallel to the incident electron beam. This results in bands of contrast, also known as an *electron channelling pattern* (ECP). The widths of these bands are twice the Bragg angle θ_B and the angles between the bands correspond to the angles between sets of lattice planes. An ECP may be recorded in an SEM under low magnification, when the angle the electron beam makes with the sample changes as it is scanned.

In another mode of operation the SEM is operated at high magnification, where the angle between the beam and the sample is essentially constant. In this case, the contrast is generated whenever the electron beam scans across areas of different crystal orientation or different lattice constants due to strain variations which change the backscattered signal. This mode is referred to as *electron channelling contrast imaging*. This allows low-angle tilt and rotation boundaries, atomic steps and threading dislocations to be imaged [116]. Fig. 3.12(d) shows

the geometry of the setup for which the detector is placed in front of the tilted sample.

ECCI can also be used to detect and unambiguously identify the three types of TDs, namely edge, screw and mixed types, in nitride semiconductors of wurtzite crystal structure. This can be achieved without the need of any sample preparation as would be necessary for identification using a TEM. TDs appear as spots with black–white (B–W) contrast caused by the strain field of the dislocations. For the identification of the TDs two images are taken with channelling conditions for two symmetrically equivalent crystal planes with **g** vectors at 120° to each other. Comparison of these two images shows a change of direction of the B–W contrast of the dislocations and is described in Ref. [117].

ECCI measurements were carried out using an FEGSEM (*FEI Sirion 200*), an electron-sensitive diode and a custom-built signal amplifier (*K.E. Developments Ltd.*).

Chapter 4

Coincident cathodoluminescence, electron channeling contrast and atomic force imaging of threading dislocations in GaN

4.1 Introduction

Most nitride-based devices consist of a relatively thick (a few μm) GaN layer located between the substrate and the actual device layers, such as the MQW structure for light-emitting diodes.

The lack of suitable lattice-matched substrates leads to the appearance of TDs, which are formed during the initial stages of growth of GaN on the substrate due to their large lattice mismatch (14% for sapphire) and difference in thermal expansion coefficients. Despite such a high density of TDs ($10^7 - 10^{11}$ cm^{-2}) devices based on the III-nitride system are still functional and exhibit relatively high efficiencies in comparison to their counterparts in the arsenide and phosphide systems with similar dislocation densities [118]. Therefore, it was thought that dislocations in the III-nitride system do not significantly influence their opto-electronic properties. However, it was shown by a comparison of atomic force microscope (AFM) and CL images with simulations that dislocations in GaN indeed can act as non-radiative recombination centres [119].

Dislocations can be classified into three types: pure edge with an a-type Burgers vector, pure screw with a c-type Burgers vector and mixed with $(a+c)$-type Burgers vector. Pure edge- and mixed-type are the predominantly observed TDs in MOCVD-grown GaN, whereas pure screw-type TDs only amount to a few percent [120].

TDs can have various effects on the optical and electrical properties, such as introducing energy levels within the band gap leading to other recombination channels besides near band edge recombination or act as scattering centres affecting the carrier transport.

The influence of the dislocation type on the optical properties, including whether they are radiative or non-radiative centres for recombination, shows strong ambiguity in the literature. Sugahara et al. have found that all types of dislocations in homo- and heteroepitaxial GaN act as non-radiative recombination centres for minority carriers as seen in transmission electron and CL images [77]. Hino et al. on the other hand discovered evidence in AFM, SEM and PL measurements that only dislocations with a screw-component (screw- and mixed-type) act as centres for non-radiative recombination, whereas edge-type do *not* behave that way [121]. The opposite was reported by Albrecht et al., who found evidence in thick homoepitaxial GaN layers that only dislocations with an edge-component (edge- and mixed-type) are recombination active [122]. With that the authors say that only edge- and mixed-type dislocations are centres for non-radiative recombination and screw-type dislocations have *no* impact on the luminescence, i.e. produce no dark spots in CL image.

Besides influencing the optical properties of GaN-based devices, dislocations can also impact on their electrical performance. High current densities and low effective Schottky barrier heights were observed in areas close to dislocations having a screw-component in an n-doped GaN film [123]. Dangling bonds near edge-type dislocation in AlGaN form acceptor-like states, which reduce the free carrier concentration and mobility with increasing edge dislocation density [124]. The same authors also correlate a decrease of PL intensity with increasing edge-type dislocation density to these dislocations being centres for non-radiative recombination. Furthermore, a reduction of TD density showed a drastic decrease of reverse-bias leakage current in GaN p-n junctions [125].

In this chapter, optical and structural analysis of TDs in a Si-doped c-plane

Figure 4.1: *Schematic of the sample structure of the Si-doped c-plane GaN epilayer. The Si concentration increases from* 5.5×10^{17} *to* 1.0×10^{19} cm^{-3} *in the bottom four n-type GaN layers. The Si concentration of the top GaN layer is* 1.0×10^{18} cm^{-3}.

GaN epilayer are carried out using CL hyperspectral and electron channeling contrast imaging (ECCI) on the same micron-scale area. TD density and dislocation type are estimated and verified by an independent measurement using AFM.

4.2 Sample description

The investigated sample was grown at the University of Cambridge using a Thomas Swan 6×2-inch close-coupled showerhead MOVPE reactor. The precursors were trimethylgallium, silane at 50 ppm in H_2 and ammonia, with H_2 as carrier gas. (0001) orientated sapphire (*c*-plane) served as a substrate. A nominally 30 nm thick GaN nucleation layer was grown before a 5 μm thick coalesced GaN layer, which formed after three-dimensional island growth. Afterwards, a multilayer containing four n-doped 200 nm thick GaN layers with increasing Si-doping concentration (5.5×10^{17}–1.0×10^{19} cm^{-3}) separated by 200 nm thick undoped GaN spacer layers was formed. Finally, another 200 nm thick GaN spacer layer followed by a Si-doped GaN layer with a Si concentration of 1.0×10^{18} cm^{-3} as the

top layer were grown. A schematic of the sample structure is shown in Fig. 4.1.

This sample, supplied by Dr. Rachel A. Oliver from the University of Cambridge, was used as a calibration structure for scanning capacitance microscopy and further sample details can be found in Ref. [126].

4.3 CL, ECCI and AFM of GaN

Due to the complicated, multilayered structure of the sample the probing depth of the electron beam is an important factor and therefore choosing the correct electron acceleration voltage is essential for the CL and ECCI measurements.

Before investigating the luminescence and defect properties of the GaN sample, the surface morphology was studied by SE imaging as seen in Fig. 4.2(a). Besides a few dark, irregular spots, either due to surface contamination or an incompletely coalesced layer, the surface appears to be smooth.

To investigate the luminescence properties of the GaN epilayer CL hyperspectral imaging, as described in Section 3.4, was performed on the same area as seen in the SE image in Fig. 4.2(a). To ensure that the excitation volume only penetrates the first epilayer (200 nm of GaN:Si), and not the multilayer structure below it, a small enough acceleration voltage needs to be chosen. In this case 5 kV was selected since the penetration depth is less than 200 nm as shown by Monte Carlo simulations in Figs. 3.6 and 3.7 when the electron beam hits the sample perpendicularly. However, in the current CL system the electron beam hits the sample under an angle of 45°, consequently reducing the penetration depth.

The room temperature CL spectra exhibited one peak at 3.43 eV corresponding to near band edge recombination in GaN. Each spectrum was then numerically fitted using a Voigt function, as shown in an example spectrum in Fig. 4.3. The integrated intensity and peak energy map constructed from the fitting parameters are displayed in Figs. 4.2(b) and (c), respectively.

The CL intensity map (Fig. 4.2(b)) exhibits dark spots of various diameters. There is no clear relation between the dark spots in the SE and CL intensity image. These dark spots in the CL image are centres of non-radiative recombination and can be related to TDs [119, 77]. Larger dark spots are clusters of two or more dislocations in close proximity. CL mapping of dark spots is a quick and non-destructive tool for estimating the TD density [127, 128]. However, if the

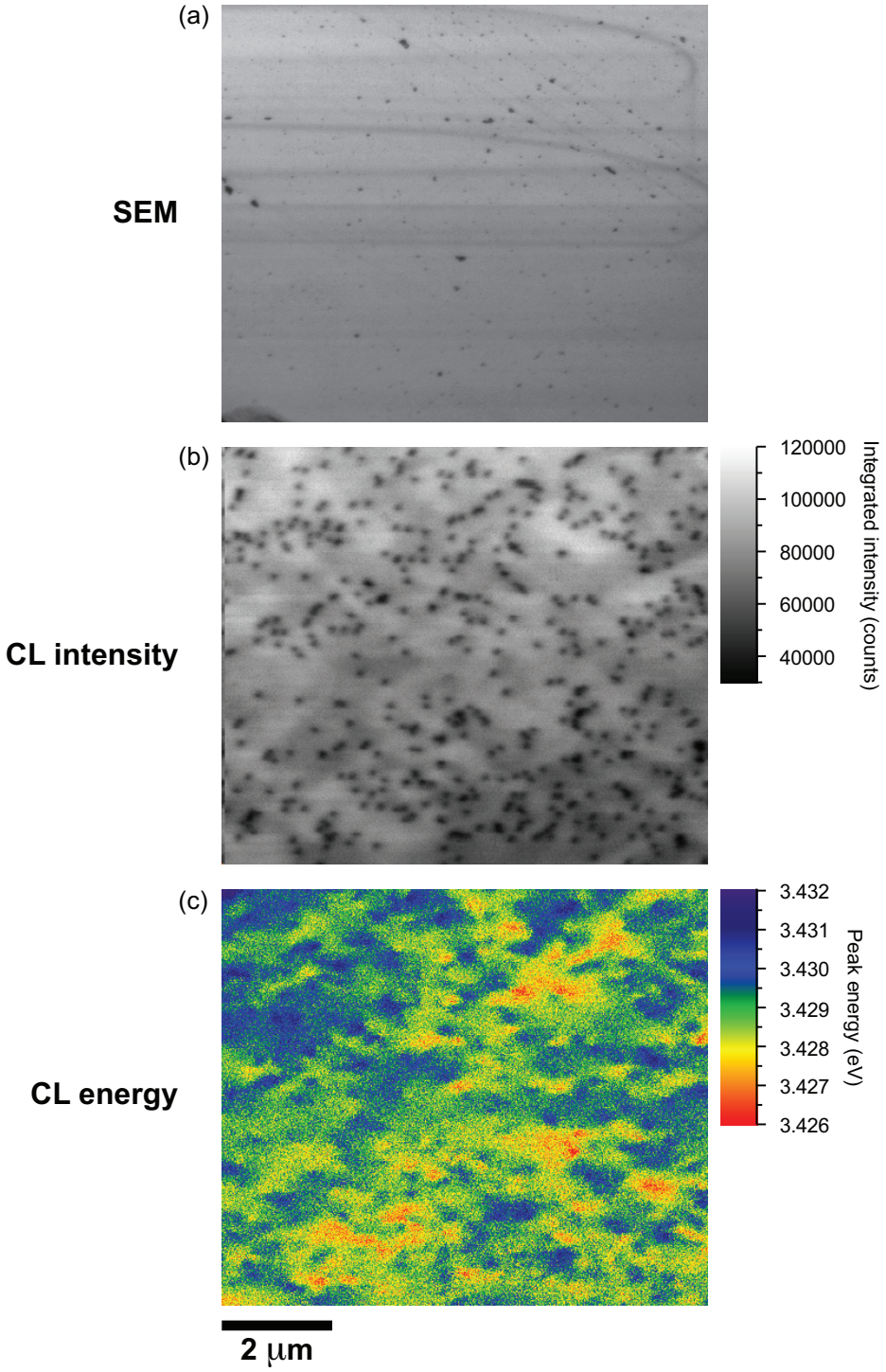

Figure 4.2: *(a) SE image, (b) integrated CL intensity and (c) peak energy map of the fitted GaN emission peak of a Si-doped c-plane GaN epilayer. The dark spots represent TDs, which are centres for non-radiative recombination. The streaks in the SE image are due to carbon deposition as the electron spot was moved to the region under investigation.*

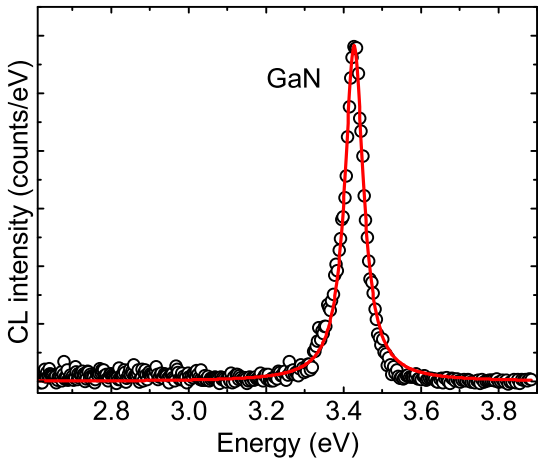

Figure 4.3: *Example spectrum showing the GaN near band edge emission peak, which was numerically fitted with a Voigt function.*

TD density is too high and/or the TD are to close together the density can be underestimated and the relative error for the density increases.

The energy map (Fig. 4.2(c)) displaying the GaN emission peak at about 3.43 eV shows a small energy variation of less than 10 meV across the imaged area. This variation of the emission energy can be caused by a change of the strain state and/or fluctuations in the Si dopant concentration leading to microscopic potential fluctuation across the GaN film [129]. The room temperature transition energy of the A exciton in single-crystal wurtzite GaN films occurs at 3.42 eV, which represents the emission energy of the unstrained state of bulk GaN [130]. Since the measured emission energy is slightly higher than the bulk value the investigated Si-doped GaN epilayer suffers from a small compressive strain. GaN grown on sapphire is under compressive stress, mainly due to the difference in thermal expansion coefficients [131]. Si-doping on the other hand introduces tensile stress with increasing Si concentration [132, 133]. In a compressively strained GaN layer the emission peak is shifted towards higher energies. However, the tensile stress introduced by the Si doping has the opposite effect and decreases the GaN emission energy. The result is a less compressively strained GaN layer with an increased emission energy compared with unstrained GaN. In this case the energy increase is about 10 meV. It should be mentioned that the cause of the tensile stress in Si-doped GaN is still under debate and the exact effect of

doping on the strain state in GaN is unclear, however dislocation inclination and dislocation pinning play a role [134, 135].

CL imaging of the GaN film showed the presence of TDs. In order to understand the nature of these TDs it is important to determine an accurate number for the TD density and identify the dislocation type. A rapid and non-destructive method is ECCI as described in Section 3.5. ECCI measurements and analysis were performed by G. Naresh-Kumar at the University of Strathclyde.

For the identification of the dislocation type two electron contrast channeling images were taken from two symmetrically equivalent crystal planes using an acceleration voltage of 30 kV, as displayed in Fig. 4.4. Large scale areas showing different grey scale in the image correspond to regions of different tilt or twist across the sample. TDs appear as spots with B–W contrast. The bright spot in the centre of the images is a dust particle, which was used for identification of the area and alignment of the two electron contrast images. Using the procedure described in Ref. [117], which compares the changes in direction of the B–W contrast in these two images, shows that 60% of the dislocations are edge-type, fewer than 2% are screw-type and the remainder are mixed-type. The total TD density was estimated from a number of electron channeling images to be $(5.1 \pm 0.4) \times 10^8$ cm^{-2}.

In order to correlate the dark spots in CL intensity images and spots with B–W contrast in electron contrast images, measurements using both techniques were performed on the same micron-scale area. To verify the TD density and their type, AFM (*Digital Instruments Dimension 3100*) measurements were also carried out on the same area of the sample by Dr. Rachel A. Oliver at the University of Cambridge. TDs create small pits upon termination on the sample surface. To enlarge these pits and make them easier to detect in AFM the sample underwent a post growth treatment using SiH_4 and NH_3 directly after the growth in the MOVPE reactor. The pit size also varies with dislocation type; edge dislocations having smaller diameters than dislocations with a screw-component [136].

To find the same area for the individual measurements an undamaged region located on one end of a scratch was chosen. Carbon contamination in the area where the ECCI measurement was performed was then used for alignment for CL imaging. The AFM is equipped with an optical microscope which was used to locate the scratch and a large area AFM scan was performed to find the same

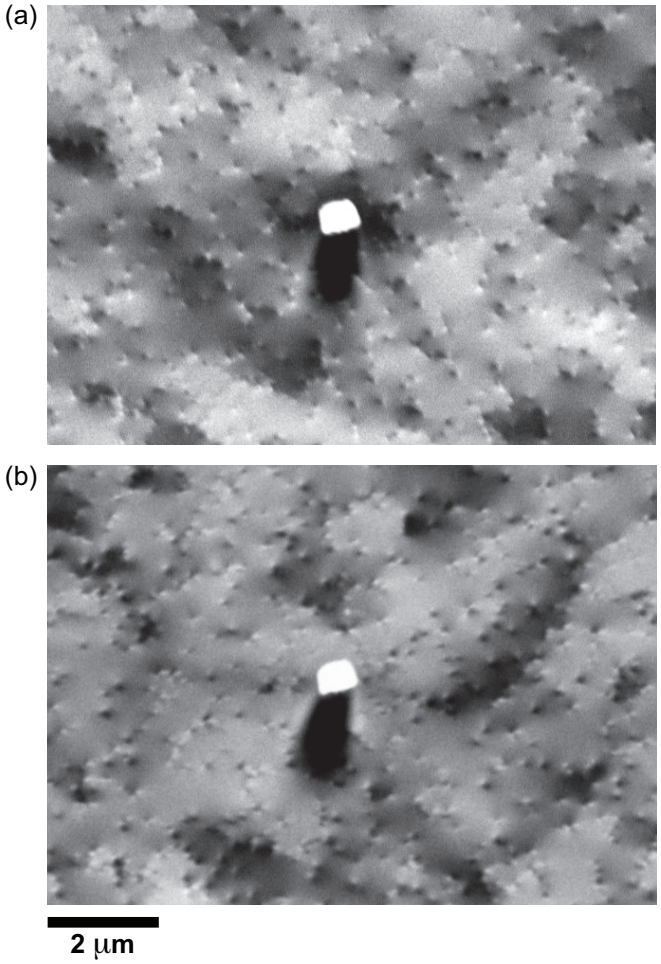

Figure 4.4: *Two electron contrast channeling images taken from two symmetrically equivalent crystal planes for identification of the dislocation type. The bright spot in the centre is a dust particle used for finding the same area. Measurements were performed by G. Naresh-Kumar at the University of Strathclyde.*

carbon contamination left by ECCI and CL.

The integrated CL intensity map of the GaN emission peak, electron channeling contrast image and AFM image of the same area are displayed in Figs. 4.5(a)–(c), respectively. The displayed images are part of larger images, but a smaller area is shown for clarity and to enlarge the detail.

The CL intensity map in Fig. 4.5(a) shows a large number of dark spots, some of them appearing in clusters. For a single dark spot with a diameter of about 150 nm to be isolated, i.e. resolved as one spot, it needs to be at least 400 nm

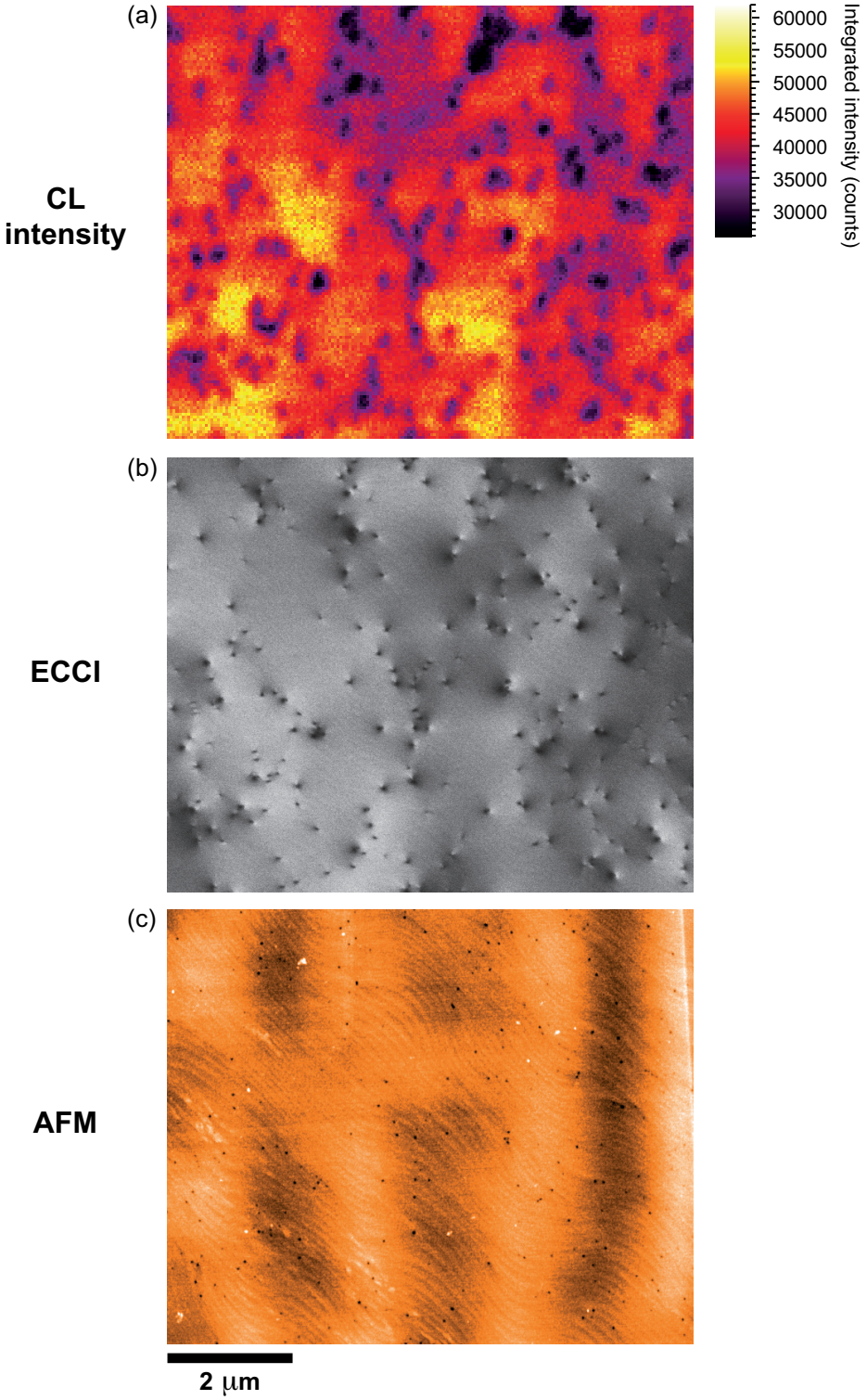

Figure 4.5: *(a) Integrated CL intensity map of the fitted GaN emission peak, (b) electron channeling contrast image and (c) AFM image of the same micron scale area of a Si-doped c-plane GaN epilayer. The ECCI measurement was performed by G. Naresh-Kumar at the University of Strathclyde and the AFM measurement by R. A. Oliver at the University of Cambridge.*

apart from its nearest neighbour. If TDs are less than 400 nm from its nearest neighbour the spots appear in clusters of darker spots of more than one TD.

The CL measurements were performed at a relatively high acceleration voltage of 5 kV, beam current of 6 nA and an electron beam spot diameter of about 20 nm in order to excite an intense enough band edge emission for mapping. Also carbon contamination from the previously-performed ECCI measurement within the imaged area reduced the CL signal making it necessary to excite the sample harder. This combination led to a reduced CL resolution and larger observed black spots. Under optimum conditions it should be expected that the CL resolution is only limited by the diffusion length and therefore the diameter of the black spots is twice the diffusion length in GaN (around 50 nm [76, 77]).

It is possible to discriminate between TDs in the electron channeling image in Fig. 4.5(b) if they are further than approximately 80 nm apart. For the entire data set approximately 750 TDs are found using the ECCI technique, with about 400 TDs being single and isolated according to the definition above. Careful comparison of the images in Fig. 4.5 shows a *one-to-one* correlation of the dark spots in the CL map, spots with B–W contrast in the electron channeling image and pits in the AFM image for these 400 isolated TDs.

From the AFM image in Fig. 4.5(c) of the same area where the CL and ECCI measurements were performed it was possible to identify the TDs of being either of edge-type (labelled "E") or as TDs having a screw-component, i.e. screw- or mixed-type (labelled "M"). The dislocation types are marked in Fig. 4.6. Comparison showed that isolated dark spots in the CL image correspond to TD of both edge- and screw-/mixed-type in the AFM image. Therefore, it can be concluded that pure edge dislocations and TDs with a screw-component act as centres for non-radiative recombination in the investigated Si-doped GaN layer. The results are inconclusive about pure screw dislocations acting as non-radiative recombination centres, because their density (<2%) is not high enough to identify single and isolated screw TDs for a comparative measurement.

Other features observed in the electron channeling image in Fig. 4.5(b) are TDs consisting of faint and elongated lines of B–W contrast of about 100 nm in length. These features could be projections of inclined edge dislocations since edge-type dislocations have been observed to bend in both Si-doped GaN layers and Si-doped $Al_{0.49}Ga_{0.51}N/Al_{0.62}Ga_{0.38}N$ [137, 138]. These faint, elongated TDs

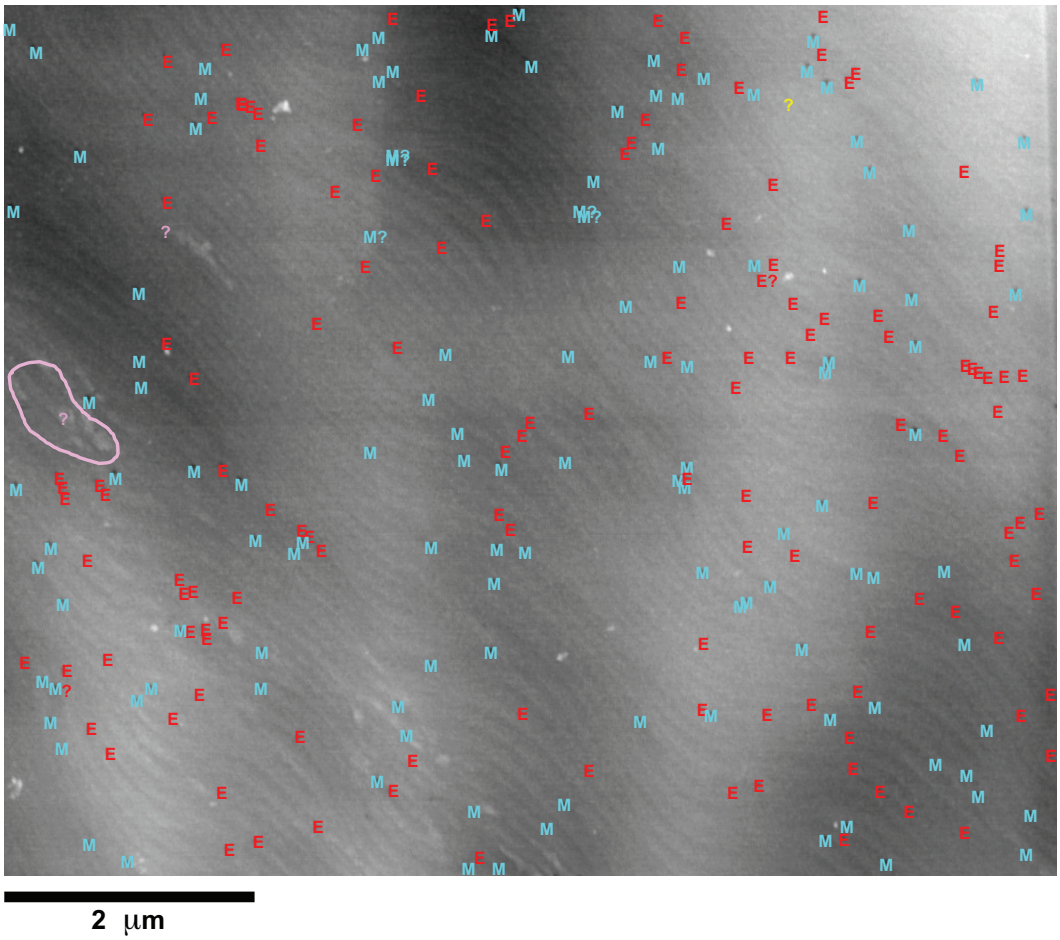

Figure 4.6: *AFM image from Fig. 4.5(c) with identification of the dislocations types. Pure edge dislocations are marked with "E", dislocations with a screw-component with "M" and unidentifiable TDs with "?". TDs labelled with "M" are probably mixed-type dislocations since fewer than 2% are screw-type. AFM measurement and identification of the dislocations were performed by R. A. Oliver at the University of Cambridge.*

were identified as edge-type TDs by correlation with the AFM image in Fig. 4.6.

The CL map in Fig. 4.5(a) exhibits another characteristic. Areas with the highest CL intensity coincide with regions free of dislocations showing a higher recombination efficiency. However, some regions without dislocations do not exhibit this behaviour but have intermediate CL intensity. The presence of other defects, such as point defects could be the cause for such a reduced CL intensity.

4.4 Summary

CL hyperspectral imaging and ECCI were combined and initial results of the optical behaviour of TDs in a Si-doped *c*-plane GaN epilayer are presented.

A strong correlation was found between TDs observed as dark spots in CL intensity maps and spots with B–W contrast in ECCI. A one-to-one correlation of single, isolated TDs was observed using both techniques. AFM imaging determined these isolated TDs to be either of edge-type or screw-/mixed-type. Therefore, it can be concluded that pure edge dislocations and dislocations with a screw-component are centres for non-radiative recombination.

However, to unambiguously determine the influence of the dislocation type on the optical properties a more suitable sample is necessary. Firstly, the TD density of the studied GaN epilayer was too high since most of the TDs appeared in clusters, which makes it impossible to determine individual dark spots in CL. Secondly, the sample showed fewer than 2% pure screw dislocations, which increased the difficulty of finding a single, isolated TD of this type in the investigated area and conducting a reliable correlation between CL and ECCI. Finally, the sample structure and Si-doping of the GaN film masked the influence of the strain field around TDs on the emission energy.

Also, the CL settings need to be carefully chosen to allow for optimum resolution. The size of the dark spots, which is approximately 150 nm, shows that the resolution is limited by the electron beam parameters. With a careful treatment of the sample and preceding ECCI measurement it is possible to gain a higher resolution, which will be limited only by the diffusion length of the sample. In that case the dark spot diameter would be twice the carrier diffusion length in GaN of around 50 nm.

Further CL and ECCI measurements need to be carried out on a simple GaN film with a low TD density and a more evenly spread ratio between the three types of TDs to investigate the recombination characteristics of each type of TD.

Chapter 5

Characterisation of planar InGaN/GaN multiple quantum well structures

5.1 Introduction

InGaN/GaN MQW structures are the building blocks of opto-electronic devices such as LDs and LEDs used in solid-state lighting. Band gap engineering and design of the MQW structure allow tuning of the emission wavelength through the entire visible spectrum, but there remains room for improvement of the IQE due to a range of material challenges facing the growth of InGaN. The IQE is a measure of how many carriers recombine radiatively in the MQW structure, which is defined by the quality of the material. Moving towards the green spectral range has detrimental effects on the emission properties. This is commonly referred to as the 'green gap' in the literature and its cause is still a matter of debate [139].

The structural and optical quality of these MQW structures is strongly dependent on the growth conditions and the choice of substrates. One essential parameter is the InGaN growth temperature, as it is used to control the incorporation of InN, which has a low miscibility in GaN. In order to avoid decomposition of the InGaN well, the GaN barrier layers separating the InGaN QWs are grown at much lower temperatures (700–800 °C) than normally used for high quality GaN films (900–1100 °C). Various different growth techniques have been developed to

improve the growth of InGaN/GaN MQWs, such as growing a protective thin GaN cap at the same temperature as the InGaN layer before starting the barrier growth at a higher temperature [140]. Furthermore, the large lattice mismatches between GaN, InN and the commonly used sapphire substrate (14% to GaN in (0001) orientation), and the difference in thermal expansion coefficients between GaN and the substrate, also lead to the formation of a high density of defects. To overcome the lattice mismatch advanced buffer layers were introduced before the growth of the epitaxial layers.

However, despite these efforts to improve the growth the III-nitride alloy system still suffers from a wide number of defects, including compositional fluctuations [141], TDs [142], misfit dislocations [143], stacking faults [144], grain boundaries [145] and V-defects or V-pits [146]. The latter is a well-known defect in InGaN MQW structures, where in general a TD terminates at the apex of an open hexagonal inverted pyramid with facets of $\{10\bar{1}1\}$ orientation [146]. TDs are caused by the large lattice mismatch and difference in thermal expansion coefficient between the epilayer and the substrate [147, 148] and originate at their interface. Despite the use of buffer layers to minimise these effects typical TD densities in the order of 10^7–10^{10} cm^{-2} are observed. These dislocations can act as non-radiative recombination centres and thus can reduce the overall efficiency of the device, making it important to understand their luminescence properties. There is also another type of defect which is seldom mentioned in the literature despite its existence being well-known amongst growers and its strong impact on the luminescence: the trench-like feature or trench defect [149, 150, 151, 113].

This chapter describes an investigation of planar InGaN/GaN MQW structures. Their optical characteristics are studied by temperature-dependent PL spectroscopy. The surface morphology exhibiting various features, such as V-defects and trench-like features, is analysed using scanning electron microscopy. CL hyperspectral images with high spatial resolution were taken to study the luminescence behaviour of these features, including shifts in emission energy as a function of position on the surface of the MQW samples. The SE and CL images allow the trench defects to be categorised into several different types. Finally, cross-section TEM allows further characterisation of the trench defects.

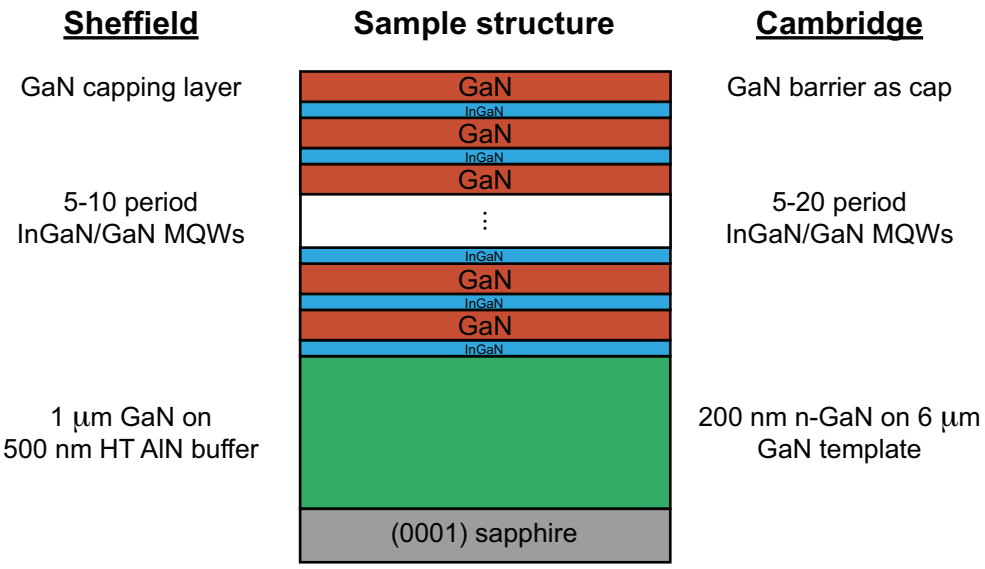

Figure 5.1: *Schematic of the InGaN/GaN MQW structures grown at the Universities of Sheffield (left) and Cambridge (right).*

5.2 Sample description

In this section two sets of samples with similar InGaN/GaN MQW structures from the Universities of Sheffield and Cambridge were investigated. A schematic of the sample structures from these two growth facilities is displayed in Fig. 5.1, with the generalised structure shown in the centre and growth specifics highlighted to the left and right.

The InGaN/GaN MQW structures from the University of Sheffield were grown by low pressure MOCVD on (0001) sapphire. To overcome the lattice mismatch a high-temperature atomically flat AlN buffer layer was employed [93]. The buffer consisted of a $\approx$ 500 nm thick AlN layer deposited on the sapphire substrate at 1150–1200 °C. After a 1 μm thick GaN layer, InGaN/GaN MQW structures with varying numbers of wells were grown followed by a GaN capping layer of the same thickness as the GaN barriers or thicker. The well and barrier widths were in the ranges of 1–3 nm and 8–12 nm, respectively, with five to ten periods and an InN content between 10% and 25%.

A series of MQW structures with increasing number of InGaN wells were grown at the University of Cambridge using a Thomas Swan 6 $\times$ 2-inch close-

coupled showerhead MOVPE reactor. A 6 μm thick low-defect-density GaN layer (TD density $\approx 4\times10^8$ cm^{-2}) grown on a 2-inch (0001) sapphire substrate served as growth template. After a 200 nm thick n-doped GaN layer, five to twenty period InGaN/GaN MQW structures were deposited on the template with nominally 2.5 nm thick wells and 7.5 nm thick barriers. Trimethylgallium, trimethylindium and ammonia were used as the sources for gallium, indium and nitrogen. The carrier gas during the GaN template growth was hydrogen, with nitrogen used during the MQW growth. A quasi two-temperature growth was used for the MQW structure, where a $\approx$ 1 nm protective GaN layer was grown after the InGaN layer using the same temperature. The growth was then continued while the temperature was ramped to a higher temperature for the GaN barrier layer. The emission peak of the MQW structures peaks at around 460 nm. Sample details can be found in Refs. [152, 153].

5.3 Photoluminescence

The emission energy, or wavelength, of InGaN/GaN MQWs is essentially defined by the width and the depth of the QWs and the band offsets of the conduction and valence bands of the semiconductors forming the QW structure. The width corresponds to the thickness and the depth to the InN content of the InGaN layer. Fig. 5.2 shows the room temperature PL spectra of six different InGaN/GaN MQW samples emitting from the violet to the green provided by the University of Sheffield. The samples in Fig. 5.2(a) were measured with a lower laser power density than those in Fig. 5.2(b).

Various differences between the emission spectra of the six samples can be observed. The main emission peak, with an energy between about 2.4 eV and 3.1 eV depending on the sample, results from photo-generated carriers becoming localised in the well region and recombining there. The energy shift (bottom to top spectrum) is caused by a combination of increasing InN composition and change in well width. Also, with increasing redshift the half-width of the peak increases due to inhomogeneous broadening caused by QW width fluctuations, compositional fluctuations of the InN content or changes in strain [154, 155].

The samples measured with the lower laser power, as seen in the spectra in Fig. 5.2(a), show an additional much broader peak at lower energies. This peak

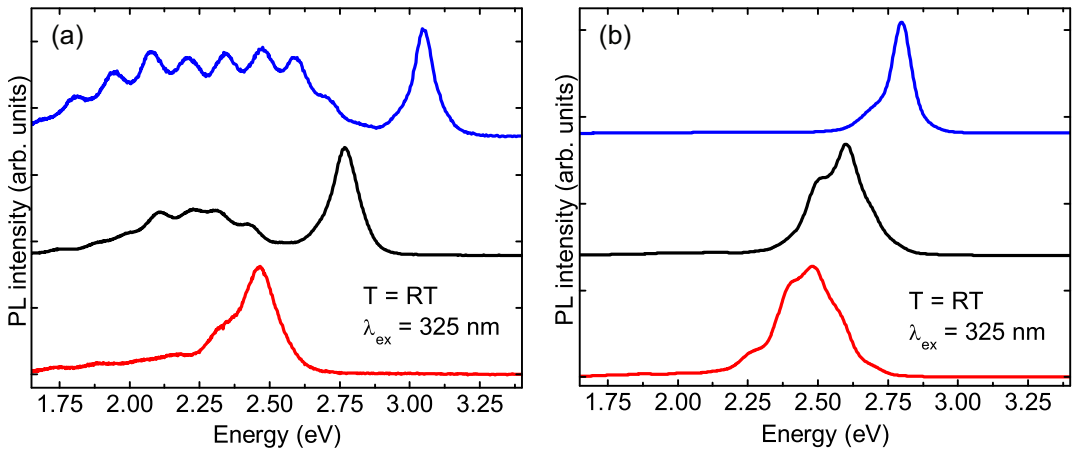

Figure 5.2: *Room temperature PL of six different samples at (a) low and (b) high excitation power density.*

is caused by recombination at levels within the band gap caused by defects and impurities in GaN layers and is referred to as yellow luminescence in the literature. There is still ambiguity about the origin, but it is speculated that the yellow band is caused by transitions involving a combination of deep or shallow donor and acceptor states [156, 157, 158]. Various theoretical and experimental investigations have been carried out to find the physical cause for these levels within the band gap of GaN. The findings include that nitrogen vacancy, gallium interstitials [159, 160] and nitrogen antisites [161] act as donors, gallium vacancies [162, 163] as a deep acceptor and more recently carbon was identified as a deep acceptor [164]. At higher excitation energies this defect band saturates and all additional carriers diffuse towards the QW and recombine there. The main emission peak thus becomes dominant over the yellow band. Also, the broad peak is decorated by smaller oscillations known as interference or Fabry–Perot fringes [40, 165]. They are caused by internal reflections at the air–GaN and GaN–substrate interfaces due to the large differences in refractive indices.

For further analysis of the QW emission, PL spectra between 16 K and room temperature were recorded for a blue-emitting InGaN/GaN sample from Fig. 5.2 at three different laser power densities (25, 65 and 450 W/cm^2). For clarity Fig. 5.3 only shows the 16 K and room temperature spectrum at each power density. As an example Fig. 5.4(a) displays the entire temperature series for the

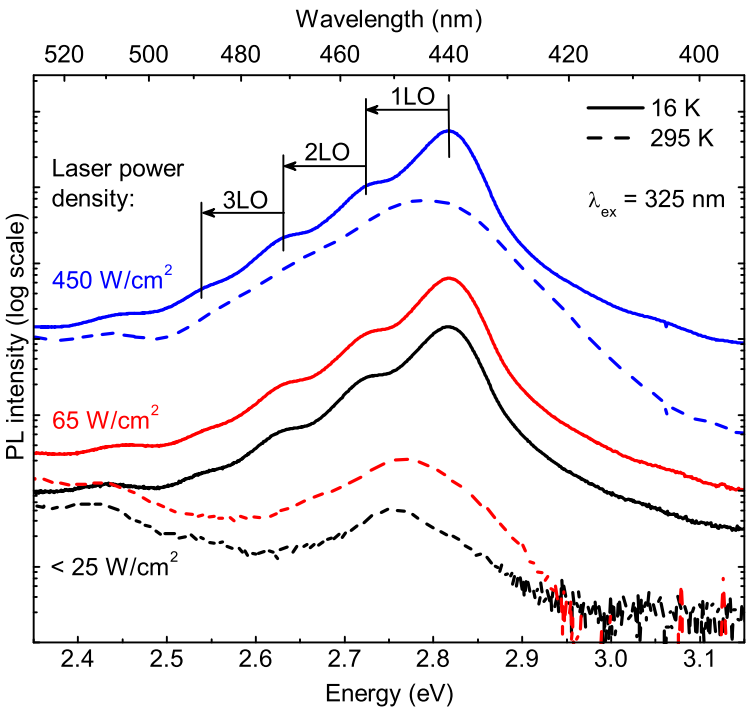

Figure 5.3: *Temperature-dependent PL series of a blue-emitting InGaN/GaN MQW structure measured at three different excitation power densities. For clarity only the room temperature and low temperature spectra at each power are shown.*

PL measurement at 450 W/cm^2.

The main emission peak just above 2.8 eV, as already mentioned above, is due to localised carrier recombination in the MQWs. Effects of the temperature on the emission can be observed from the spectra in Fig. 5.3. The MQW peak exhibits a redshift as temperature increases due to the temperature-dependence of the band gap, which is larger at 16 K than at room temperature. Its intensity is decreasing with increasing temperature, because of the activation of non-radiative recombination channels. There are at least three LO phonon replicas visible at 16 K on the low energy side, which are masked by the broadening of neighbouring peaks at room temperature.

By plotting the peak energy of the MQW emission as a function of temperature it can be observed that the energy shift with temperature exhibits an *"s-shaped"* behaviour (red–blue–redshift) as seen in Fig. 5.4(b). It cannot be explained simply by the shrinkage of the band gap usually described by the semi-

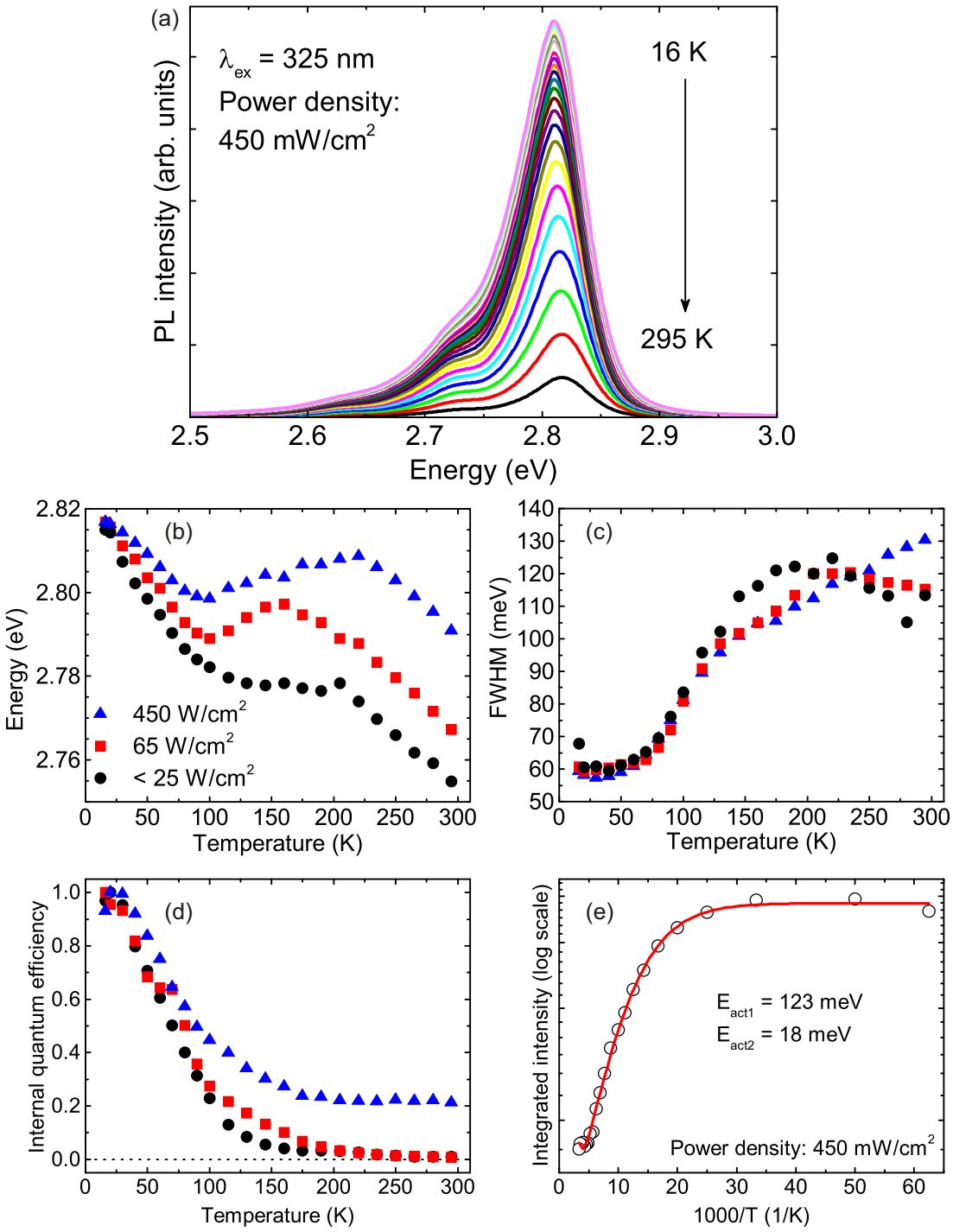

Figure 5.4: *Analysis of the blue-emitting sample from Fig. 5.3: (a) PL spectra measured at the highest excitation power density (450 mW/cm^2) from 16 K to room temperature. (b) Energy, (c) FWHM and (d) IQE as a function of temperature at three excitation power densities. (e) Arrhenius plot of the integrated intensity fitted for the determination of the activation energies. The plot for the measurement at the highest power is shown as an example.*

empirical Varshni equation [166] or the empirically found equation in Ref. [167]. This non-monotonous temperature behaviour is common for alloy semiconductors and is due to potential fluctuations caused by variations in either the composition (InN content) or interface (well width) [168, 169]. With increasing temperature, carriers can overcome these small potential fluctuations and drop to lower energy minima leading to a redshift of the emission. Upon further increasing the temperature the thermal energy is enough to overcome these larger potential fluctuations and excitons are no longer bound by them, causing a blueshift. However, the excitons are still localised within the QW. From there on the emission peak essentially follows the band gap decrease.

Another feature observed in Fig. 5.4(b) is the shift of the energy curve to higher energies when the excitation power is increased. As described in Section 2.3 nitride-based structures exhibit large electric fields along the c direction due to a change in spontaneous and piezoelectric polarisation between the InGaN and GaN layers. By increasing the excitation density of the PL measurement more carriers are generated which screen these internal electric fields. As a result the transition energy is blueshifted because the flat-band condition is approached and the influence of the QCSE is weakened, as schematically shown in Fig. 2.7 in Section 2.3. The blueshift is 2 meV at 16 K and 36 meV at room temperature.

This large difference in energy shift at low and high temperatures is unexpected. It should be pointed out that the measurements at these three laser powers were performed while modifying the PL setup. Various optical elements have been changed in order to transmit a higher percentage of the laser light for achieving a higher excitation density at the sample stage. Sample non-uniformity could play a role as well since the three measurements were performed on different pieces of the same wafer.

The full width at half maximum (FWHM) or linewidth of the MQW emission peak is plotted in Fig. 5.4(c). At low temperature the width is approximately 60 meV regardless of excitation power. With increasing temperature it exponentially increases until 100–150 K above which the width starts to deviate for the three power densities. As mentioned before the linewidth is mostly dominated by inhomogeneous broadening effects (well width fluctuations, compositional fluctuations, changes in strain) [154]. If homogeneous broadening alone were to account for the linewidth it would mainly be due to thermal broadening and of the order

Power density (W/cm^2)	E_{act1} (meV)	E_{act2} (meV)	η_{IQE} (%)
450	18	123	21
65	8	47	<1
25	11	54	<1

Table 5.1: *Calculated activation energies from fits of the temperature-dependent integrated intensity and IQE at room temperature for the blue emitting sample from Fig. 5.3.*

of k_BT. At room temperature this is approximately 25 meV in contrast to the observed 100–130 meV as shown in Fig. 5.4(c). Also, for the highest laser power the FWHM is still increasing above 180 K, whereas for the lower laser power densities the linewidths are slightly decreasing.

A measure of how many carriers recombine radiatively is given by the IQE, which is the ratio of the radiative recombination probability τ_r^{-1} and the total recombination probability τ^{-1} [20]. τ^{-1} is the sum of τ_r^{-1} and the non-radiative recombination probability τ_{nr}^{-1}. Conventionally, it is approximated by the ratio of the integrated PL intensity at temperature T and low temperature (here 16 K) assuming that all carriers recombine radiatively at low temperature [170]

$$\eta_{\mathrm{IQE}}(T) = \frac{\tau_r^{-1}}{\tau^{-1}} = \frac{\tau_r^{-1}}{\tau_r^{-1} + \tau_{nr}^{-1}} \equiv \frac{I(T)}{I(16\ \mathrm{K})}. \tag{5.1}$$

Fig. 5.4(d) shows the IQE as a function of temperature at three excitation densities. At high temperatures the IQEs of the measurement with the two lower power densities (25 and 65 W/cm^2) are almost approaching zero, which suggests that recombination takes place almost exclusively via non-radiative channels. In contrast, at the highest excitation density radiative recombination still occurs and the IQE at room temperature is about 21%. The room temperature IQEs are listed in Tab. 5.1. Amongst others, non-radiative recombination can be caused by defects, which will have a finite density. Although non-radiative recombination will increase with increasing temperature, a higher excitation power density will saturate these non-radiative recombination paths. The IQE therefore increases with laser power.

With increasing temperature non-radiative recombination channels are thermally activated. The non-radiative recombination probability τ_{nr}^{-1} can be es-

timated using a Boltzmann factor $e^{-\frac{E_{\mathrm{act}}}{k_B T}}$ for the generation of such a channel with necessary activation energy E_{act}. Since, under steady state excitation, the PL intensity is inversely proportional to the radiative recombination probability ($I \propto \tau_r^{-1}$) the commonly used expression for calculating the activation energy follows [171]

$$I = \frac{I_0}{1 + \sum_i A_i e^{-\frac{E_{\mathrm{act},i}}{k_B T}}}. \tag{5.2}$$

The number of exponential terms in the denominator depends on the number of non-radiative recombination channels present in the sample. Fig. 5.4(f) is an Arrhenius plot of the integrated PL intensity of the MQW emission peak measured at the highest excitation density. The intensity was fitted using Eq. (5.2) with two exponential terms, which yielded two activation energies (18 meV and 123 meV). This procedure was also carried out for the PL measurements of the remaining excitation densities and the activation energies are summarised in Tab. 5.1.

In general for QWs, the quenching of the luminescence is due to carriers being thermally excited into the barrier layer, where the activation energy is linked to the depth of the QW [172]. In the barrier they can recombine non-radiatively, which is referred to as a barrier to capture process [173]. However, even the highest activation energy of 123 meV is too small for carriers leaving the QW if a conduction/valance band offset of 70/30 [174] or 60/40 [175] is assumed. Therefore, the higher activation energy might be related to the activation of non-radiative channels due to defects, such as dislocations. With increasing laser power density the activation energy increases from around 50 meV to 123 meV, which could be due to saturation of non-radiative recombination centres [176].

At all three laser power densities, the lower activation energy is in the range of 10–20 meV and is not strongly affected by it. Thermally excited carriers are no longer bound by the potential fluctuations, caused by compositional and interface fluctuations, but are still confined within the QW [168]. Hence, the second activation energy is much lower than the QW depth and is related to the depth of these potential fluctuations. Since the lower activation energy is barely affected by an increase in laser power also suggests that this activation energy is associated with these potential fluctuations. Another possibility is that the

carriers are bound to a donor within the QW and the lower activation energy could also be associated with the binding energy needed to ionise this donor. The exciton binding energy with Si as the donor is 12–17 meV [177].

5.4 Investigation and classification of surface features

The planar InGaN/GaN MQW structures were investigated by scanning electron microscopy. Observed macroscopic features, such as V-defects and trench defects, on the surface are identified, classified and further investigated by CL hyperspectral imaging and transmission electron microscopy.

5.4.1 Surface morphology

The surface morphology of the InGaN/GaN MQW structures grown at the University of Sheffield was investigated by SEM. Figs. 5.5(a)–(e) show typical SE images of MQW structures with increasing emission wavelength from 407 nm to 503 nm. The surface appears to be smooth apart from two types of microscopic feature, namely V-pits and trenches.

The surface pits are hexagonal in shape in the *c*-plane as seen in the oblique view SE image in Fig. 5.5(f). This defect is very common in multilayer InGaN/GaN structures and is referred to as a V-pit or V-defect and usually caused by TDs [146, 178, 179]. The V-pits are inverted open hexagonal pyramids with six facets of $\{1\bar{1}01\}$ orientation. The main causes of the formation of the V-pit are not unambiguously known, but mostly likely are increased strain [180] and kinetic effects, i.e. a change of gallium incorporation and In segregation [179, 181]. The InN content is also reported to be an important factor; for low InN compositions there is almost always a TD originating at underlying interfaces or an inversion domain at the apex of the V-pit [179, 146, 181], whereas for high InN compositions (>30%) stacking mismatch boundaries (SMBs) can also drive the formation [182].

An estimate of the pit diameter is given in Tab. 5.2. The huge difference in size between the samples in Figs. 5.5(a), (b) and (d) and the sample in Fig. 5.5(c)

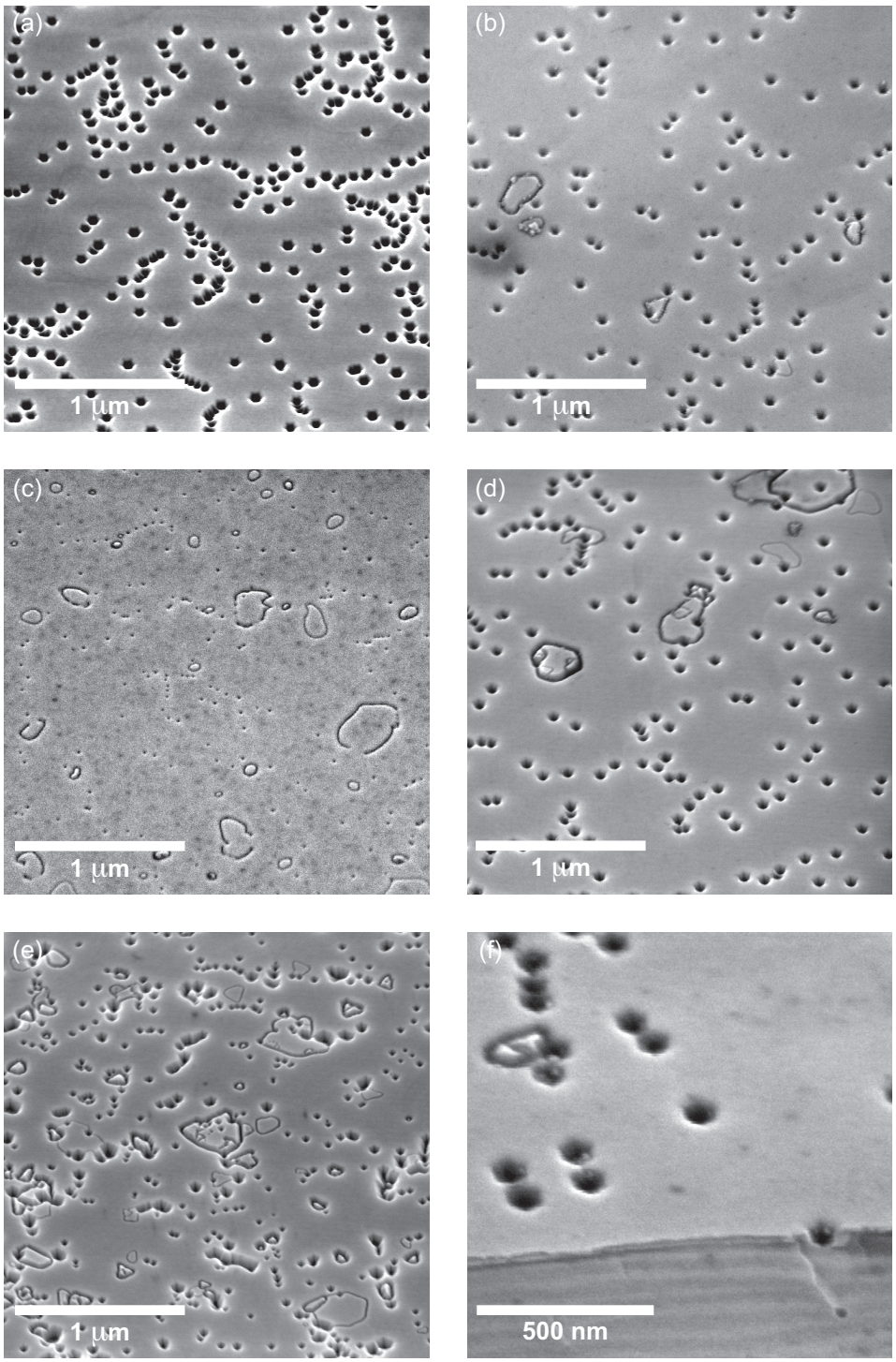

Figure 5.5: *(a)–(e) SE images of InGaN/GaN MQW structures from the University of Sheffield with increasing emission wavelength. (f) Oblique view SE images of a V-pit on the sample edge.*

Sample (from Fig. 5.5)	**No. of QWs**	**InN content** (%)	**Pit diameter** (nm)	**Pit density** (10^9 cm^{-2})
(a)	10	14	75	3.2
(b)	10	16	60	1.5
(c)	3		10–15	3.0
(d)	10	20	65	2.5
(e)	5	24	20–100	

Table 5.2: *Number of QW periods, InN content and estimation of V-pit diameter and density for MQW structures in Figs. 5.5(a)–(e).*

can be explained by the number of QWs. V-pits start to form at one of the first few InGaN–GaN interfaces and their lateral size therefore increases with each additional grown layer [146]. Empirical results also show that higher InN composition assist pit formation [179], which may be the reason for the large differences in pit size for the sample in Fig. 5.5(e), which possesses the highest InN content. Tab. 5.2 also shows the average V-pit density, which lies in the lower 10^9 cm^{-2} regime. This number corresponds to the minimum density of TDs in the samples, since not every TD opens up to form a V-pit.

Furthermore, the SE images in Fig. 5.5 reveal another type of macroscopic defect on the MQW surfaces besides the well-known V-pit. These features exhibit trench-like characteristics, which mostly form closed loops as seen in Figs. 5.5(b)–(d). The trenches are in general thinner than V-pits and sometimes intersect them. With increasing emission wavelength, and hence InN content, the surface becomes very rough with a high density of trenches and pits with varying diameter, as shown in Fig. 5.5(e) for the sample with the highest emission wavelength. The formation mechanism of the trenches is not clear and their optical characteristics compared with V-pits and defect-free regions on the surface are different as shown in the following section.

In Section 2.1 it was discussed that GaN has two possible polar surfaces due to the lack of inversion symmetry as illustrated in Fig. 2.3(b). It is possible for the area within the trenches to possess a different polarity. An area with different polarity is known as an *inversion domain*. A simple and fast method for determining the polarity is wet etching. The surface of GaN of [0001] polarity (Ga face) is inert when KOH is used as an etch solution, whereas the surface

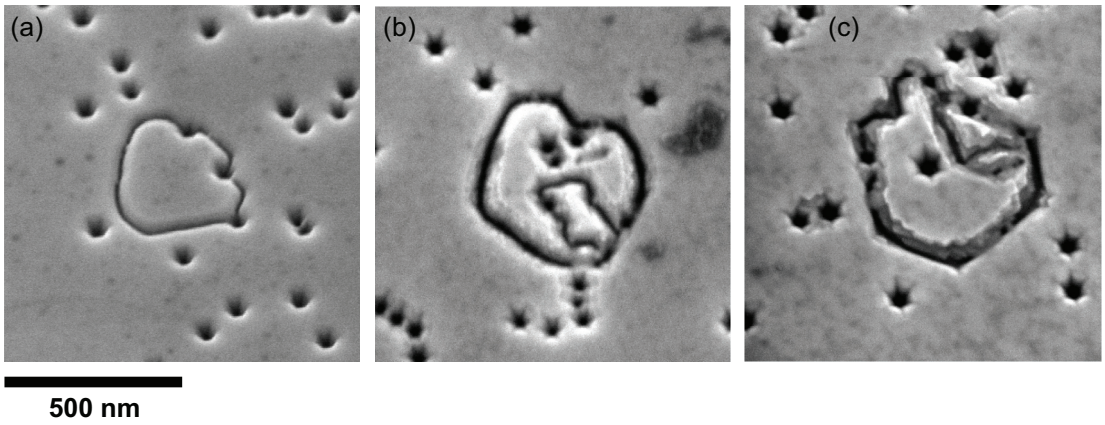

Figure 5.6: *(a) SE image of the surface of a as-grown InGaN/GaN MQW structure. SE image after etching in KOH at room temperature for (b) 5 minutes and (c) 35 minutes.*

of $[000\bar{1}]$ polarity (N face) is selectively etched [183]. Figs. 5.6(a)–(c) shows SE images of the surface of a InGaN/GaN MQW structure before and after etching in KOH solution for 5 and 35 minutes, respectively. Etching was performed at room temperature using a 1 M KOH solution. As can be seen in Figs. 5.6(b) and (c) the planar surface outside *and* inside the trench defect remains unchanged after exposure to KOH for 35 minutes. This illustrates that the entire surface exhibits [0001] polarity (Ga face). Only the edges of the trench defects and the V-pits are slightly affected by the KOH solution, which could be related to their different crystal orientation being more reactive to etching than the [0001] direction of the surface.

5.4.2 CL hyperspectral imaging

An advantage of CL hyperspectral imaging is the ability to map shifts in wavelength or energy, which can be traced back to features on the sample surface since an SE micrograph of the imaged area is recorded. Fig. 5.7 shows a set of CL maps of a relatively large area of a ten period MQW structure from the University of Sheffield containing three trench-like features and numerous V-pits. The luminescence is strongly influenced by the surface morphology. The peak energy inside the trench defect is redshifted by about 45 meV and the emission

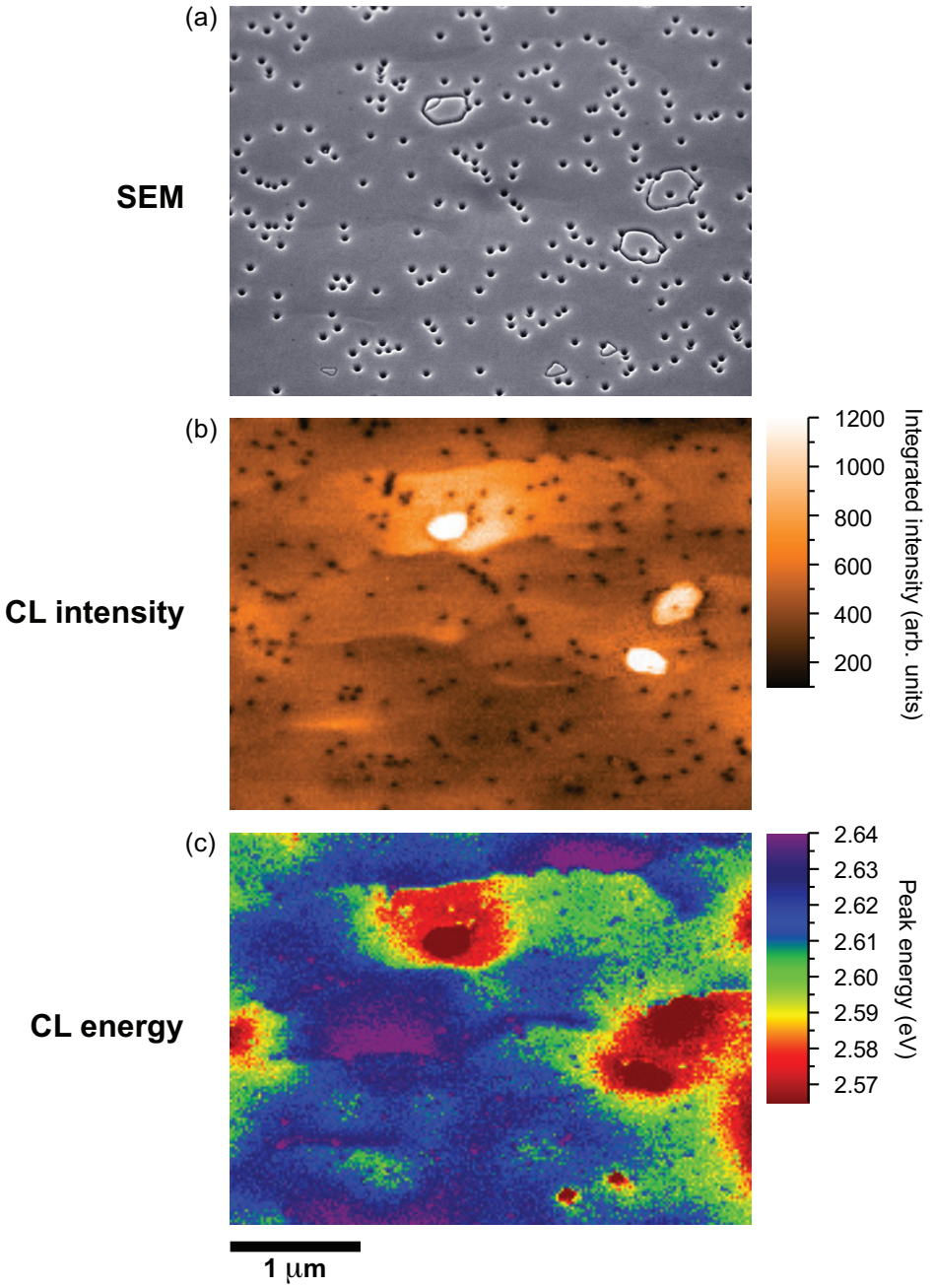

Figure 5.7: *CL hyperspectral information for a ten period InGaN/GaN MQW: (a) SE image, (b) fitted CL integrated intensity map and (c) fitted CL energy map at room temperature. From Ref. [113].*

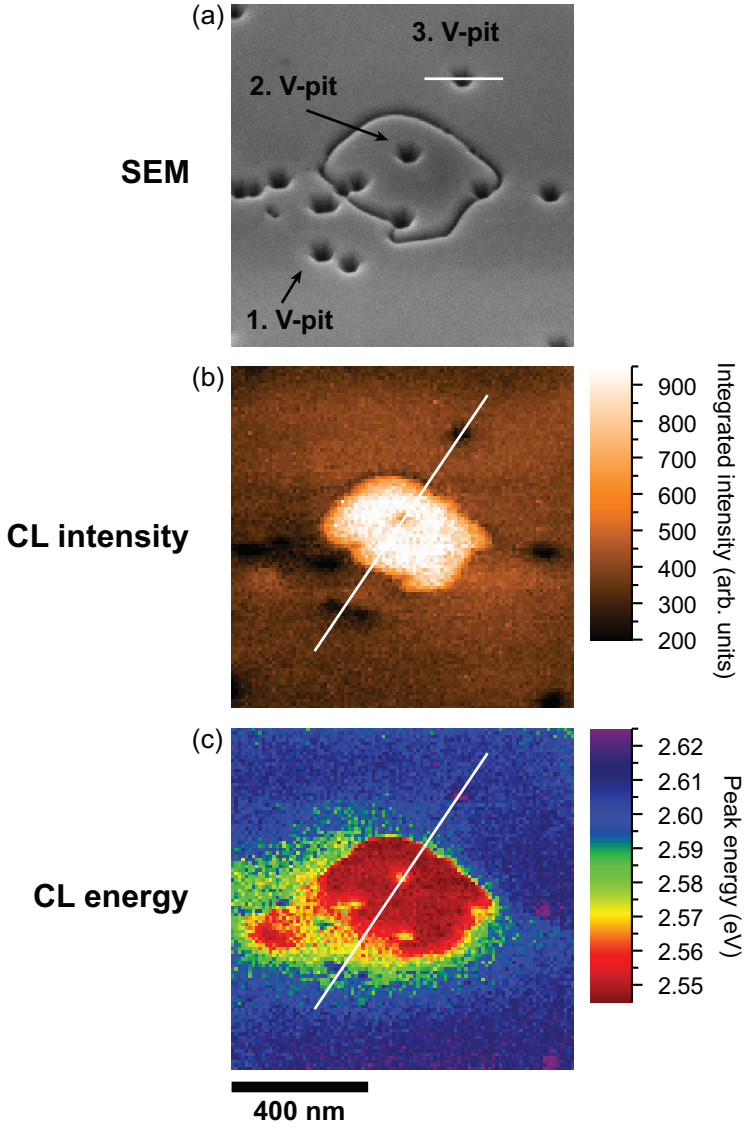

Figure 5.8: *High resolution CL hyperspectral images from sample in Fig. 5.7: (a) SE image, (b) fitted CL integrated intensity map and (c) fitted CL energy map at room temperature. From Ref. [113].*

is very intense in comparison with the surrounding planar regions. The V-pits show the opposite behaviour: the intensity is decreased and the emission energy is blueshifted, which is more clearly shown in Fig. 5.8(b) and discussed in the following paragraphs [113].

For a more detailed analysis, higher resolution hyperspectral images of the

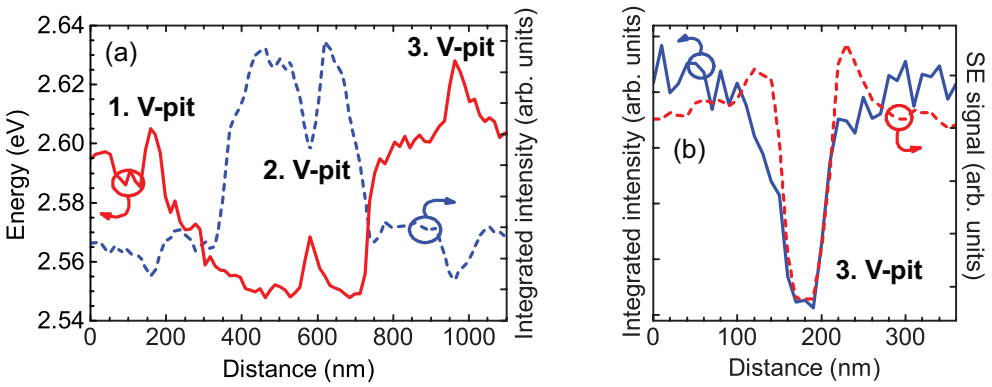

Figure 5.9: *(a) CL line scans through a trench-like feature and three V-pits and (b) horizontal line scans through the third V-pit. From Ref. [113].*

trench defects were recorded, one of which is shown in Fig. 5.8. The SE micrograph in Fig. 5.8(a) displays a trench-like feature of roughly 500 nm in diameter enclosing a few V-pits of about 65 nm in diameter. The MQW emission peak is fitted with a Gaussian function and the CL integrated intensity and energy maps for the fits are illustrated in Figs. 5.8(b) and (c), respectively. For another illustration of the luminescence behaviour of these features, providing information on a 10 nm length scale, line scans are taken across the trench-like feature and three V-pits (Fig. 5.9(a)). The line scans clearly demonstrate the opposite behaviour of the V-pits compared to the area inside the trench defects. In particular, the peak energy for the V-pit in the middle of the trench-like feature is shifted by about 10 meV in energy over a distance of less than 25 nm. Fig. 5.9(b) shows horizontal line scans of the SE signal and CL integrated intensity of the third V-pit as marked in Fig. 5.8(a). The similar shape of the two scans is notable and the CL feature is broadened by no more than 10 nm compared to the SE scan.

The increase in emission energy from the V-pits can be caused by different effects, including decreased InN content, reduction in well width, increase in compressive strain and reduction of the QCSE. The above effects, however, are usually interrelated. For example, decreased InN content or narrower well widths reduce the influence of the QCSE, reinforcing the blueshift. The increased energy emission from the V-pits is most likely due to a reduced InN incorporation into the InGaN MQWs along the sidewall of the pits, which is supported by results from InGaN single QW samples in Ref. [184]. However, in Ref. [179] it is also

reported that the different crystal orientation of the sidewalls compared to the [0001] direction leads to an increased InN incorporation into the MQWs and an emission at lower energies was observed in contrast to the blueshift in Fig. 5.8(c). It should be mentioned that the V-pits in both references are twice as large as the pits described here. It is difficult to determine which of the aforesaid mechanisms is the dominant one. However, it is clearly evident that V-pits are associated with non-radiative recombination centres since their luminescence intensity is greatly reduced.

The formation mechanism of the trenches is not clear. Due to their increased CL intensity, the trench defects seem to localise the radiative carrier recombination while redshifting the emission energy, which suggests an InN rich region or wider wells inside the trench enclosed region. Refs. [150, 149] describe an increased and redshifted CL emission coming from inclusions of increased height embedded in V-defects, which seem to be similar to the trench-like features in Fig. 5.8. They concluded that the bright emitting inclusions nucleate at the highly strained InGaN–GaN interface and attributed them to an increased InN content, where the V-defect induces InN segregation during the subsequent barrier and well growth. Similar features were also observed in Ref. [151], where it was also reported that a GaN barrier growth at higher temperatures than the InGaN wells results in inclusion-free surfaces. A cause for the increased CL intensity inside the trench defect could be carrier localisation in quantum-dot-like structures of almost pure InN in the InGaN layer [185], which would also explain the redshifted emission as observed in Fig. 5.8(c). Furthermore, a difference in strain caused by the trench-like feature could assist InN migration and formation of these quantum dot (QD) structures within the trenches [141].

These issues will be discussed further after considering some similarities and some differences in similar trench-like features on the surface of InGaN/GaN MQW structures grown at the University of Cambridge.

Investigation of the surface morphology of similar MQW structures from the University of Cambridge revealed trench defects of various trench widths and shapes compared with observations of samples from the University of Sheffield. Again, SE imaging showed the presence of a high density of trench defects besides the commonly occurring V-defect. A closer look shows differences in the appear-

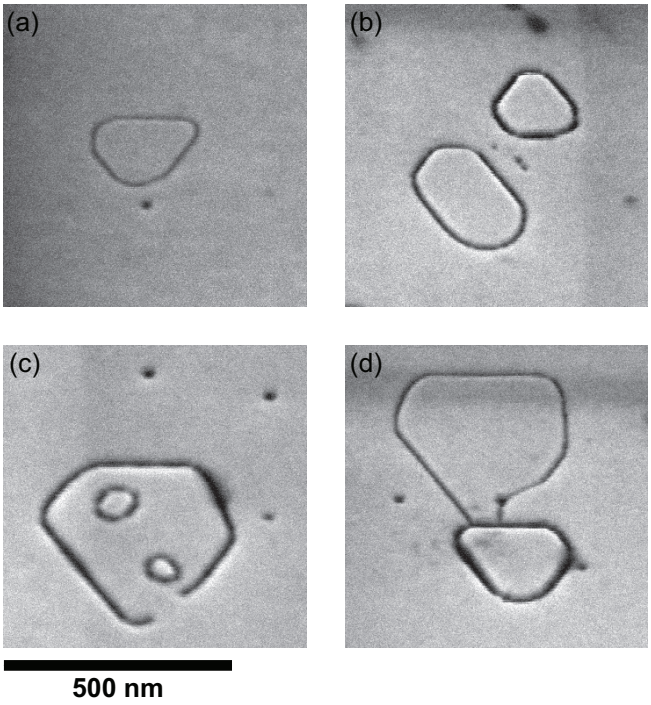

Figure 5.10: *SE images of three different types of trench defects on the surface of a five period InGaN/GaN MQW structure from the University of Cambridge: (a) narrow trench forming a closed loop, (b) two wide trenches forming a closed loop, (c) open loop and (d) a narrow trench loop connecting a wide trench loop. The pits are V-defects.*

ance of such defects, which have diameters of a few 100 nm. Three types of trench defects can be identified and classified as seen in Figs. 5.10(a)–(c): (i) *narrow* trenches forming closed loops, (ii) *wide* trenches forming closed loops and (iii) trenches forming *open* loops. These three types sometimes connect with—or intersect—either trenches of another kind (Fig. 5.10(d)) or V-defects. The total trench defect density for the five period InGaN/GaN MQW structure is approximately 1×10^8 cm^{-2}.

The luminescence behaviour of these defects is notably different from the observations on comparable structures from the University of Sheffield [113], as discussed above. In those samples, CL hyperspectral imaging only revealed a redshift and strong intensity increase in the luminescence from within the trench loops in comparison with the surrounding area; no trench defects with varying trench

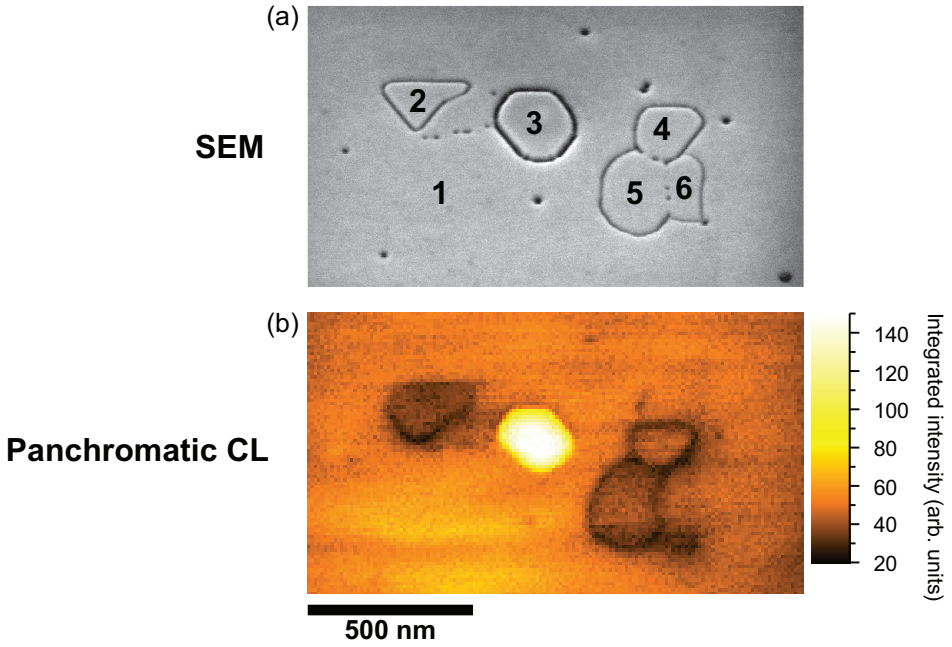

Figure 5.11: *(a) SE image of three trench defects neighbouring each other and (b) panchromatic CL image of the same area as seen in the SE image.*

width were observed. In contrast, the current sample from the University of Cambridge is governed by trench defects of more diverse types, each having a different impact on the luminescence. Fig. 5.11(a) shows an SE image of three neighbouring trench defects, namely (from left to right): a narrow trench loop; a wide trench loop; and interconnected narrow trench loops with an open loop. From a CL hyperspectral data set of this area a conventional panchromatic (i.e. spectrally integrated) CL intensity image was created, which is shown in Fig. 5.11(b). Three distinct luminescence behaviours are observed in this intensity map. The area inside the middle defect, a wide trench loop labelled '3', exhibits a much stronger CL intensity than the regions enclosed by adjacent loops or surrounding area. These structures therefore match the observations of the trench-like feature on the Sheffield samples [113]. In contrast, the Cambridge samples also show narrower trench loops (labelled '2', '4', and '5'), which show a reduced intensity compared with the above described trench enclosed regions. Furthermore, there are some regions within narrow trench loops, such as 6, which display no CL intensity contrast at all. Additionally, well-known V-pits are observed, which act

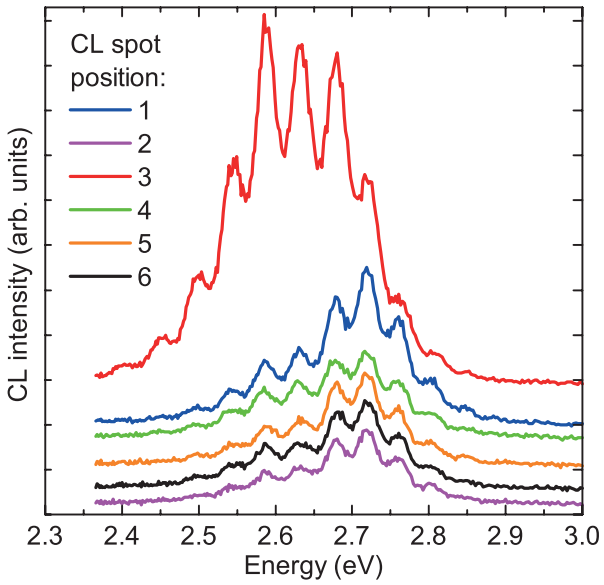

Figure 5.12: *CL spot spectra from six marked spots of a 5-by-5 pixel area in the SE image in Fig. 5.11(a). The spectra are offset for clarity.*

as centres for non-radiative recombination and therefore appear as dark spots in the CL intensity map. To further clarify this varying emission within the trench defects, mean spectra for 5-by-5 pixel areas at six different positions, marked by numbers on the SE image in Fig. 5.11(a), have been calculated; these spectra are plotted in Fig. 5.12. The CL spectra are dominated by thickness fringes resulting from interference between the directly emitted light and that reflected from the GaN–sapphire interface, which are observed due to the small numerical aperture of the reflecting objective. Region 3 shows not only a clear increase in intensity but also a redshift in its emission wavelength in comparison with the other trench defects and the surrounding (defect-free) area. Measurements on the other four positions inside the left and right trench defects show only a slight intensity reduction and small peak energy shifts compared with the defect-free area.

Exploiting the hyperspectral nature of the CL dataset, the MQW emission peak in each spectrum was fitted with a Gaussian function. The resulting maps of the fitted integrated intensity and peak energy are displayed in Figs. 5.13(a) and (b), respectively. The CL intensity map from peak fitting is almost identical to the panchromatic CL image in Fig. 5.11(b). The CL peak energy map (Fig. 5.13(b)) clarifies the mean energy shifts. The area within the middle trench defect (region

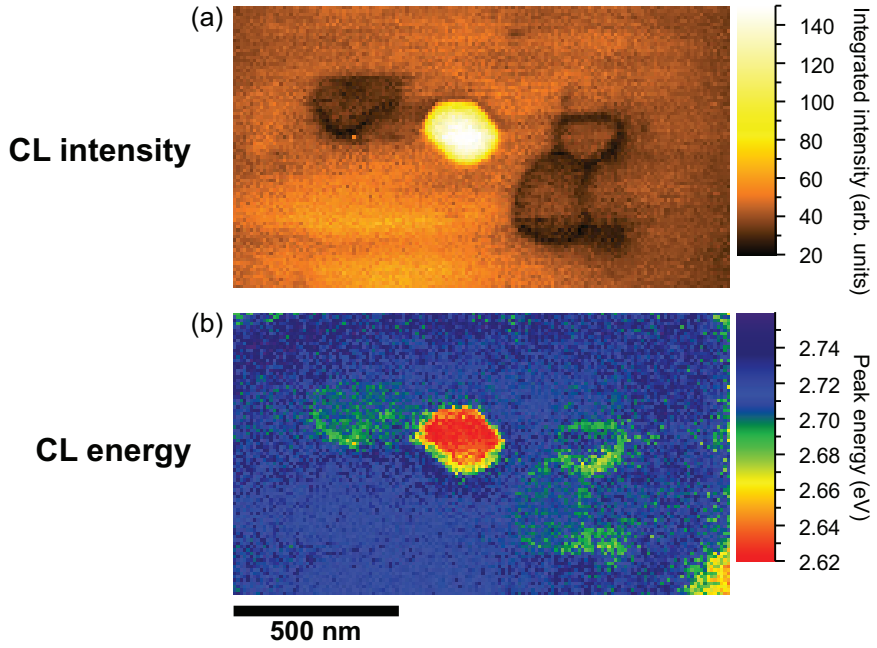

Figure 5.13: *Room temperature CL maps gained by fitting the MQW emission peak in the hyperspectral data set with a Gaussian function: (a) integrated intensity and (b) peak energy map.*

3) is redshifted by about 90 meV compared with the defect-free surrounding region, while its intensity changes by almost an order of magnitude. On the other hand, the enclosed regions of the narrower trench defects (regions 2, 4, and 5) only show a small redshift of about 10 meV and a slight reduction of the intensity. As already seen in the panchromatic CL image, the area where loop 6 is located shows no change in the CL intensity map. Also, no energy shift is observed for region 6, whose presence appears to have no impact on the luminescence. Fig. 5.14 shows the energy shift plotted against the width of the trenches, showing a generally increasing redshift with increasing trench width. The width was estimated from intensity line scans across the SE images.

To investigate the underlying structural characteristics of the trench defects cross-section TEM measurements (*FEI Tecnai F20*) have been performed at the University of Cambridge on a ten period QW sample. This sample is in all other ways identical to the five period QW sample investigated by CL imaging [152]. A high angle annular dark field (HAADF) image of a sectioned trench

t]

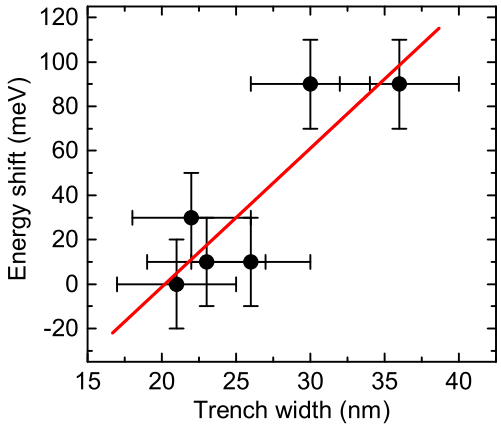

Figure 5.14: *Energy shift of the inside region with respect to the surrounding area against trench width, fitted with a straight line as a guide for the eye.*

defect is shown in Fig. 5.15, with the QWs appearing as bright line contrast. The defect bounded by two sectioned regions of the trench, indicated by white arrows, encloses a raised central area. The shadow image of a second trench very close to the first is visible due to the projection of the sectioned trench through the entire thickness of the TEM specimen. This shadow image confirms that the trenches are not V-defects, as these are pyramidal features which do not produce a shadow V-shape when viewed in cross-section. HAADF imaging of the defect-free area shows that the QWs and barriers are highly uniform with thicknesses of (2.5 ± 0.3) nm and (7.5 ± 0.3) nm respectively. The QWs within the enclosed region of the trench defect, however, are wider, with an average thickness of (3.5 ± 0.3) nm, leading to the area being raised compared with the surrounding region.

The authors of Ref. [153] have performed further high resolution cross-section TEM investigations on these structures. It was found that a basal plane stacking fault (BSF) extends underneath the trench defect and ends below the apices of the V-shaped trenches. From there a stacking mismatch boundary (SMB) runs upwards from the edge of the BSF and terminates at the apex of the trench. The stacking order is altered to ...ABABCBCBC... causing the appearance of the BSF. Plan-view TEM showed that straight boundaries of the defect are orientated

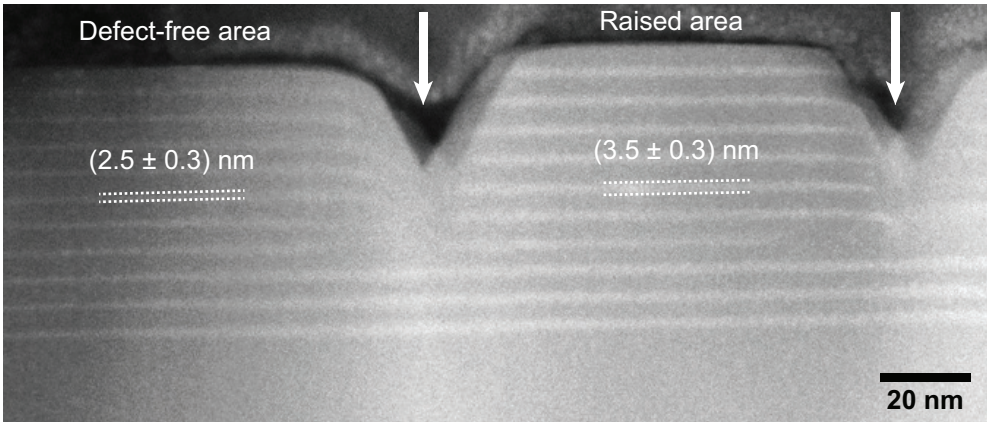

Figure 5.15: *HAADF image of a sectioned raised trench defect, with trenches indicated by arrows. The thickness of the InGaN QWs is indicated by dotted lines. TEM measurements were carried out at the University of Cambridge.*

at 60° or 120° to each other and follow $\langle 1\bar{1}00 \rangle$ directions. It is proposed that whenever a change in orientation occurs the SMB opens up into a pit. Jagged sections appear where the boundary undergoes frequent changes in direction to maintain the $\langle 1\bar{1}00 \rangle$ orientation of the SMB and the generated pits join to form a trench.

Ting et al. have used the AFM to study the surface morphology of what they called inclusions, described as larger filled-in V-pits, similar in appearance to the trench defect [149]. They reported that some of these features have an increased height of up to 12 nm. Florescu et al. described these inclusions appearing as variously bright and dark in panchromatic CL images [150]. Both Florescu and Ting suggested that the brighter inclusions originate at the first InGaN–GaN interface, where the growth mode changes from three-dimensional island-like to two-dimensional step-flow growth. They suggest that inclusions of segregated indium or InN-rich InGaN are nucleated at those positions where TDs or V-pits intersect the InGaN–GaN interface. Further investigation by Kumar et al. showed that the use of trimethylindium pre-flow before the InGaN well and high temperatures for the GaN barrier growth encouraged appearance of the inclusions [186]. The additional In atoms might nucleate at V-pits and form InN-rich clusters at the GaN interface, which act as sinks for further In segregation causing the inclusions to appear during the subsequent layer growth. The appear-

ance of inclusions can be reduced or prevented by using elevated temperatures or introducing hydrogen during the GaN barrier growth, or by reducing the InGaN growth rate [149, 150, 187].

The results of Fig. 5.13 illustrate that trench defects of different types cause marked changes to the luminescence behaviour of the QWs. There are several possible causes for the changes in energy and intensity: (i) change in the well width; (ii) change in the InGaN composition; (iii) change in the strain state; and (iv) change in the strength of the QCSE, several of which are interrelated. Possible causes of a redshift will now be considered, along with the impact on luminescence intensity. One is an increase in the well width of the QWs. Wider QWs, however, lead to a decrease in intensity, because the QCSE increases due to stronger spatial separation of electron and hole wave functions. A stronger QCSE additionally redshifts the emission. Another possibility for a redshift is an increase in the InN content, which also reduces the emission intensity due to the degradation of crystal quality. Strain relaxation has an influence on several parameters. The MQW structures are usually under compressive strain due to the pseudomorphic growth. Partial relaxation of this strain causes the emission to shift to lower energies. Since strain leads to the QCSE, its reduction also results in a blueshift and increase in intensity. Strain relaxation can also cause an increase in the InN fraction through the compositional pulling effect. This has been observed in InGaN epilayers with increasing film thickness as strain relaxation starts to occur, which leads to a higher InN incorporation towards the top of the epilayer [188, 189, 190]; similar results have been found for InGaN MQWs [191]. A significant enhancement of the emission intensity can be due to a localisation effect in the MQW region. It can be caused by potential fluctuations, such as local changes of the InN composition or well/barrier widths. An increased InN content can be related to InN-rich clusters or quantum-dot-like states within the well layer, which would also explain the strong redshift in the emission energy [185]. This makes localisation the strongest contender to explain a redshift accompanied by an increased emission intensity (as in region 3) since most of the single effects causing an increased intensity lead to a blueshift of the emission, as described above. A combination of the above-mentioned effects, however, could lead to a redshift and significantly increased intensity, such as strain relaxation enhancing InN incorporation and leading to carrier localisation. The redshift due to the

InN increase and localisation, however, must dominate over the blueshift from a reduced QCSE caused by relaxation in this case.

The observed, significant variations in luminescence between the trench defects with different trench widths might be caused by different material properties within the loops, and the effect of these properties on the QWs. Considering the greater trench width of some of the loops, it is a fair assumption that with increasing width the V-shaped trenches penetrate further into the MQW structure, maybe even as far as the first QW interface. Also, the TEM findings that a vertical SMB is connected to the apex of the trench linked to a BSF extending below the loop, suggests that the affected area of the defect is separated from the surrounding material and the undisturbed QWs below the BSF. This separation could lead to altered growth conditions in the affected area causing a change in the material properties. Therefore, loops with narrower trenches might be less affected since a smaller area is altered compared with wider trenches, which penetrate further into the material.

As the HAADF image in Fig. 5.15 shows, some defects possess QWs with increased thickness within the enclosed area leading to that area being raised compared with the surrounding region. Wider QWs decrease the emission energy due to weaker quantum confinement and stronger QCSE. From the HAADF image the width of the trench is estimated to be 26–28 nm, which identifies the defect as one with narrow trenches according to the introduced classification. Furthermore, AFM imaging on these structures showed that trench defects can have lowered, level or raised central regions [152]. An increase in well thickness, however, would not explain the drastic increase in intensity for the loops with wider trenches or the appearance of trench defects with level or lowered central regions since there is no additional material within the enclosed area. An alternative explanation is necessary. The observed formation of stacking faults and the generation of a V-pit by SMBs as reported in Ref. [153] is one route to strain relaxation [144, 192]. As noted above, strain relaxation could lead to an increase in the InN content (compositional pulling effect), which could cause carrier localisation and a redshift of the emission if it dominates over a blueshift from a reduced QCSE. Localisation and reduction of the QCSE (due to strain relaxation) increases the emission intensity. The impact of the trench defect on the emission properties cannot be explained by one single mechanism since most of the effects are interrelated. For

narrower trenches the wider QWs might be the cause since less material is affected and only a slight reduction in intensity is observed. For wider trenches on the other hand localisation might dominate due to the large increase in intensity and redshift.

The trenches themselves appear as dark lines in the CL intensity maps in Figs. 5.11(b) and 5.13(a). TDs generating V-pits are considered to be centres for non-radiative recombination; since TEM measurements showed the trenches consist of coalesced pits, which are caused by SMBs opening up, it is reasonable to assume that SMBs themselves also act as non-radiative recombination centres.

5.5 Summary

Planar InGaN/GaN MQW structures have been studied by SEM and PL and CL spectroscopy.

PL measurements on these structures were carried out between 16 K and room temperature using three excitation power densities. A shift of the MQW emission peak towards lower energies was observed with increasing InN content and well width. Temperature-dependent PL showed an s-shaped dependence of the emission energy consistent with the presence of potential fluctuations (InN content and interface). The almost vanishing IQE at low excitation power showed that at room temperature non-radiative recombination dominates, whereas for high excitation power radiative recombination paths still compete at room temperature. Two thermally activated recombination channels are present; the first is related to carriers overcoming potential fluctuations within the well, whereas the second might be related to defects, such as dislocations.

Three types of trench-like features or trench defects have been identified in InGaN/GaN MQW samples and classified using scanning electron microscopy. Loops with narrow trenches, loops with wide trenches and open loops. CL hyperspectral imaging showed marked difference in luminescence from within the trench enclosed regions. While the area inside wider trench defects gives luminescence which is redshifted and more intense, the emission from inside loops with narrower trenches is only slightly redshifted and its intensity is lower compared with the surrounding region. TEM measurements showed an increase in QW thickness for the enclosed area. Different effects and their combination, such as

wider QWs, increased InN composition, strain relaxation (formation of SMBs and BSFs) and carrier localisation (potential fluctuations or InN rich clusters), could be the cause for the observed luminescence changes. With increasing depth and width of the trenches more enclosed material is affected by the defect, effectively separating the inside region from its surroundings. For wider trench defects carrier localisation could be the main cause, dominating over other effects, whereas for narrower trench defects localisations seems to be weaker and the increased width of the QWs governs the emission properties. Furthermore, SMBs opening up to pits might act as centres for non-radiative recombination similar to TDs generating V-pits, because of their dark appearance in CL intensity images.

CL investigation of V-defects showed a decrease of the emission energy indicating a reduced InN incorporation into the sidewalls and a reduction of luminescence intensity, which suggests that they act as non-radiative recombination centres.

Deeper understanding of these defects and of their different emission characteristics compared with the rest of the sample surface—some acting as non-radiative recombination centres—is important for further enhancement and development of ultra-efficient LEDs based on InGaN/GaN structures.

Chapter 6

Luminescence investigations of GaN nanorods containing multiple InGaN/GaN disks

6.1 Introduction

LEDs using InGaN/GaN MQWs as their active region already exhibit excellent optical properties and are commercially available. The overall efficiencies of the devices, however, still need to be improved and the fabrication costs lowered to enhance the large-scale commercialisation of SSL.

Spontaneous and strain-induced piezoelectric polarisation along the c direction, as discussed in Section 2.3, induce strong internal electric fields in the same direction [52]. This leads to the phenomenon referred to as QCSE, which red-shifts and decreases the intensity of the MQW emission peak [56]. Furthermore, the light extraction efficiency from the active region of the material is reduced by total internal reflection at the semiconductor–air interface [193].

Two approaches exist to reduce or eliminate the QCSE within nitride structures. The highest spontaneous and piezoelectric polarisation exists along the (0001) or c direction. By moving towards the m-plane or a-plane, whose directions are perpendicular to the c direction, it is possible to eliminate both types of polarisation [194, 195]. These planes are referred to as non-polar; planes in between are called semi-polar. The use of semi-/non-polar planes offers one route

to reducing or even eliminating the influence of the QCSE [196, 197]. Growth along these planes, however, is difficult and can result in poor crystal quality due to a high density of dislocations and stacking faults [198, 199]. The second approach to reduce the QCSE employs nanostructures, such as nanorods or nanowires, which incorporate MQWs either as disks along the c direction or on the sidewalls (core–shell nanorods). The MQW structure of hexagonally-shaped core–shell nanorods is located on their sidewalls, which are non-polar planes with absent polarisation fields [200]. Enhanced performance due to additional quantum confinement and a reduction in the QCSE due to strain relaxation within the MQW structure have been reported for nanorods with InGaN/GaN MQW disks in the c-plane [201, 202, 203]. It is possible to grow GaN nanowires by MOCVD in which TDs have been eliminated [204]. Additionally, nanostructures have the advantage of improved light extraction due to an increased surface area, which further enhances the device efficiency [205, 206]. Detailed investigation of the processes controlling the light emission from nanorods is still required to further understand the impact of strain and carrier transport within them.

This chapter discusses the optical behaviour of individual, isolated GaN nanorods containing InGaN/GaN MQWs using CL hyperspectral imaging, and of nanorod arrays using PL spectroscopy. In contrast to other studies, the combination of high spatial and spectral resolution provided by the CL technique makes it possible to obtain useful information from a single isolated nanostructure on a length scale approaching 10 nm [109, 113]. *Conventional* CL imaging records either the total spectrally-integrated intensity (panchromatic) or the intensity distribution at a fixed wavelength (monochromatic). By contrast, CL *hyperspectral imaging* is a more powerful technique in which an entire luminescence spectrum is recorded at each pixel in an image, as described in Section 3.4.

Conventional CL mapping has been used for various kinds of nanorod structures fabricated from the group III-nitride system, e.g. GaN nanorods of various diameters, InGaN/GaN pedestal nanorods, core-shell InGaN/GaN nanorods or GaN nanorods containing an InGaN SQW [201, 207, 208, 209]. There have also been a few reports of in-depth spot-mode CL investigations of ZnO nanorods [210, 211]. None have combined the nanoscale spatial resolution with the spectral resolution achieved in the present study.

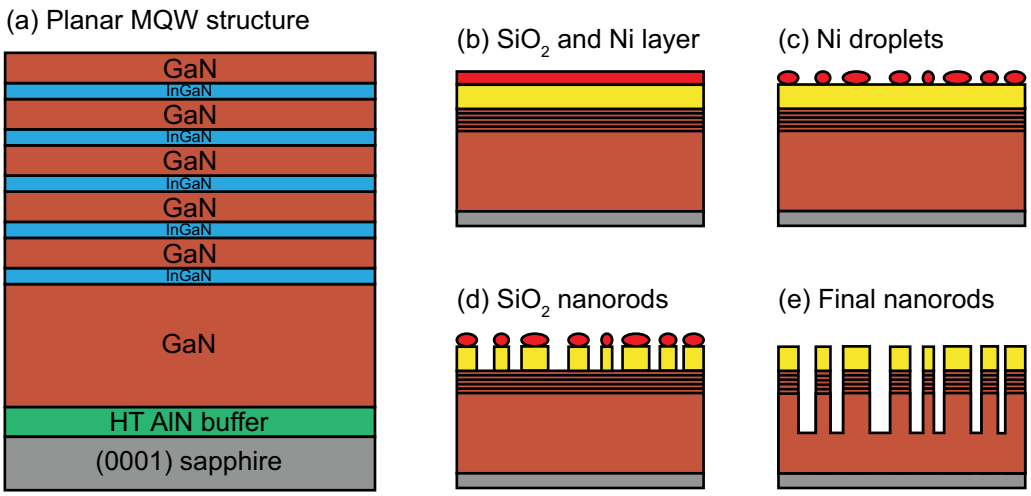

Figure 6.1: *(a) Structure of a five period InGaN/GaN MQW sample from the University of Sheffield. Fabrication of the nanorods using a self-assembled nanomask: (b) Deposition of a SiO_2 and nickel film, (c) annealing step to form nickel droplets, (d) etching of SiO_2 nanorods and (e) ICP etch of GaN forming the final nanorod structure.*

6.2 Nanorod fabrication

The nanorods in this study were fabricated from planar InGaN/GaN MQW samples using a top-down approach. The MOCVD growth of the planar structures, as described in Section 5.2, and the fabrication of the nanorods were performed at the University of Sheffield in the group led by Prof. Tao Wang. The planar structure chosen for the nanorod fabrication process consisted of a five period InGaN/GaN MQW structure with 3 nm thick InGaN wells, 10 nm thick GaN barriers and a GaN capping layer of nominal thickness of 45 nm. This planar structure will be referred to as the as-grown sample.

The fabrication of the nanorods employs self-assembled nickel droplets as an etch mask, which eliminates a photolithography step [212, 213]. This process is schematically outlined in Fig. 6.1. First, a 200 nm thick SiO_2 film was deposited on the surface of the planar MQW samples using plasma-enhanced chemical vapour deposition. In the next step, thermal evaporation was used to grow a nickel film of about 10 nm. To form the etching mask the structure was annealed under a flowing N_2 atmosphere at 800–850 °C, which allows the nickel layer to

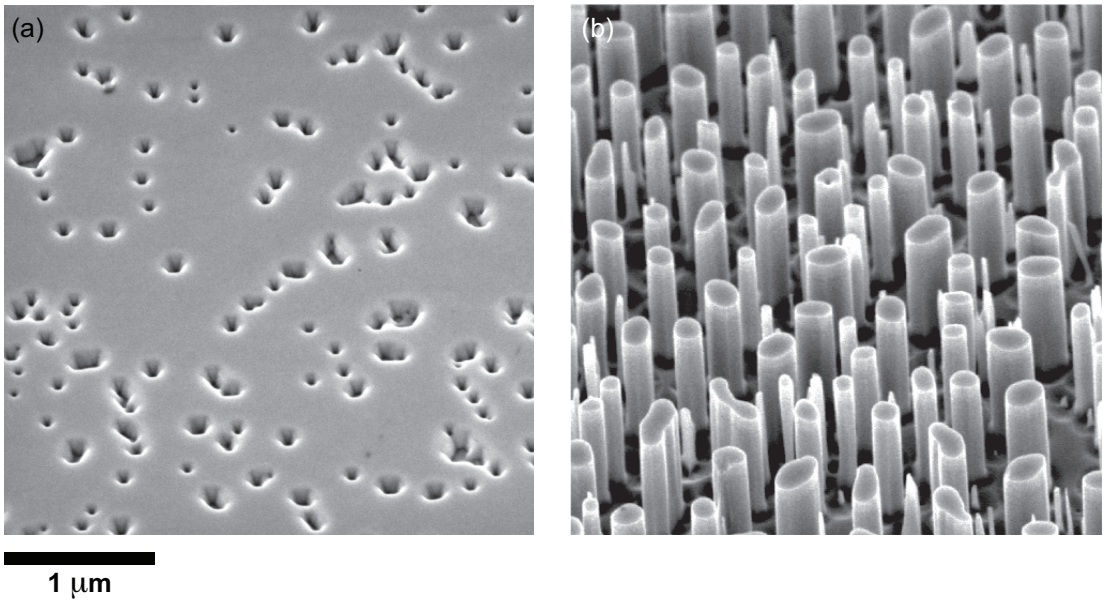

Figure 6.2: *(a) Typical SE of the surface of the InGaN/GaN MQW structure. (b) SE image of the nanorod array after the etch process, showing nanorods with diameters in the range of 100–300 nm. The sample is tilted by 45° in respect to the electron beam for both SE images.*

transform into self-organised islands. These islands have diameters up to a few 100 nm. Afterwards a standard reactive ion etching process is carried out to create SiO_2 nanorods, which serve as a second etch mask. A second dry etching step using an inductively coupled plasma (ICP) is used to etch the MQW structure until parts of the GaN template are exposed. ICP etching normally damages the structure, especially the newly created sidewalls of the nanorods, which leads to a significant degradation of the electrical and optical performance of the device [214, 215, 216]. A surface treatment is therefore applied to the nanorods to remove any damage due to etching.

6.3 Surface morphology

The surface morphology before and after the nanorod fabrication process is investigated by SEM. A typical SE image of the surface of the planar InGaN/GaN MQW sample is shown in Fig. 6.2(a). The surface exhibits a high density of pits

of varying diameters. The pits, commonly referred to as V-defect, are hexagonal in shape and were discussed in Section 5.4.1; their luminescence behaviour was studied in Section 5.4.2. This sample was used to fabricate nanorods using the top-down approach as described in the previous Section 6.2 using a self-assembled nickel mask. Fig.6.2(b) displays a SE micrograph of the resulting nanorod array; the sample is tilted by 45° in respect to the electron beam. The nanorods have diameters ranging from 100 nm to 300 nm, an average length of 900 nm and the nanorod density is in the mid 10^8 cm^{-2} regime. Compared to the as-grown sample, the top surface of the nanorods is flat with almost no presence of V-pits. The SE image in Fig. 6.2(b) shows only one nanorod with a pit. The non-uniformity is due to the randomness of the formation of the nickel droplets, which act as an etch mask. Better control of the mask formation, such as thickness of the nickel film, annealing temperature and duration of the annealing step should lead to a higher uniformity of nickel droplets with similar diameters [217, 218].

6.4 CL hyperspectral imaging of single nanorods

For the optical investigation of an individual, isolated nanorod, the nanorods were detached from the original array and dispersed in a suspension of acetone. This suspension was then deposited on a clean piece of silicon wafer and left to evaporate. SE imaging was performed on this sample to locate isolated nanorods for subsequent recording of CL hyperspectral images. A typical SE micrograph after isolation of a nanorod with 250 nm in diameter is shown in Fig. 6.3(a). The left-hand side corresponds to the top of the nanorod.

A room temperature CL hyperspectral image of this nanorod in Fig. 6.3(a) was recorded using an acceleration voltage of 5 kV, a beam current of about 6 nA, a step size of 20 nm and an exposure time of 20 ms per spectrum. The measurement geometry is schematically shown in Fig. 3.10 in Section 3.3.2. Fig. 6.3(b) displays the integrated CL intensity map. This map is equivalent to a conventionally acquired panchromatic CL image and clearly shows a region of higher intensity at the top (left-hand side) of the nanorods, corresponding to the location of the QW stack. Fig. 6.3(c) shows representative CL spectra from the hyperspectral

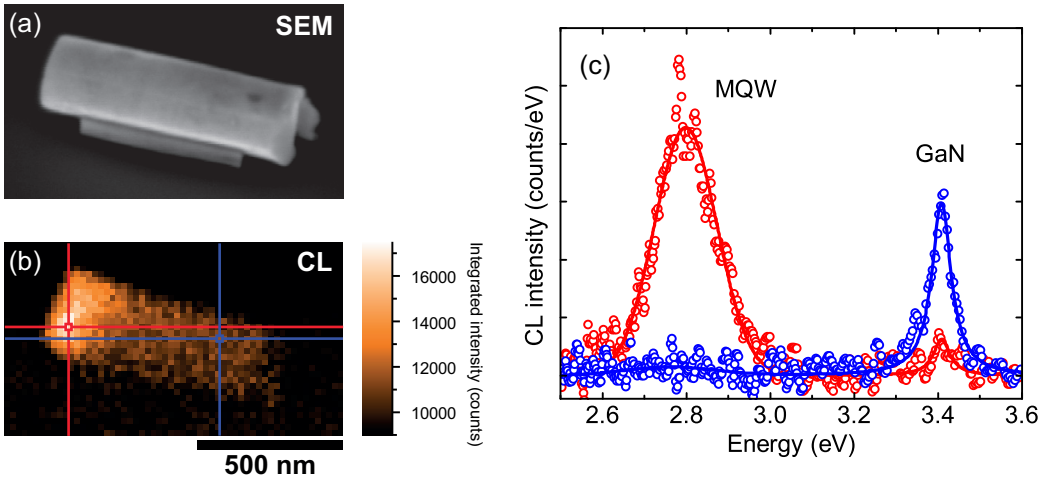

Figure 6.3: *(a) SE electron image of an isolated nanorod with a 250 nm diameter on a silicon substrate. (b) Corresponding room temperature panchromatic CL map showing the total integrated CL intensity. (c) Representative CL spectra with fits of the MQW and GaN emission taken from two pixels of the hyperspectral image indicated by the two crosshairs in (b).*

CL image, with one from a pixel within the area with high intensity (i.e. MQW emission) and the second from further down the rod (showing GaN emission). Similar observations of a single QW nanorod have been reported at lower spatial resolution using μ-photoluminescence [219].

Each spectrum in the hyperspectral image consists of a peak originating from the GaN band edge emission, near 3.41 eV, and one from the MQW emission, near 2.8 eV. For a more detailed analysis of the hyperspectral image, these peaks in each spectrum were numerically fitted using Voigt and Gaussian functions for the GaN and MQW peaks, respectively. The resulting CL energy and intensity maps of the GaN and MQW emission are reproduced in Figs. 6.4(a)–(d). To aid visualisation the corresponding CL intensity maps were used as a mask to display only the area in the CL energy maps where the intensity exceeds the noise level.

The map of the GaN emission energy in Fig. 6.4(a) reveals a negligible energy shift along the axis of the nanorod, indicating that there is no variation in strain within the GaN region of the nanorod. The room temperature transition energy of the free A exciton in single-crystal GaN films occurs at 3.42 eV, which is close to the measured GaN band edge emission of 3.41 eV in the CL map [130]. The

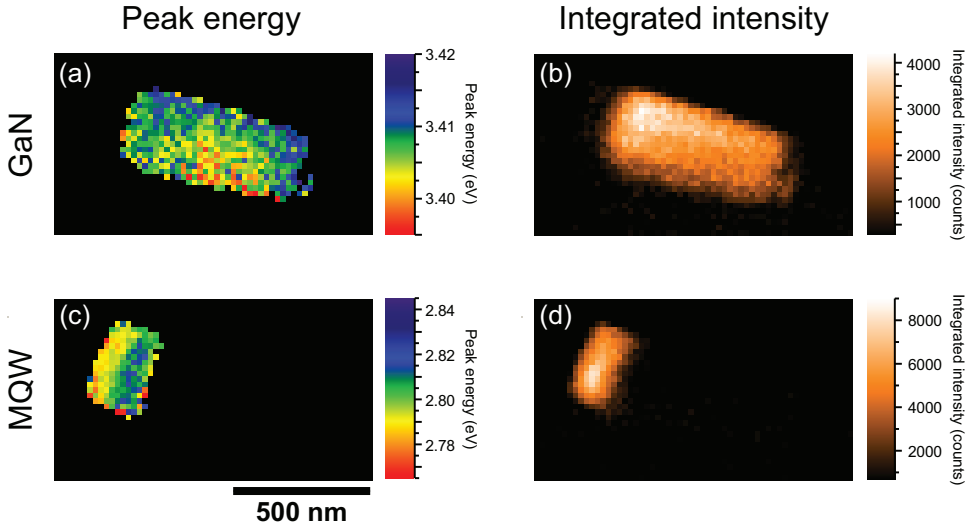

Figure 6.4: *Room temperature CL maps gained by fitting the hyperspectral data set in Fig. 6.3(b) with Voigt and Gaussian functions for the GaN and MQW emission peaks, respectively: (a) peak energy and (b) integrated intensity maps of the GaN band edge emission and (c) peak energy and (d) integrated intensity maps of the MQW emission. Using the spectral information gained by peak fitting it is possible to identify the spatial origin of the two peaks and map shifts in their energy. The MQW emission is located on the left-hand side corresponding to the top of the nanorod, whereas the GaN emission originates from the area below this region. The map of the GaN peak shows a negligible energy shift along the nanorod axis suggesting no variation in strain. However, the map of the MQW emission displays a small redshift towards the top surface of the nanorod.*

emission at the lower side of the nanorods is slightly redshifted, which is likely to be a result of self-absorption. The excitation and measurement geometry becomes very important in the case of three-dimensional structures. The nanorod in Fig. 6.3(a) lies horizontally on the 45° tilted sample holder; when the electron beam excites the "uphill" side of the nanorod (corresponding to the lower side in the SE and CL images) the emitted light has to pass through the rod before reaching the detection optics as seen in the sketch in Fig. 6.5(a). Stronger absorption of the emitted light by the GaN can therefore result in a small apparent narrowing and redshift.

The map of the MQW peak energy in Fig. 6.4(c) shows that there is no energy shift perpendicular to the axis of the nanorod, whereas a small redshift occurs

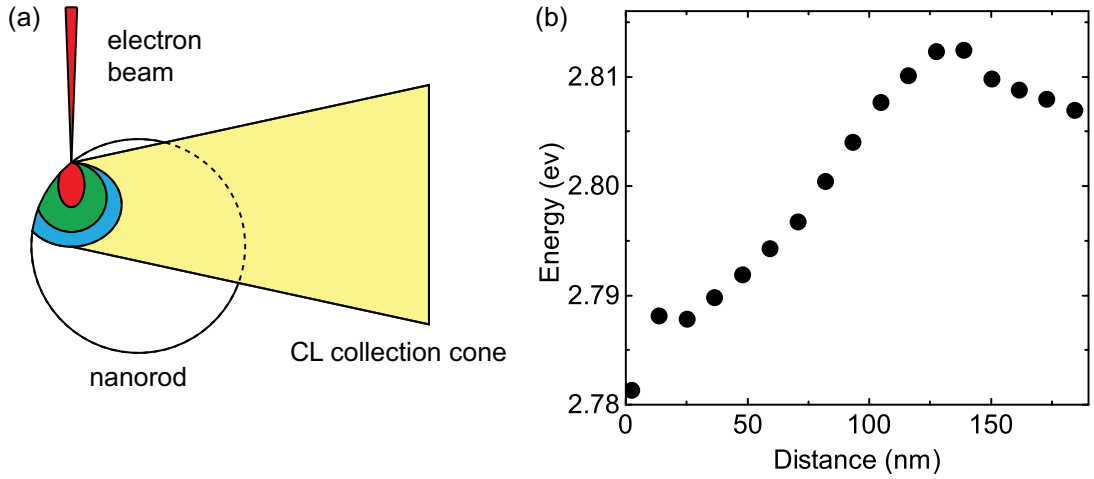

Figure 6.5: *(a) Schematic diagram showing the influence of self-absorption. Light generated on the left-hand side of the rod has to pass through the nanorod to reach the detection optics. The excitation volume induced by the electron beam is also shown. (b) Line scan through the MQW emission energy map in Fig. 6.4(c) showing a small redshift along the axis towards the top (left-hand side of the graph)of the nanorod.*

along the growth direction. The MQW emission energy changes by approximately 18 meV over the width of the MQW region; this can be seen in Fig. 6.5(b), which shows an energy line scan through the MQW region along the nanorod axis. Such a redshift could arise through a number of different mechanisms. Variation in the emission energy *within the MQW region* itself would result, for example, from well-to-well differences in composition or thickness, or from a relaxation of the compressive strain along the growth axis. However, these effects are usually interrelated, and also influence the strength of the QCSE, making it difficult to determine which one dominates. *Outside the MQW region*, however, these effects would not be expected to influence the emission energy at all, since a given pixel in the CL map corresponds to the region at which carriers are generated and not to the region where the radiative recombination occurs. Carriers generated outside the active region may diffuse to the nearest well, but the emission energy from the resultant recombination will not depend on the properties of the GaN at the point of the electron beam incidence. One mechanism which could account for the apparent shift in MQW emission as the beam scans away from the active

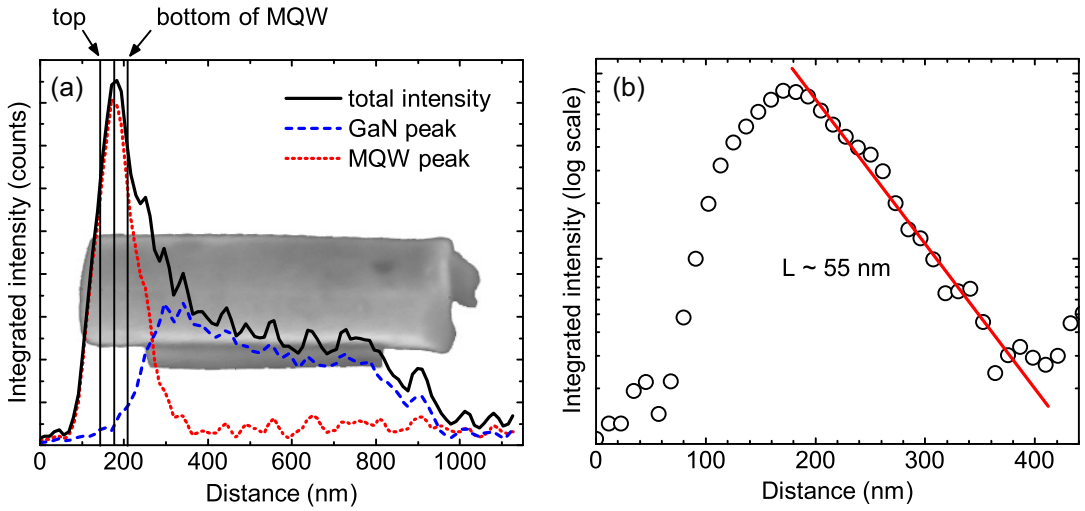

Figure 6.6: *(a) Integrated intensity line scans of the MQW and GaN emission from the CL maps in Fig. 6.4(b) and (d), respectively, superimposed on the SE image of an isolated rod. The three vertical, parallel lines mark the top, centre and bottom of the QW stack on the nanorod as determined by X-ray diffraction. The maximum of the total intensity is in good agreement with the calculated centre of the MQW region. (b) Logarithmic intensity plot of the same line scan (red dotted line in (a)) through the QW stack, fitted by a simple one-dimensional diffusion equation for calculating the carrier diffusion length L at room temperature.*

region is the screening of the electric fields due to the high density of e-beam-generated carriers, resulting in a reduction in the QCSE. Such an effect would result in an increase in emission energy when the beam is near the MQWs and in a decreased emission energy further away from this region. This effect may explain the observed redshift at both extremes of the line scan in Fig. 6.5(b), corresponding to the regions on either side of the MQWs.

Next, the line scans of the integrated intensities of the MQW and GaN emission along the nanorod axis are plotted in Fig. 6.6(a) to further investigate the emission behaviour of the MQW structure. To identify the spatial origin of the luminescence the line scans are superimposed on the SE image of the isolated nanorod on the same scale. Using X-ray diffraction the centre of the MQW structure is estimated to be approximately 77 nm below the top of the rod, which is matched to the maximum of the MQW emission intensity. The intensity profile is in good agreement with the SE image, i.e. the length of the nanorod. However,

the bottom of the rod does not show much light emission, which might be caused by structural damage sustained during detachment from the GaN template. At the other end the intensity drops down rapidly due to the electron beam scanning over the top edge. A closer look at the MQW emission intensity reveals three different slopes in the vicinity of the maximum as seen in the logarithmic plot of the integrated MQW intensity in Fig. 6.6(b). The steep drop at the top end of the nanorod is related to a combination of the limit of the sample and surface recombination. The second region on the left side of the maximum, which has a shallower slope, is related to carrier distribution within the wells, as discussed below. There is only one slope on the lower side, which is similar to the second one, but continues further into the GaN part of the rod. Carriers generated in the thick GaN layer below the MQWs can reach the wells from areas further away and contribute to the MQW intensity. This exponential decay of the intensity suggests that a simple one-dimensional diffusion equation of the form $I \propto e^{-\frac{x}{L}}$ can be used to fit the CL intensity. The calculated carrier diffusion length of $L \approx$ 55 nm for this 250 nm wide nanorod matches well with the lower limit of the diffusion length of 50–60 nm previously obtained from InGaN/GaN layers [76, 77]. It should be mentioned, however, that these diffusion lengths were estimated from dark spots (non-radiative recombination centres) in plan-view panchromatic CL images and in-plane diffusion in either material was measured, whereas here L is calculated from the intensity profile along the [0001] axis of the nanorod. The slopes on either side of the intensity maximum are very similar, as it makes no difference on which side the excitation occurs. This intensity distribution will be the result of the convolution of the carrier generation function and the QW profile, coupled with the subsequent diffusion of the carriers. Alternative methods using monochromatic CL intensity profiles and/or spot spectra were used to estimate the diffusion lengths of 100 nm and 200 nm at low temperature (5 K) in ZnMgO and ZnO nanowires [220, 221].

The same measurements were performed on a nanorod with a diameter of 215 nm. The results are displayed in Figs. 6.7, 6.8 and 6.9. The carrier diffusion length in this 215 nm nanorod was calculated to be 45 nm, which is of the same magnitude as for the 250 nm nanorod described above.

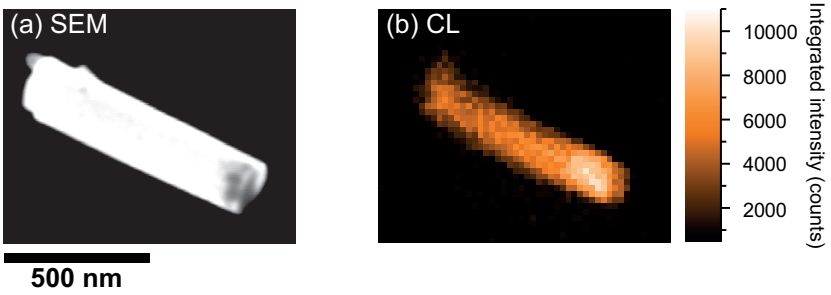

Figure 6.7: *(a) SE image and (b) corresponding room temperature panchromatic CL map of an isolated nanorod with a 215 nm diameter. The top of the nanorod is located on the right-hand side.*

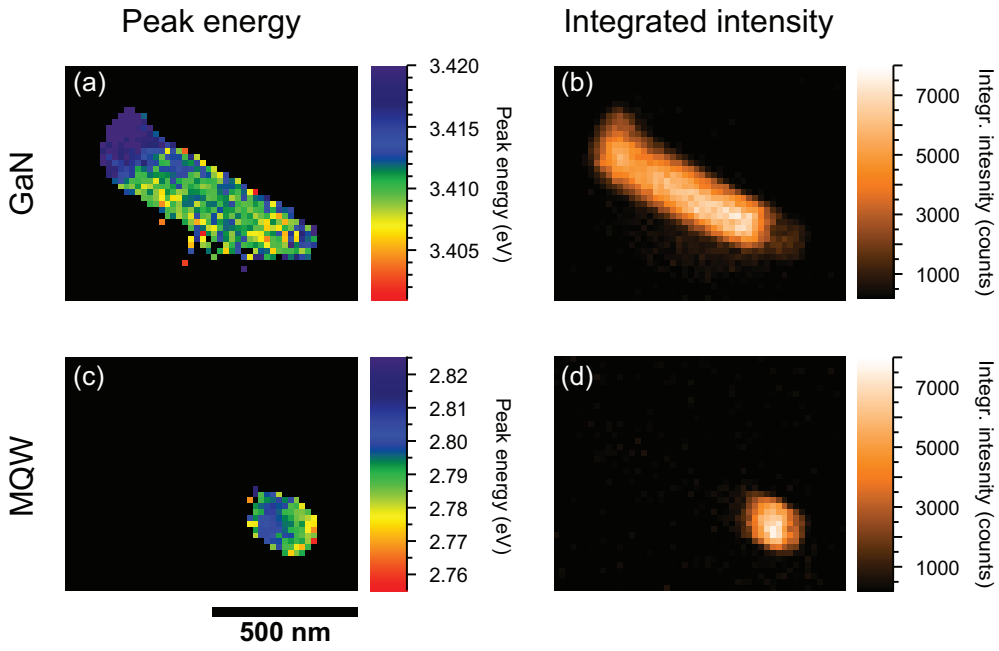

Figure 6.8: *Room temperature CL maps gained by fitting the hyperspectral data set in Fig. 6.7(b) with Voigt and Gaussian functions for the GaN and MQW emission peaks, respectively: (a) peak energy and (b) integrated intensity maps of the GaN band edge emission and (c) peak energy and (d) integrated intensity maps of the MQW emission.*

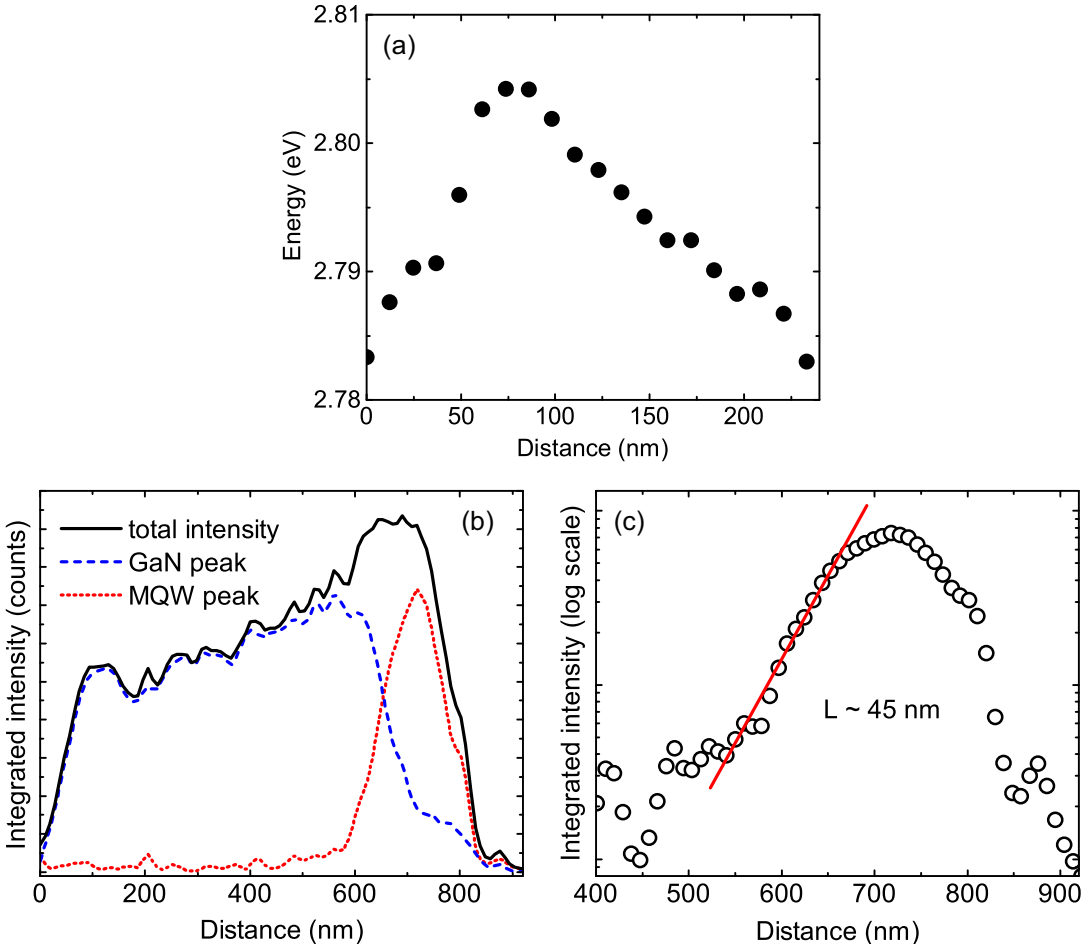

Figure 6.9: *(a) Line scan through the MQW emission energy map in Fig. 6.8(c) showing a small redshift along the axis towards the top (right-hand side) of the nanorod. (b) Integrated intensity line scans of the MQW and GaN emission from the CL maps in Fig. 6.8(b) and (d), respectively. (c) Logarithmic intensity plot of the same line scan (red dotted line in (b)) through the QW stack. The calculated carrier diffusion length is approximately 45 nm for this 215 nm wide nanorod.*

6.5 Photoluminescence of arrays of nanorods

To shed light on the strain situation, low-temperature PL spectra from the as-grown and nanorod array samples were investigated, as shown for the highest laser power of 44 mW in Fig. 6.10(a). The rows of data points above the two peaks correspond to measurements from different positions several millimetres apart on the sample and indicate the extent of a slight variation in the emission

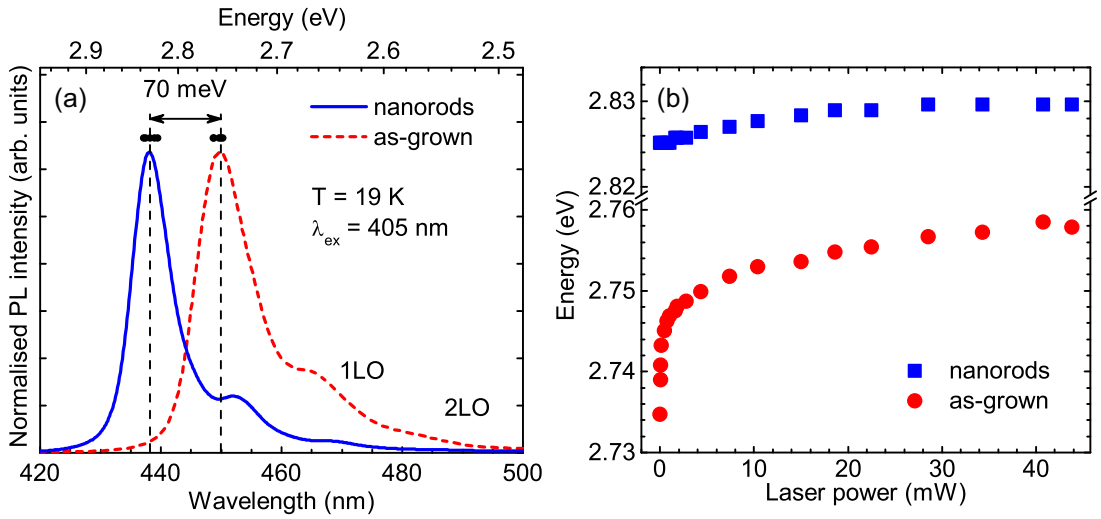

Figure 6.10: *(a) Low-temperature PL spectra show a blueshift and linewidth narrowing of the emission peak of the nanorod compared to the as-grown sample. (b) Power-dependent PL of the as-grown sample compared with the nanorod sample displays a blueshift with increasing laser power. The different magnitude of this blueshift indicates a decrease of the internal electric fields, i.e. weaker QCSE, in the nanorod sample. The spectra were recorded at 19 K.*

energy across the surface. In addition, two LO phonon replicas are resolved with a peak separation of about 90 meV. Notable differences between the spectra for the nanorod and the as-grown sample are observed; the emission energy of the nanorod sample is blueshifted by about 12 nm (70 meV) and the optical linewidth of the main emission peak (zero-phonon line) of the nanorod sample is decreased by about 20 meV in respect to the as-grown sample.

As discussed in the previous chapters, a characteristic of (0001)-oriented InGaN/GaN QW structures is the presence of strain-induced internal electric fields along the growth direction leading to the well-known QCSE, which shifts the emission peak towards lower energies. The observed blueshift is likely to be caused by a reduction of the piezoelectric polarisation, which shifts the band profile back towards the flat-band condition [33, 222]. In this case the blueshift can be interpreted as a relaxation of strain in the MQW structures after the formation of the nanorod arrays. Pseudomorphically grown InGaN wells on GaN, however, are compressively strained, which increases the band gap and hence the emission

energy compared with the unstrained case. Relaxation of the compressive strain would then result in a decrease in the emission energy. This indicates that the energy shift related to the reduction of the QCSE is stronger than the shift resulting from the reduction of the compressive strain. Fabrication of nanorods also decreased the optical linewidth of the nanorod emission, as seen in Fig. 6.10(a). With increasing piezoelectric fields the electron–hole wave function overlap decreases, which results in an inhomogeneous broadening of the linewidth [154]. The observed decrease in linewidth of the nanorods supports this finding of a reduced influence of the QCSE. The reduction of the piezoelectric field strength can be estimated to be about 0.23 MV/cm using the energy shift and the well width, which is comparable with results from similar nanorods, albeit of greater diameter, as reported in Ref. [33].

Low-temperature power-dependent PL measurements on the as-grown and nanorod samples were also performed, as displayed in Fig. 6.10(b). Although both exhibit a blueshift with increasing laser power, the shift is stronger for the as-grown sample (23 meV) compared with the nanorod sample (5 meV). As mentioned above, the influence of the QCSE results in a redshift of the emission energy. With increasing laser power more charge carriers are excited in the wells and the internal electric fields are screened to a greater extent. As a result the emission energy increases with increasing excitation intensity. The difference in the strength of this blueshift further supports the argument concerning relaxation in the InGaN well layers, since before the fabrication of the nanorods the as-grown layer is heavily strained. Fabrication of the nanorods relaxes the well material and as a result the QCSE is weaker. Therefore, the blueshift with increasing laser power is less pronounced in the nanorods than the as-grown sample. Compositional non-uniformity of the wafer as suggested in Ref. [216] is a less likely explanation, as measurements on different positions on the sample display a smaller spread in energy than the energy shift between as-grown and nanorod samples as seen by the dots above the emission peak in Fig. 6.10(a). Related work has been reported for InGaN/GaN microdisks and tapered nanoposts [222, 223].

Reciprocal space maps (RSM) using X-ray diffraction of similar nanorod structures with varying InN compositions in Ref. [224] further support the above conclusion. An RSM of the as-grown layer showed that the InGaN MQWs were pseudomorphic with the GaN buffer layer, i.e. the MQW structure is under com-

pressive strain. By contrast, an RSM of the nanorod sample displayed an increase of the in-plane lattice constant approaching the fully relaxed point. This sample had a higher InN composition than the sample discussed here and exhibited 80% strain relaxation, whereas a sample with lower InN content was almost fully relaxed. Therefore, it is most likely that the observed blueshift of the nanorods compared with the as-grown sample in Fig. 6.10(a) is due to this partial strain relaxation of the MQW structure as indicated by the RSM findings. A first study of blue LEDs employing these InGaN/GaN nanorods can be found in Ref. [213] showing enhanced emission and similar current–voltage characteristics compared with planar LEDs.

6.6 Summary

Nanorods have been fabricated from planar InGaN/GaN MQW structures using a self-assembled metal nanomask and investigated by CL and PL spectroscopy. Spatially and spectrally resolved CL hyperspectral imaging was performed on individual nanorods. The absence of an energy shift in the emission from the GaN below the MQW structures signifies that there is negligible strain variation along the rod axis in this layer. In contrast, the MQW emission energy changes by approximately 18 meV across the region containing the wells. This is either due to a change in material properties within the MQW structure (e.g. QW width, InN composition or strain relaxation) or effects outside the QW area (diffusion and screening). A line scan through the MQW emission intensity showed a simple exponential behaviour, which allows a room temperature carrier diffusion length in the GaN rod ($d = 250$ nm) of about 55 nm to be estimated. Low-temperature PL identified a 12 nm (70 meV) blueshift for the nanorod sample compared with the as-grown planar structure. Power-dependent PL of the as-grown MQW and nanorod sample showed a smaller blueshift with increasing excitation power after nanorod fabrication. This is a strong indicator for partial strain relaxation in the MQW structure as a result of a reduction in the influence of the QCSE, as also suggested by X-ray diffraction through RSM measurements.

These results will have significant impact on the use of nanorods to improve opto-electronic devices, such as white LEDs. Fabrication of nanorods and subsequent strain relaxation provides an alternative route, compared with non-/semi-

polar devices, to reducing the built-in electric fields to increase device performance. This offers a cheaper and easier path to the mass production of high performance, ultra-efficient LEDs.

Chapter 7

Hybrid nanostructure GaN/organic molecule white light-emitting diodes

7.1 Introduction

Current white LEDs either use a combination of three individual LEDs emitting in the red, green and blue spectral regions, or more commonly, a blue LED coated with a yellow emitting phosphor. The generation of white light using a combination of LEDs and energy-down converting materials is discussed in Section 2.6.

For highly efficient blue LEDs the epiwafers used for the growth of the LED structure must be of extremely high crystal quality. This results in huge manufacturing costs for the LED material. However, to ensure the commercial success of solid-state lighting the price of the end product needs to be as low as possible.

One problem of planar LEDs is the limited escape of light due to total internal reflections at the interfaces, which could lead to a waveguide effect and reabsorption of the light. Additionally, another problem is the lower IQE of the low-cost LED compared with costly and highly efficient LEDs. In Chapter 6 etched nanorods were introduced, fabricated by a simple top-down approach using a self-assembled metal nanomask. The benefits of this method are (partial) strain relaxation leading to an increase of the IQE and enhanced light extraction

due to a larger surface area [225, 226]. This approach employs low-cost standard blue-emitting epiwafers, which are commercially available. These nanorods contain InGaN/GaN MQW discs, which are exposed due to the etch process. Filling in the spaces between the nanorods with an energy down-converting material brings the converter in direct contact with the active region enhancing the energy transfer between the blue LED and the converter. This energy transfer between the MQWs and the organic material can be described by a non-radiative Förster-like energy transfer due to dipole-dipole interactions [227]. The energy transfer rate strongly depends on the distance d between the light-emitting MQW structure and the organic molecules [228]. Due to the fabrication of the nanorods the distance between the MQW structure and the organic material can approach zero, which will greatly enhance the energy transfer.

Yellow phosphors are commonly used as a converter material, however there are remaining challenges. The blue light from the LED undergoes a Stokes shift to yellow when absorbed by the phosphor. Energy losses during this process occur due to the generation of heat. Also, the yellow phosphor is susceptible to self-absorption, which further reduces the conversion process [229, 230]. Self-absorption reduces the total efficiency of the LED and also affects the colour rendering since less yellow light is contributed to the emitted spectrum. Furthermore, the energy transfer between the blue LED and the organic materials needs to be further improved. Often low-cost white LEDs appear blueish white, because too much of the blue light gets transmitted and dominates the luminescence spectrum. This has a severe impact on the quality of the white light, i.e. affects the colour rendering capabilities of the LED. Another issue is the spatial uniformity of the white light emitted from the LED, i.e. change of emission with angle [231, 232]. A varying thickness of the phosphor coating will lead to different mixing ratios of the yellow and blue emission. Different intensities of the blue light from the top surface or edges of the LED chip will have a similar influence on colour mixing. These effects will have a strong impact on the colour rendering properties of the LED, but in this case it is angle-dependent. Angular uniformity of the light emission is important for many lighting applications, such as room lighting.

Requirements of the energy down-converting material include efficient emission in the yellow-orange spectral region, absorption in the blue spectral region,

minimal self-absorption and chemical and morphological stability under the operating conditions of the final device. Commercially available materials, which may have the desired absorption and emission characteristics, however, do not meet all the requirements as stated above. Novel organic compounds have the advantage of having the ability for fine-tuning through manipulation of their chemical structure.

Organic LEDs emitting in the visible spectrum have been realised using semiconducting conjugated polymers, which lead to a hybrid white LED using an inorganic blue InGaN LED pumping a red- and green-emitting conjugated polymer system [233, 234, 235]. The BODIPY unit, an organic dye, chosen in this work for its strong fluorescence properties, has gained substantial attention in the last decade [236, 237, 238]. Its properties are summarised in Section 7.2. A small molecule will be constructed in which BODIPY will be the emitter in the yellow spectral region, linked to an absorber in the blue region. The advantages of this small molecule over polymers is the precise knowledge of its molecular structure and synthetic reproducibility [239].

In this chapter, two generations of organic materials are introduced. The targeted absorption of the organic molecule is in the blue spectral region for white light generation. The first generation of molecules is absorbing in the UV region and emitting in the yellow region. Modification of the absorbing component shifted the absorption into the violet–blue region, while the yellow emission remained the same. These organic compounds were then deposited on UV LEDs, blue LEDs, or blue-emitting nanorods, and the energy down-conversion was studied by EL and PL spectroscopy. An environmental SEM was used to investigate film formation on the nanorod structures.

7.2 Properties of BODIPY

The 4,4-difluoro-4-borata-3*a*-azonia-4*a*-aza-*s*-indacene unit, or BODIPY as it is commonly known, is an organic fluorescent dye and part of the difluoro-boraindacene family. Advantages of BODIPY are its thermal and photochemical stability, high fluorescence quantum yields, large absorption and emission profiles and good solubility in various organic solvents, such as acetone and toluene [238]. Due to its properties it has found applications in biological labelling [240], lu-

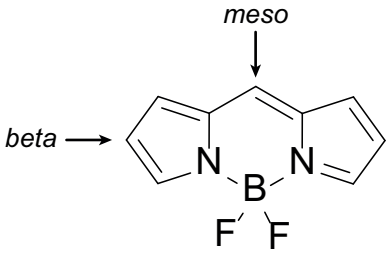

Figure 7.1: *Chemical structure of a BODIPY core unit. The meso- and beta-positions are marked with arrows.*

minescence [241], dye sensitised solar cells [242] and as sensors for pH and ions [243, 244]. Fig. 7.1 shows the chemical structure of a BODIPY core unit. Its tuneable emission characteristics in the yellow spectral region makes it attractive for organic light-emitting devices [238]. BODIPY has a strong, but narrow absorption peak, which is confined around 500 nm. Therefore, BODIPY is a good candidate as an organic converter in combination with an absorbing partner unit.

Since BODIPY absorbs and emits in the yellow spectral region another absorbing partner is needed for the absorption in the blue spectrum. For absorption in the blue region and emission in the yellow region, efficient energy transfer between the two partner units needs to occur. Förster resonant energy transfer (FRET) describes the mechanism where energy is non-radiatively transferred from a donor molecule to an acceptor molecule through dipole-dipole coupling [245]. The efficiency of the energy transfer strongly depends on the spatial separation d of the involved molecules. Another possible energy transfer, called Dexter electron transfer, is a quantum mechanical mechanism based on the exchange of an electron between two molecules [246]. Strong overlap of the wave functions of the donor and acceptor molecule is necessary. A star-shaped supramolecular system containing three BODIPY units and a truxene core emitting at the wavelengths corresponding to the BODIPY units showed energy transfer due to both Förster- and Dexter-type energy migrations processes [247].

Novel organic compounds have certain advantages over commercially available materials. Their chemical structure can be manipulated for the specific purpose of light conversion. Changing the conjugation length of the absorbing component, changing the substitution position of the BODIPY or even exchanging the

absorbing component makes it possible to fine-tune the absorption and emission characteristics to fit the desired property.

7.3 1st generation of small molecules

7.3.1 Chemical structures and physical properties

The organic compounds were synthesised by Dr. Neil Findlay (Department of Pure & Applied Chemistry, University of Strathclyde) in the group of Prof. Peter Skabara, who also supplied the basic absorption and emission characteristics in this subsection.

The first generation of small molecules are four novel, linear oligofluorene-BODIPY systems [248]. The absorbing partner consists of an oligofluorene chain, having three or four fluorene units. This chain is coupled with a BODIPY unit at the *meso*- or *beta*-position, which are marked in Fig. 7.1, forming a linear molecule. The unused positions of the BODIPY unit are blocked with a methyl (Me) or ethyl (Et) group, which also increases the stability of the final molecule. The end products are bright red-orange powders. In solution in toluene or chloroform they are fluorescent under UV irradiation. The chemical structures of these four linear oligofluorene-BODIPYs are shown in Fig. 7.2. A full description of the synthesis can be found in Ref. [248].

Absorption spectra of all four compounds as a diluted solution in dichloromethane using UV-vis spectroscopy are shown in Fig. 7.3(a). The spectra exhibit two main emission peaks. The stronger, shorter wavelength absorption band around 354–370 nm corresponds to the absorption by the oligofluorene chain, whereas the longer wavelength, less intense band around 513–527 nm stems from the BODIPY unit. Extending the conjugation length from three to four fluorene units produces a redshift of the oligofluorene absorption band by about 12–13 nm for the *meso*- and *beta*-position. The absorption is also increased by extending the conjugation. Changing the substitution position does not seem to have a large affect on the absorption. The BODIPY absorption band redshifts by about 12 nm when changing the substitution position from *beta* to *meso* for either conjugation length.

For the purpose of using these organic compounds as energy down-converters

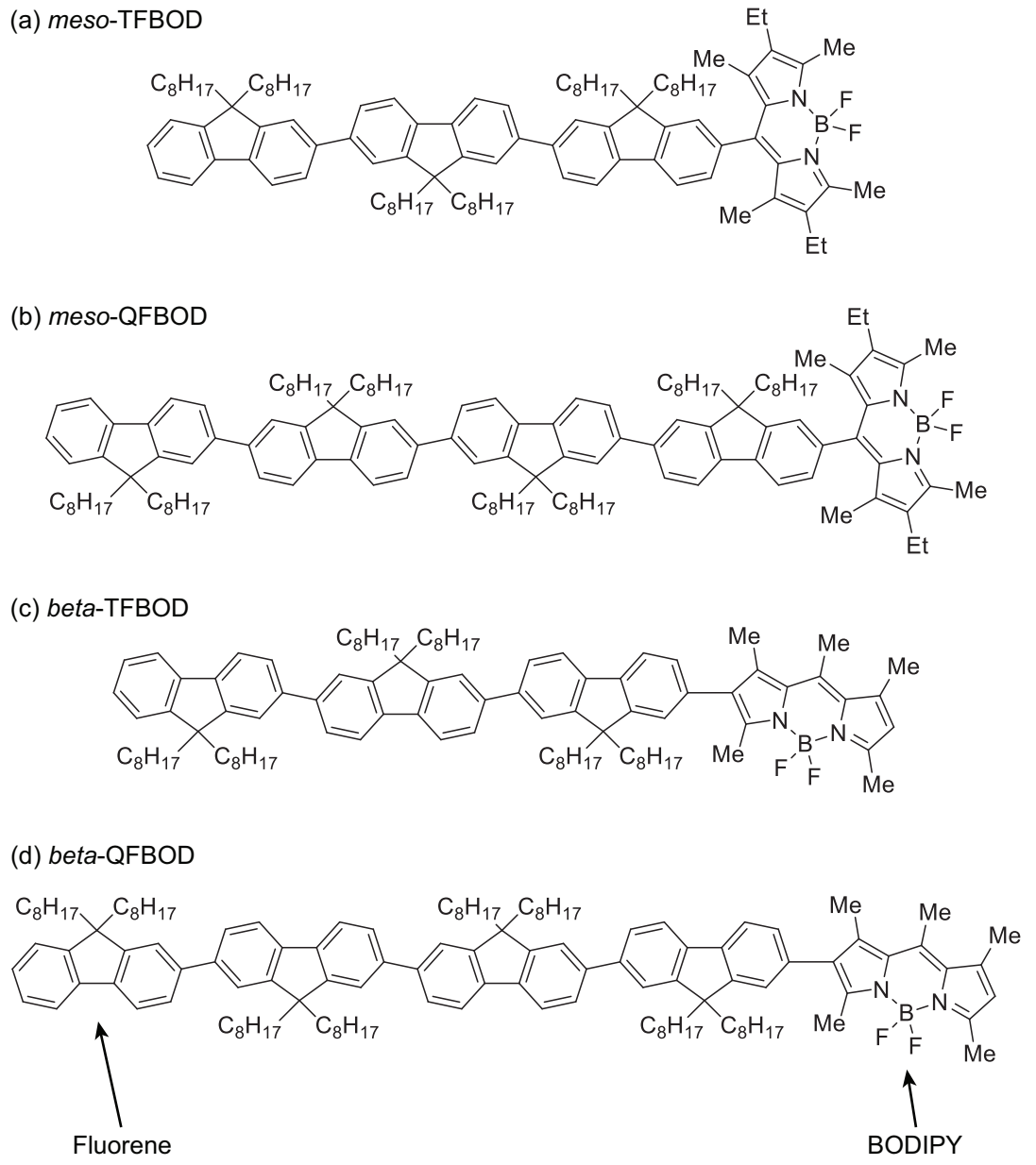

Figure 7.2: *Chemical structure of the first generation of linear oligofluorene-BODIPY molecules: (a) meso-TFBOD, (b) meso-QFBOD, (c) beta-TFBOD and (d) beta-QFBOD. Image courtesy of N. Findlay.*

efficient energy transfer between the absorbing oligofluorence chain and emitting BODIPY units needs to occur. Fig. 7.3(b) displays PL spectra measured of the four compounds in dilute dichloromethane solutions with an excitation

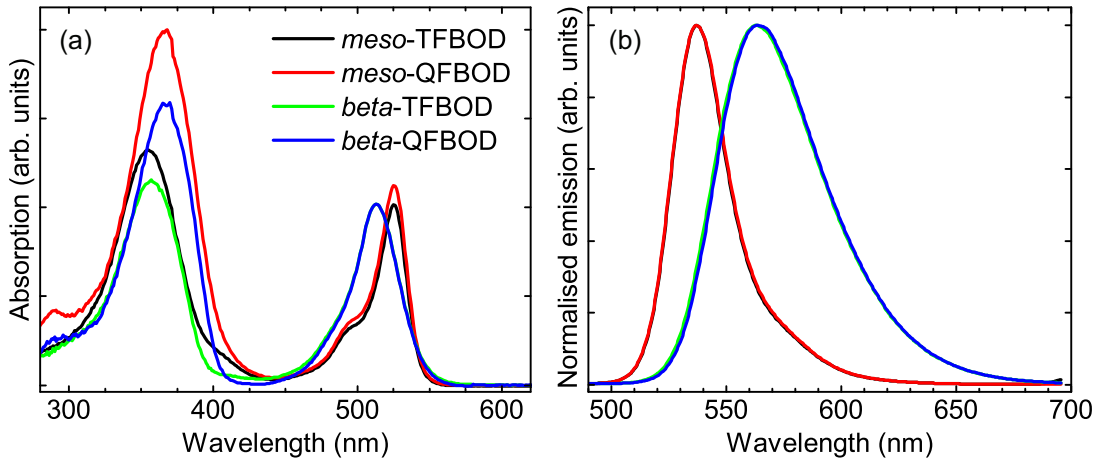

Figure 7.3: *(a) Absorption and (b) normalised PL spectra of the first generation linear oligofluorene-BODIPY compounds as dichloromethane solutions ($\approx 10^{-5}$ M and $\approx 10^{-6}$ M, respectively). The excitation wavelength for the PL measurement corresponds to the absorption maximum of the oligofluorene chain as listed in Table 7.1. The measurements were performed by N. Findlay and S. Elmasly, Department of Pure & Applied Chemistry, University of Strathclyde.*

wavelength corresponding to the absorption maximum of the oligofluorene chain. Fig. 7.3(b) shows that energy transfer between the oligofluorene chain and the BODIPY unit takes places since the oligofluorene arm is selectively excited while emission from the BODIPY was observed. Also, changing the substitution position from *meso* to *beta* broadens and redshifts the emission by about 26 nm regardless of the conjugation length.

Comparing absorption and emission spectra of the *meso*- and *beta*-substituted positions shows either a 50 nm or 10 nm Stokes shift (the difference between the absorption and emission maximum), respectively. To investigate the efficiency of the energy transfer the PL quantum yield (PLQY) of *meso*-QFBOD was measured and referenced to a known BODIPY dye (measurement performed by Dr. A. R. Inigo, Department of Pure & Applied Chemistry). The PLQY is defined as the ratio of the numbers of emitted and absorbed photons [249]. For *meso*-QFBOD the PLQY is 0.84±0.04. The absorption maxima of the oligofluorene and BODIPY units and the emission maximum of the BODIPY of the four linear oligofluorene-BODIPYs are summarised in Table 7.1.

	Absorption oligofluorene (nm)	**Absorption** BODIPY (nm)	**Photoluminescence** BODIPY (nm)
meso-TFBOD	354	526	537
meso-QFBOD	366	527	537
beta-TFBOD	357	513	563
beta-QFBOD	370	513	564

Table 7.1: *Absorption wavelength of the oligofluorene chain and BODIPY, and emission wavelength of the first generation oligofluorene-BODIPY compounds.*

7.3.2 Energy down-conversion using UV LEDs

In order to demonstrate the energy down-conversion process, *meso*-QFBOD was deposited on a commercially available, inorganic UV LED. The UV LED is based on the AlGaN material system and emits around 365 nm. The LED die is mounted in a TO46 metal can and is contacted by gold wire bonds. *meso*-QFBOD was chosen as the candidate molecule as its absorption maximum almost coincides with the emission peak of the UV LED and also as it has the strongest absorption band of the four oligofluorene-BODIPY compounds.

In an initial experiment to study the film formation and its absorption of UV light from the LED, a series of drops of *meso*-QFBOD in solution were deposited on the LED die. For the deposition process *meso*-QFBOD was dissolved in solvents such as toluene or chloroform. Using 4 mg in 1 ml of solvent, one to ten 2 μl drops were deposited on the LED die and left to dry. After these deposition steps (one, two and ten drops) room temperature EL spectra were acquired using the modified PL setup as described in Section 3.2. The spectra are not corrected for the system response over this wavelength range. Figs. 7.4(a) and (b) display EL spectra on logarithmic and linear scales, respectively, of the UV LED after deposition of the *meso*-QFBOD solution under a forward current of 5 mA. The spectra are normalised to the emission peak of the UV LED around 365 nm in order to see the changes in the emission from the organic material. The uncoated emission spectrum shows a second broad emission peak around 585 nm, which is about two orders of magnitude less intense than the UV emission. This emission band is referred to as the yellow band and its origin due to defects in the LED material was discussed in Section 5.3. After the deposition of the organic compound

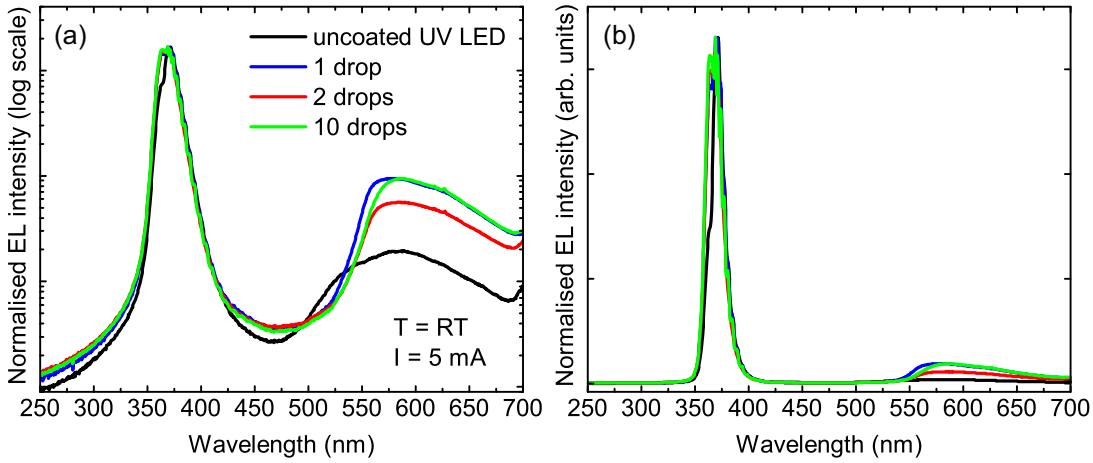

Figure 7.4: *Normalised EL spectra on a (a) logarithmic and (b) linear scale of a UV LED coated with meso-QFBOD of various film thickness under forward current of 5 mA. 1, 2 or 10 two µl drops of the meso-QFBOD solution (4 mg in 1 ml of solvent) were deposited on the LED die and left to dry. The spectra are normalised to the emission peak of the UV LED.*

the maximum of the longer wavelength peak is shifted to approximately 590 nm and its intensity is increased relative to the main LED emission. This change can be attributed to emission from *meso*-QFBOD, which is pumped by the 365 nm line of the UV LED and dominates over the defect band. The steeper drop on the shorter wavelength side is due to self-absorption by the second absorption peak of *meso*-QFBOD at 527 nm (see Fig. 7.3(a)). However, closer inspection of the film uniformity using an optical microscope showed that most of the LED die was not covered with the organic film. This would explain why the intensity of the molecule emission does not increase with the number of deposited drops.

In order to achieve a better film on the LED die, a more concentrated solution was prepared using 30 mg of *meso*-QFBOD in 1 ml of toluene. A 10 μl drop of this solution was deposited on top of the LED die. Optical microscope images of the LED with and without *meso*-QFBOD and under a forward current are shown in Figs. 7.5(a)–(c). As seen in Fig. 7.5(b) even with a higher concentrated solution a continuous film is not formed, but most of the molecule has accumulated around and between the two wire contacts. EL spectra under a forward current of 5 mA of the uncoated and *meso*-QFBOD-coated UV LED are displayed in Fig. 7.5(d).

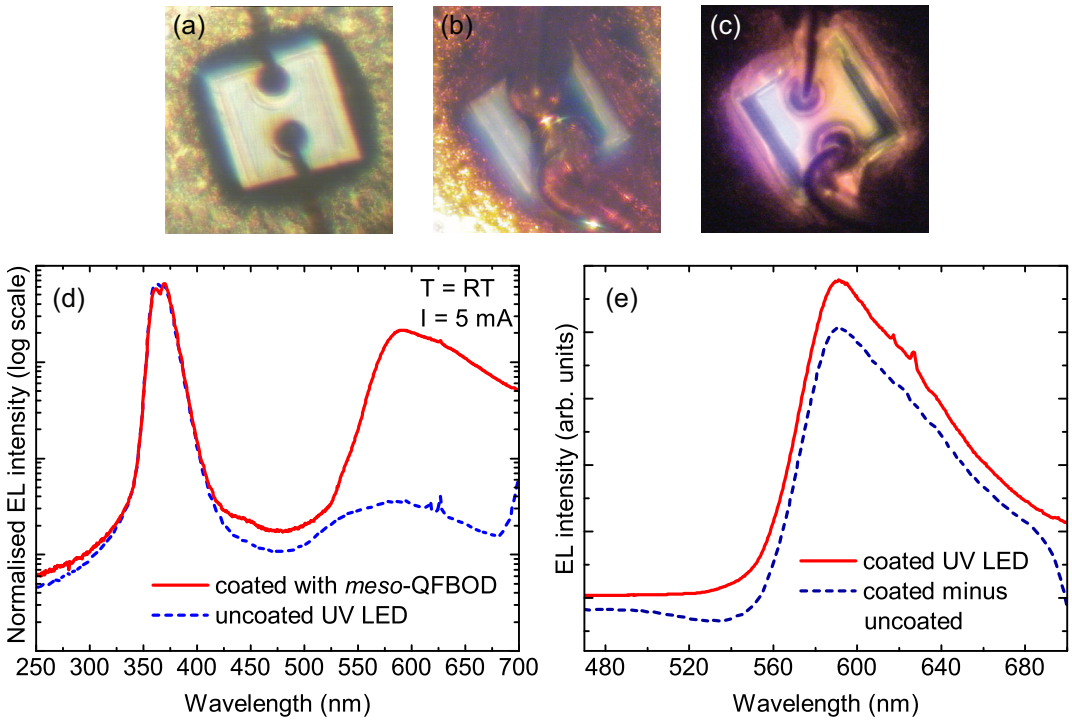

Figure 7.5: *Optical microscope image of the UV LED, (a) uncoated, (b) coated with meso-QFBOD and (c) coated and under forward current of 1 mA. The edge of the LED is 280 μm in length. (d) Normalised EL spectra of the uncoated and coated LED under forward current of 5 mA. (e) Spectrum of the uncoated UV LED subtracted from the spectrum of the meso-QFBOD coated LED compared to the spectrum of the coated LED in the region of the yellow emission. One 10 μl drop (30 mg in 1 ml of solvent) of meso-QFBOD was deposited on the LED die.*

The emission profile is similar to the previous EL measurements except that the intensity of the emission band from *meso*-QFBOD is stronger, which is due to more material being deposited on the LED. In order to show that the change of the yellow emission band is indeed caused by emission from the organic material the spectrum of the uncoated LED is subtracted from the spectrum of the LED coated with *meso*-QFBOD. Fig. 7.5(e) shows this subtraction spectrum compared with the spectrum of the coated UV LED, where the yellow spectral region is enlarged. The graph shows almost no change in the subtraction spectrum, which indicates that the emission peak at 585 nm originates from the organic material with negligible contribution from the defect band.

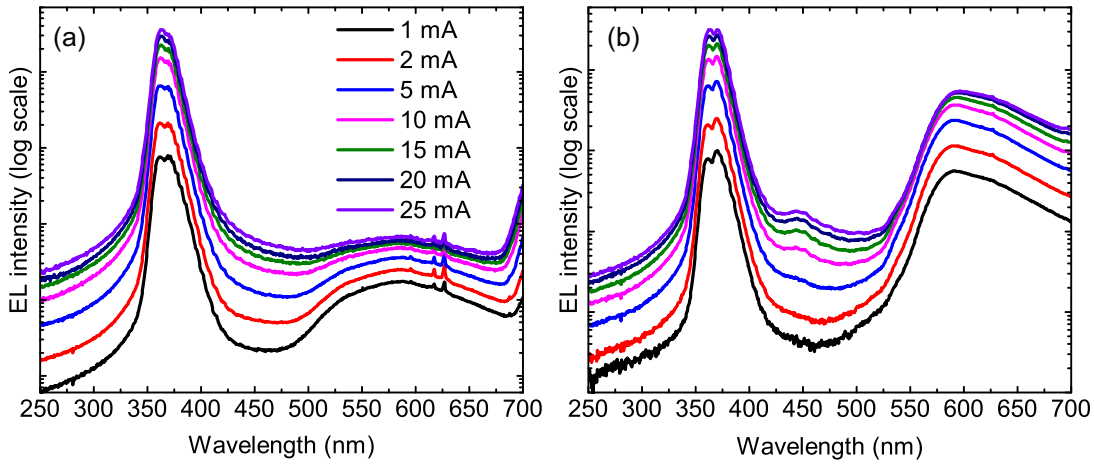

Figure 7.6: *EL current series of a UV LED (a) before and (b) after deposition of one 10 µl drop of meso-QFBOD (30 mg in 1 ml of solvent).*

This *meso*-QFBOD UV LED was also used to perform EL measurements at different currents. Fig. 7.6(a) and (b) shows EL spectra of the UV LED before and after deposition of the organic material, respectively, using currents from 1 mA to 25 mA. Without the organic material a reduction of the yellow defect band is observed with increasing current as well as a strong increase in the UV emission intensity. The relative intensity of the UV emission with respect to the intensity of the yellow band increases for larger currents as recombination at defect sites saturates due to their finite density, as seen in Fig. 7.6(a). After the deposition of *meso*-QFBOD, emission from the organic compound dominates over the defect band and with increasing current less UV light is absorbed and the intensity of the UV peak increases faster than the yellow peak. This is shown in Figs. 7.7(a) and (b) where the intensities of the UV and yellow emission and their ratio is plotted against the applied forward current. As expected Fig. 7.7(b) shows a decrease in the relative intensity of the yellow emission from the organic molecule with increasing current due to a saturation of the conversion process in the thin film. This could be caused by the saturation of the absorption, energy transfer from the absorber unit to the emitter unit of the organic molecule or emission of the organic compound.

By comparing the emission intensity of the UV peak before and after deposit-

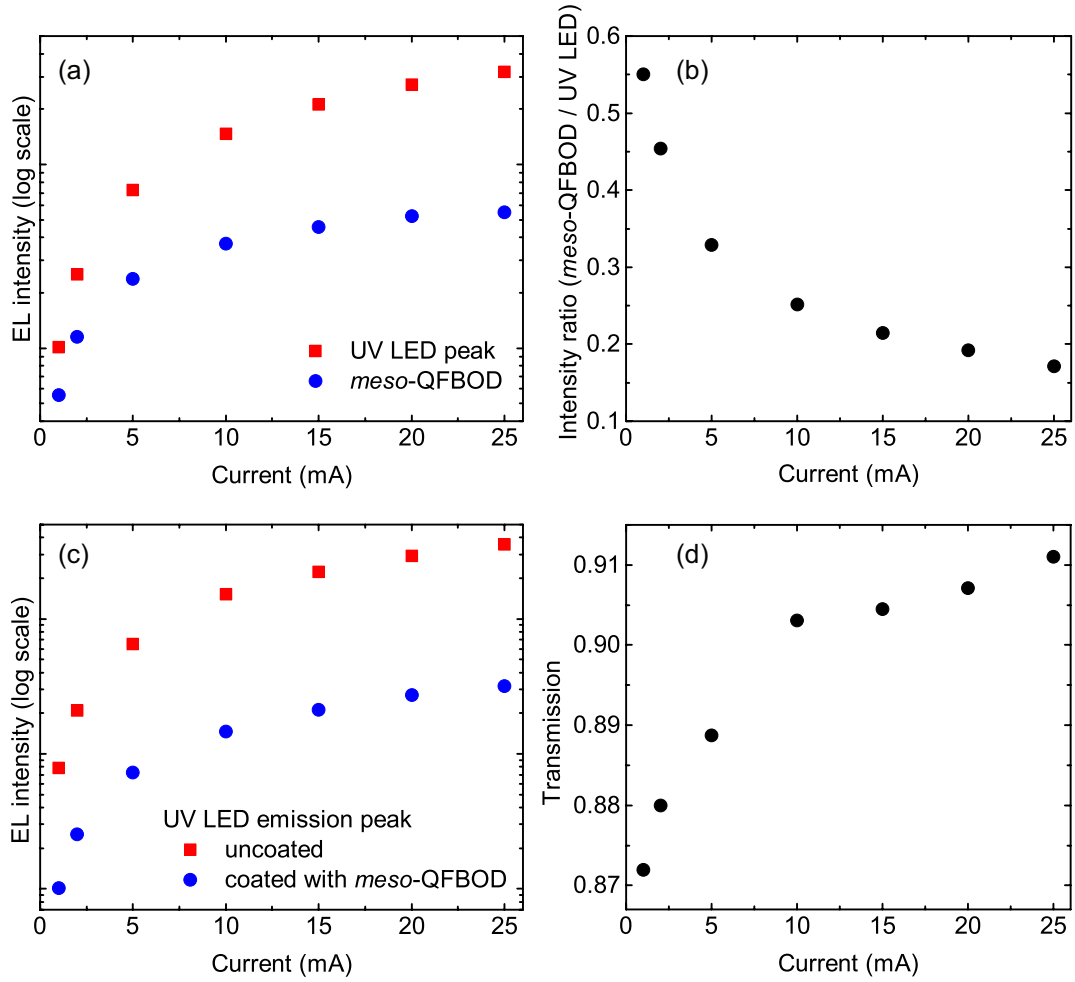

Figure 7.7: *(a) Intensities of the UV LED emission peak and yellow emission peak from meso-QFBOD of the coated LED. (b) Intensity ratio of LED yellow and LED emission peak. (c) Intensities of the UV LED emission before and after deposition of meso-QFBOD. (d) Calculated transmission of the UV emission through meso-QFBOD film.*

ing *meso*-QFBOD (Fig. 7.7(c)) it is possible to estimate how much of the UV light is transmitted through the organic material by simply calculating the difference in intensity and normalising it to the intensity of the LED without the coating:

$$T = \frac{I_{\mathrm{UV,uncoated}} - I_{\mathrm{UV,coated}}}{I_{\mathrm{UV,uncoated}}}. \tag{7.1}$$

The calculated transmission of the UV emission using Eq. (7.1) is displayed in Fig. 7.7(d). Again, with increasing current more UV light is generated and the absorption by *meso*-QFBOD starts to saturate leading to a stronger increase in the transmitted UV emission. Furthermore, optical microscope images of the LED in Figs. 7.5(b) and (c) showed that parts of the LED die were not covered by the organic material leading to UV light not being absorbed by the organic film. The contact of the wire bond might be a cause for this non-uniform deposition of the organic material and a better deposition process needs to be explored for a more efficient light conversion process.

7.4 2nd generation of small molecules

7.4.1 Chemical structures and physical properties

In the previous section organic molecules for energy down-conversion were introduced, which were absorbing in the UV and emitting in the yellow–orange spectral region. For white light generation, however, blue light is needed in addition to yellow. As in Section 7.3.1, the synthesis and measurements of the absorption and emission characteristics in this section were carried out by Dr. N. Findlay and H. McMullen.

The oligofluorene chain of the first generation of molecules, which absorbs in the UV, has been modified in order to absorb in the blue spectral region. The second generation of small molecules consists of three possible candidates and their chemical structures are displayed in Fig. 7.8. For all three molecules, the absorbing unit is placed in the centre between BODIPY units on either side. The first two molecules possess a different absorbing core. The first small molecule, $(BODFlu)_2$-BT, has an absorbing core unit consisting of a benzothiadiazole (BT) and a fluorene (Flu) on both sides. The fluorenes are connected to the BODIPY at the *meso*-position. The core of the second molecule, $(BODFluTh)_2$-FB, has a fluorobenzene (FB) at its centre, which is bordered by a thiophene (Th) and a fluorene (Flu) on either side. Again, the fluorene is substituted at the BODIPY *meso*-position. The third molecule, $(BODFlu_{\mathbf{2}}Th)_2$-FB, is an advancement of the second molecule. The core unit was changed by extending the conjugation (length of the molecular chain) of the fluorene unit from one to two. The fluorenes with

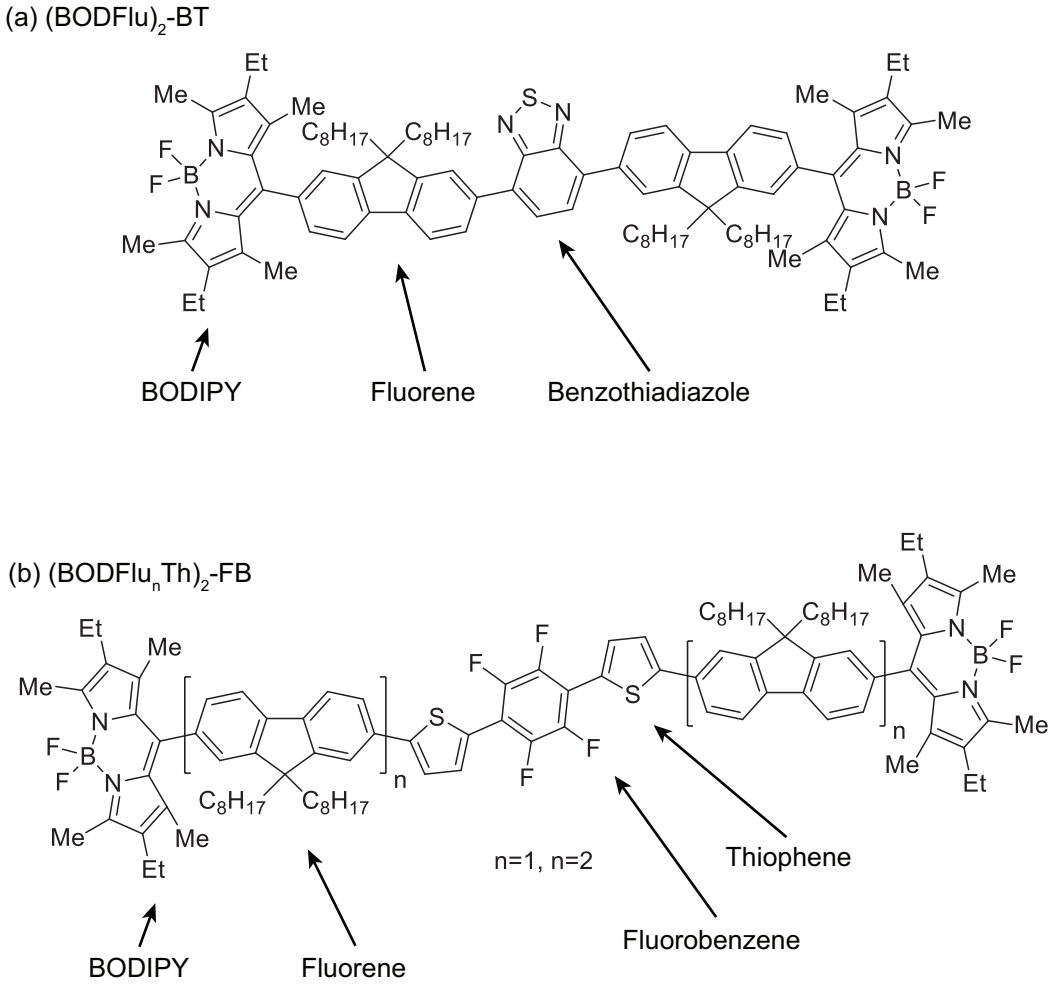

Figure 7.8: *Chemical structure of the second generation BODIPY molecules: (a) (BODFlu)$_2$-BT and (b) (BODFlu$_n$Th)$_2$-FB with $n = 1, 2$. Image courtesy of N. Findlay.*

the hydrocarbon group (C_8H_{17}) make all compounds soluble.

Absorption and PL spectra of (BODFlu)$_2$-BT and (BODFluTh)$_2$-FB ($n = 1$) are shown in Figs. 7.9(a) and (b), respectively. The absorption spectrum of (BODFlu)$_2$-BT exhibits two absorption bands from the core unit at 322 nm and one at 405 nm. The longer wavelength absorption band at 525 nm arises from the BODIPY. When excited at the second maximum the organic compound shows energy transfer to the BODIPY and emission at 550 nm occurs. (BODFluTh)$_2$-FB on the other hand shows only one absorption band at 403 nm

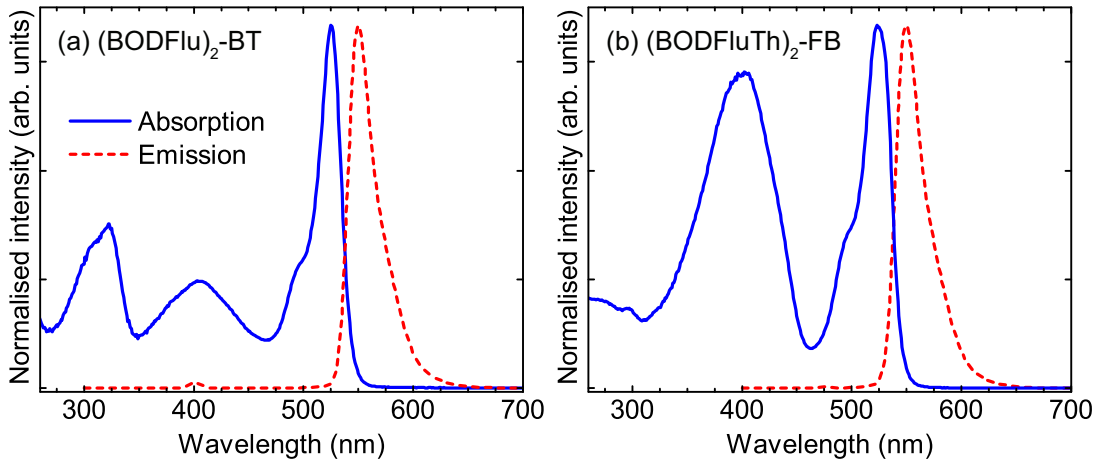

Figure 7.9: *Normalised absorption and PL spectra of the second generation BODIPY compounds with different absorbing cores: (a) (BODFlu)$_2$-BT and (b) (BODFluTh)$_2$-FB. The excitation for the PL measurements was 405 nm and 440 nm, respectively. The measurements were performed by N. Findlay and S. Elmasly, Department of Pure & Applied Chemistry, University of Strathclyde.*

besides the BODIPY absorption band, as shown in Fig. 7.9(b). Compared with the BODIPY absorption peak the absorption of (BODFluTh)$_2$-FB at 403 nm is stronger than the 405 nm absorption band of (BODFlu)$_2$-BT. The photoluminescence of (BODFluTh)$_2$-FB also shows energy transfer from the core unit to the BODIPY when excited at 440 nm, which is slightly higher than the absorption maximum, but closer to the blue emission needed for white light generation.

The absorption spectra in Fig. 7.9 always exhibit at least two absorption peaks. The absorption peak around 525 nm from the BODIPY cannot be avoided, because the desired yellow emission is generated by the BODIPY unit. It is possible, however, to increase the absorption by the core unit in the blue spectral region. To realise this, the conjugation of the fluorene unit of (BODFluTh)$_2$-FB has been doubled as shown in Fig. 7.8(b) with $n = 2$. Fig. 7.10 shows a comparison of the absorption and PL spectra of (BODFluTh)$_2$-FB and (BODFlu$_\mathbf{2}$Th)$_2$-FB. The absorption of the core unit relative to the absorption by the BODIPY has increased. Similarly, the emission intensity of (BODFlu$_2$Th)$_2$-FB compared with (BODFluTh)$_2$-FB is enhanced. The peak wavelength of the absorption and emission on the other hand displays a negligible shift after extending the conjugation

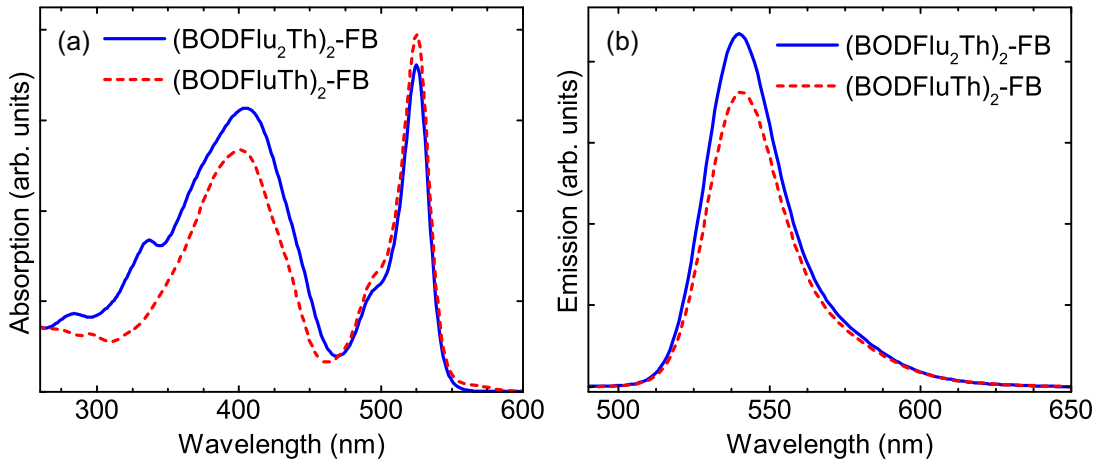

Figure 7.10: *(a) Absorption and (b) PL spectra of the second generation BODIPY compounds $(BODFluTh)_2$-FB and $(BODFlu_2Th)_2$-FB. The PL excitation wavelength for both molecules was 435 nm. The measurements were performed by N. Findlay and H. McMullen, Department of Pure & Applied Chemistry, University of Strathclyde.*

of the fluorene units.

Absorption and emission maxima of these three second generation compounds are summarised in Tab. 7.2.

	Absorption core (nm)	**Absorption** BODIPY (nm)	**Photoluminescence** BODIPY (nm)
$(BODFlu)_2$-BT	322, 405	525	550
$(BODFluTh)_2$-FB	403	525	550
$(BODFlu_2Th)_2$-FB	405	525	550

Table 7.2: *Absorption wavelength of the core and BODIPY, and emission wavelength of the three second generation BODIPY compounds.*

7.4.2 Energy down-conversion using blue-emitting nanorods and blue LEDs

In order to investigate the energy down-conversion process of the second generation small molecules $(BODFluTh)_2$-FB was chosen, because it has the strongest absorption band in the 400 nm region of the two compounds with different absorbing core units as seen in Fig. 7.9. For the conversion process fully-processed blue LEDs and blue-emitting nanorod samples containing MQWs were used.

A drop of $(BODFluTh)_2$-FB in toluene (10 mg in 1 ml) was deposited on a fully-processed LED chip from the University of Bath (courtesy of Dr. D. Allsopp and Dr. P. Shields). The LED chip is 1×1 mm^2 in size and the blue emission at approximately 445 nm is achieved by an InGaN/GaN MQW structure (6 periods, 16% InN).

Hyperspectral EL imaging at room temperature was performed on this LED. 2D EL maps representing the total integrated intensity, real colour, integrated intensity of the blue emission (400–500 nm) and yellow emission (550–800 nm) and an EL mean spectrum calculated from the entire hyperspectral image are shown in Figs. 7.11(a)–(e). The black lines in the EL images are interdigitated, metal p- and n-contacts on the surface of the LED chip. As seen in the total intensity EL map the emission intensity is very non-uniform, indicating an uneven thickness of the film across the LED chip. Regions with a thinner film are clearly shown in the integrated intensity map of the blue emission peak between 400–500 nm. More of the blue light is transmitted through the layer of organic material in areas with a thinner film in comparison with darker areas of increased film thickness such as the bottom right and top left corner of the LED chip. The integrated intensity map of the emission from $(BODFluTh)_2$-FB in the region of 550–800 nm surprisingly displays a very uniform intensity distribution as seen in Fig. 7.11(d). The intensity distribution would be uniform if the yellow emission from the organic compound would be saturated across the entire LED. If this is the case, additional blue light would be transmitted, such as in the bright areas of the blue intensity map. The darker areas in the blue intensity map might might be due to a combination of a non-uniform emission of the blue light across the LED chip, saturation of the yellow emission and a thinner organic film. Fig. 7.11(e) displays the mean EL spectrum, which was calculated using the individual EL spectrum from each pixel

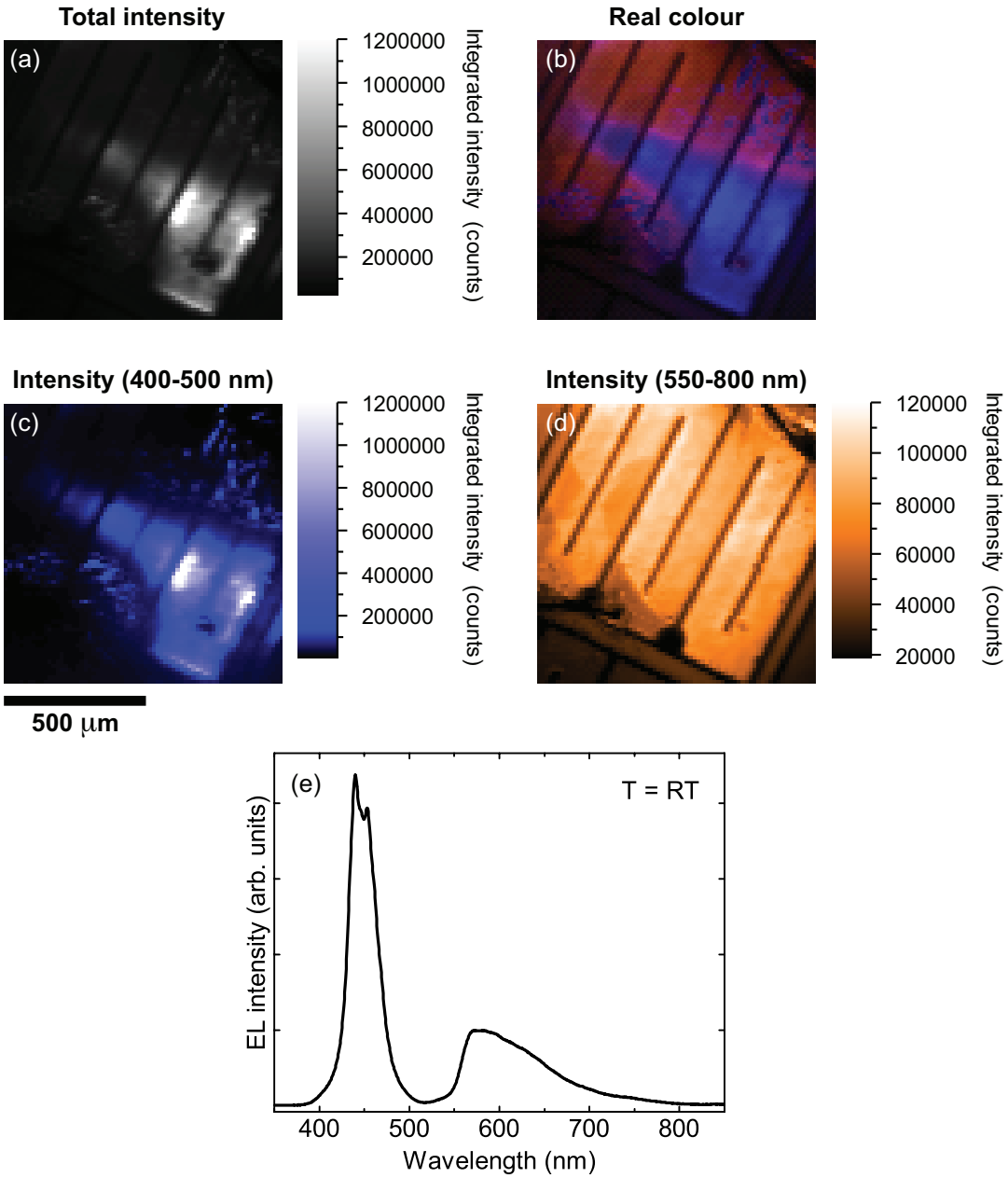

Figure 7.11: *Hyperspectral EL imaging of a fully-processed blue InGaN/GaN LED coated with one drop of $(BODFluTh)_2$-FB: (a) total integrated intensity map, (b) real colour image, (c) integrated intensity from the blue emission peak (400–500 nm) and (d) yellow emission peak (550–800 nm). (e) Mean spectrum calculated from the hyperspectral EL image. The black lines are interdigitated, metal p- and n-contacts. The LED chip was provided by D. Allsopp and P. Shields, University of Bath.*

in the hyperspectral EL map. As expected the spectrum contains two emission peaks, one from the LED and the other from the organic material. The sharp drop on the lower wavelength side is due to self-absorption of the BODIPY molecule as already observed for the first generation molecule *meso*-QFBOD in Fig. 7.4.

To study the energy down-conversion process using nanostructures the organic material was deposited on top of etched nanorods containing MQWs. The nanorod sample was fabricated at the University of Sheffield and the etching process is described in Section 6.2. The sample was specifically fabricated to match the absorption band of $(BODFluTh)_2$-FB. The emission wavelength of the nanorods is around 445 nm.

First, the formation of the organic film on the nanorods was investigated using a variable pressure (environmental) field emission gun SEM (*FEI Quanta 250*). One drop of $(BODFluTh)_2$-FB solution (10 mg in 1 μl of toluene) was deposited on the nanorods sample and left to dry. By eye it was already noticeable that the film was very non-uniform with radially increasing film thickness from the centre of the sample to the edge. Figs. 7.12(a)–(c) show SE images recorded under a pressure of 0.5 mbar of the nanorod surface from the centre towards the edge with increasing film thickness. The centre of the sample is barely covered with the organic material as seen in Fig. 7.12(a). The organic compound appears as semi-transparent haze between the nanorods in the SE image. Moving towards the edge of the sample the thickness increases and the organic material starts to fill in the space between the nanorods (Fig. 7.12(b)). At about half way to the edge the deposited compound started to form a continuous film as seen in Fig. 7.12(c) where on one side the nanorods are still quite visible and on the other side the organic material starts to accumulate on top of the nanorods. At the sample edge (Fig. 7.12(d)) a thick film has formed over the nanorods with a few broken-off rods directly on the edge due to cleaving.

In order to investigate the light conversion process PL measurements were performed on the nanorod sample coated with $(BODFluTh)_2$-FB. Since these samples are not complete LED structures (no p-n junction or metal contacts) the emission from the MQWs embedded in the nanorods is selectively excited using a 405 nm laser diode at room temperature. The excitation takes place through the polished back surface in order to minimise absorption of the laser light by the organic material on top of the nanorods. PL measurements of the sample with

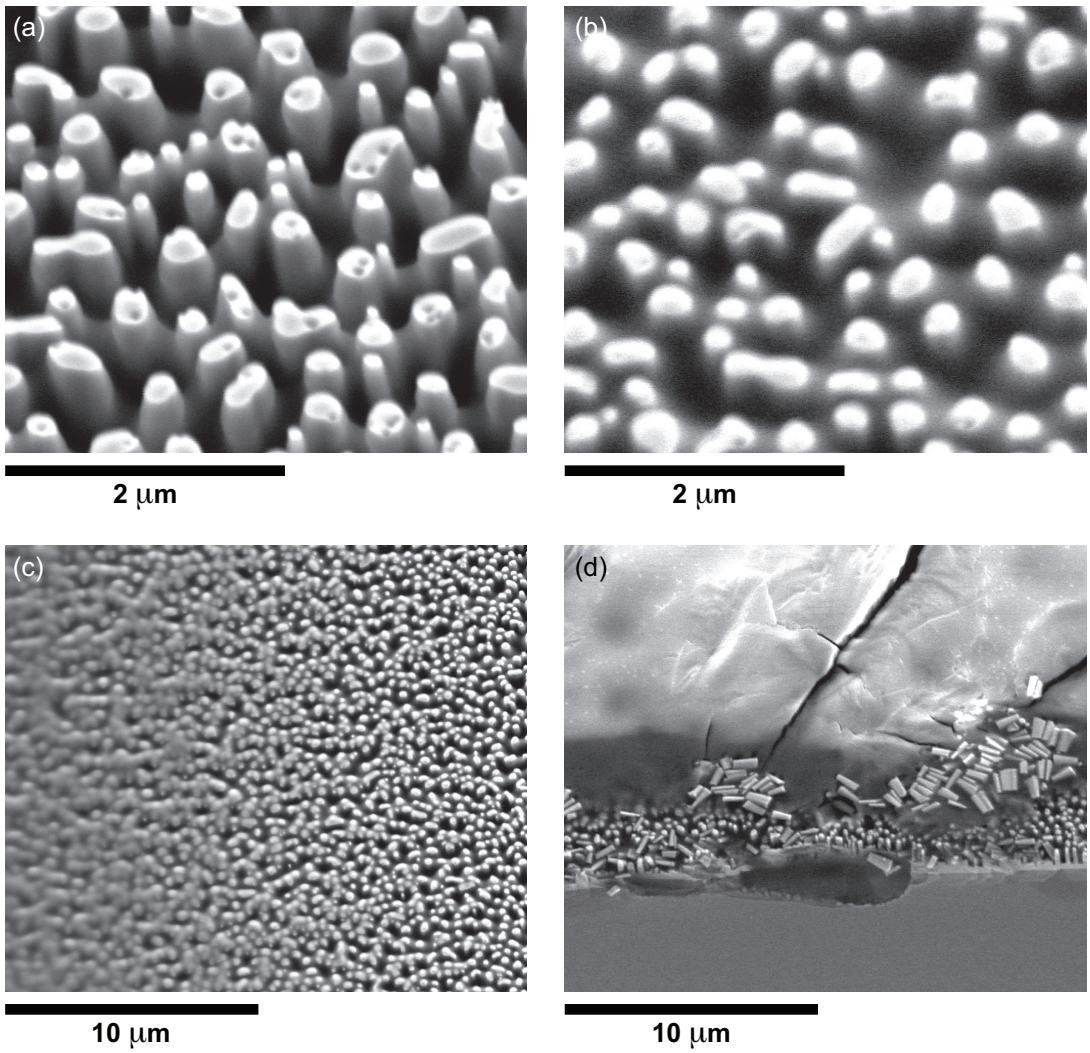

Figure 7.12: *SE images of nanorods coated with (BODFluTh)$_2$-FB using a variable pressure SEM. The film showed a gradient towards the sample edge shown in (a)–(c) and a thick layer of the organic material with broken nanorods on the sample edge as seen in (d). The sample is tilted by 45° in respect to the electron beam and the pressure is 0.5 mbar.*

different film thicknesses were recorded by subsequently adding another drop of (BODFluTh)$_2$-FB solution and letting it dry before taking a PL spectrum. The spectra of the uncoated nanorod sample and nanorods coated with up to six drops of the organic material are displayed in Fig. 7.13.

The uncoated nanorod sample only exhibits one emission peak at about

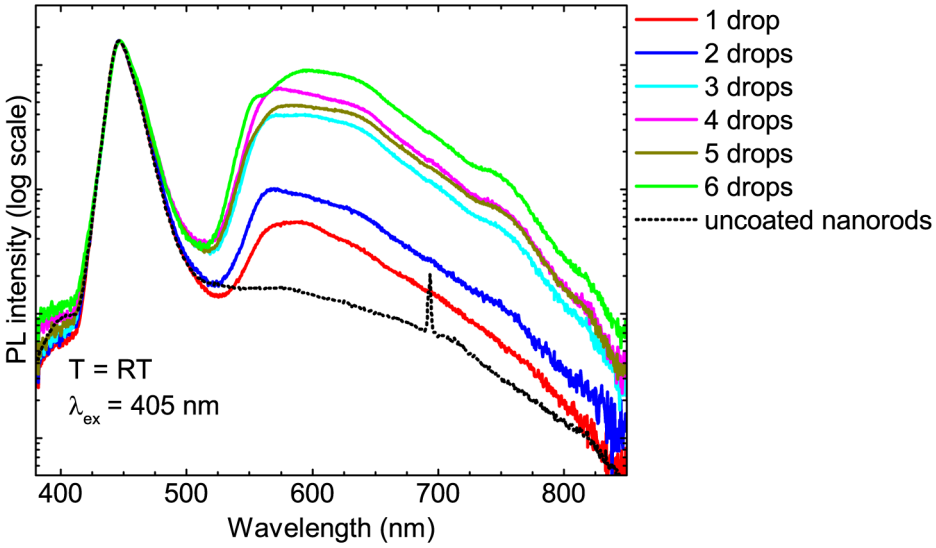

Figure 7.13: *Normalised PL (λ_{ex} = 405 nm) of InGaN/GaN MQW nanorod structures coated with (BODFluTh)$_2$-FB of various film thickness achieved by depositing one to six drops of the organic material. The spectra are normalised to the MQW emission peak of the nanorods. The excitation of the MQW emission using a 405 nm laser was carried out through the back of the sample to minimise absorption of the laser light by the organic material.*

446 nm originating from recombination within the MQW structure. Deposition of a film of (BODFluTh)$_2$-FB adds another contribution to the emission spectrum in the yellow region above 530 nm. With increasing number of deposited drops and hence film thickness the intensity of the yellow emission from the organic material is enhanced. A closer look reveals that the spectrum for drop 4 and 5 are out of order. This might be due to the formation of films of poor uniformity. Also, when adding additional drops of the solution there is a tendency for the solid layer of organic film to redissolve. The shorter wavelength side of the emission peak exhibits a rapid drop, which is due to self-absorption of the BODIPY molecule at 525 nm. Even with poor film quality and a nanorod emission wavelength that is about 40 nm away from the absorption maximum of the organic compound, emission from (BODFluTh)$_2$-FB was observed. As mentioned before, the emission wavelength of the nanorods was chosen in such a way that it is suitable for white light generation in combination with the emission from the organic

material.

In order to improve the absorption and emission profiles of the organic compound, the conjugation length of the molecular chain was extended. In the case of $(BODFluTh)_2$-FB the fluorene unit of the absorbing core is doubled to create $(BODFlu_2Th)_2$-FB. As discussed in Section 7.4.1 and seen in Fig. 7.10, the intensity of the absorption in the blue spectral region and the emission of $(BODFlu_2Th)_2$-FB has been increased compared with $(BODFluTh)_2$-FB.

For the optical analysis, $(BODFlu_2Th)_2$-FB (10 mg in 1 ml of toluene) was deposited on a fully-processed blue LED emitting at 440 nm. The LED wafer was grown by Dr. M. Kappers at the University of Cambridge and the device was fabricated by Dr. M. Hopkins at the University of Bath. EL measurements were performed using an integrating sphere (*Labsphere Illumina*). The contacted LED is located on a small piece of a fully-processed 2-inch wafer, surrounded by uncontacted LEDs. Due to scattering of the blue light in areas of the sample, which are not part of the contacted LED die, the entire sample was covered with the organic material. A photograph of the LED under operation inside the integrating sphere is shown in Fig. 7.14(a). The brightest part of the sample shows the location of the contacted LED die, whereas the remaining area emitted yellowish light, which is generated by secondary fluorescence from scattered blue light from the contacted LED.

Fig. 7.14(b) shows the EL spectrum of the LED with and without $(BODFlu_2Th)_2$-FB under a forward current of 70 mA using an integrating sphere. For clarity the spectrum of the uncoated LED was normalised to the spectrum of the coated LED, because the intensity of the blue peak of the uncoated LED was about 90 times stronger compared with the blue emission peak from the coated LED. Similar to the spectra in Figs. 7.11(e) and 7.13 with $(BODFluTh)_2$-FB as the converter molecule, the emission spectrum of the blue LED coated with $(BODFlu_2Th)_2$-FB exhibits two peaks. The LED emission is located at approximately 440 nm, whereas broad emission from the organic molecule appears at 550–700 nm.

The integrating sphere measures the absolute intensity in units of W/nm. The emission spectra, recorded by the measurement system, are corrected for the system response by using a calibrated light source for a reference measurement. This makes it possible to accurately measure parameters such as CRI, CCT and

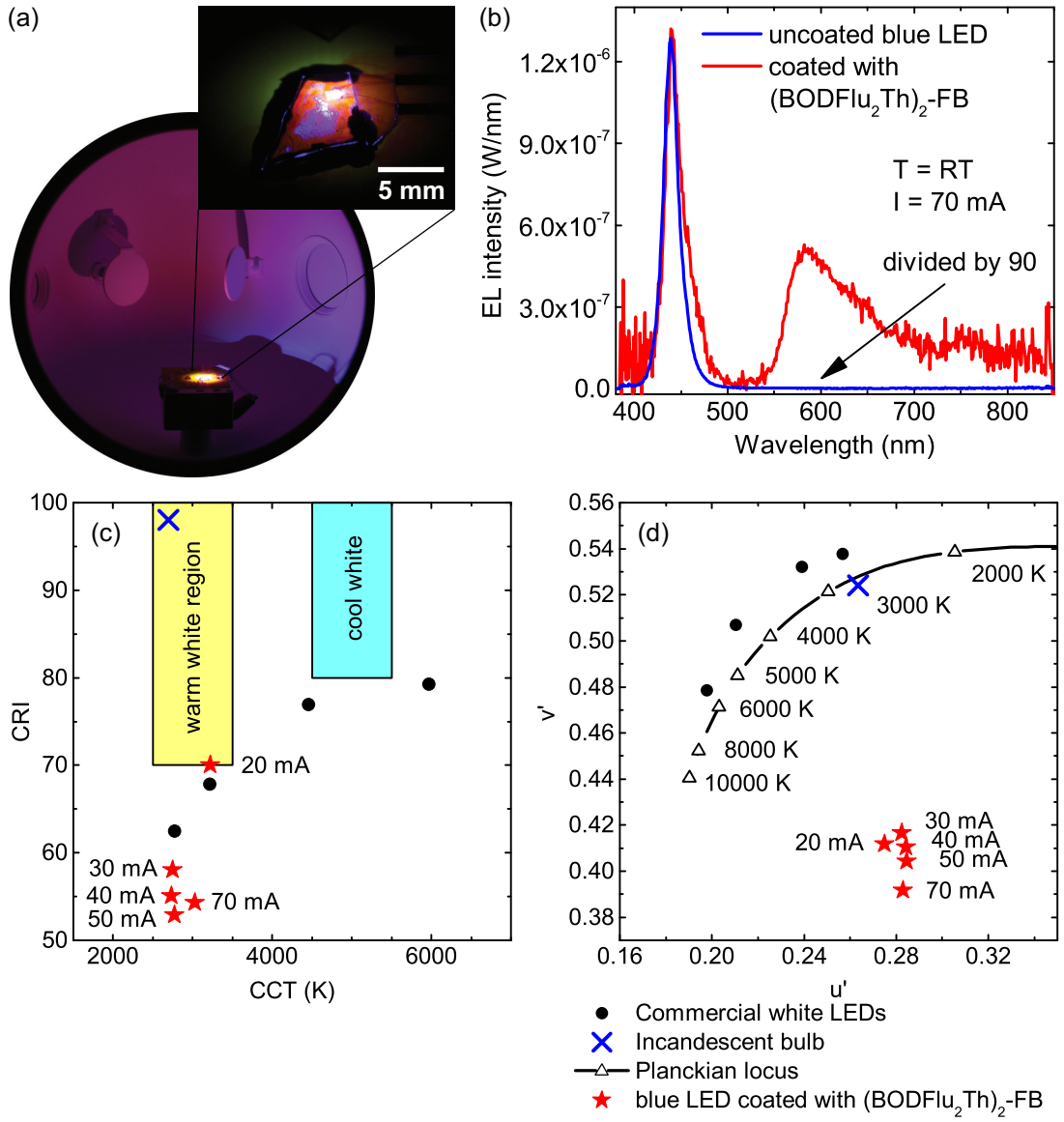

Figure 7.14: *(a) Photograph a blue InGaN/GaN LED coated with $(BODFlu_2Th)_2$-FB under operation inside an integrating sphere. The inset shows a magnification of the LED chip. (b) EL spectra of the blue LED with and without the organic material under forward current of 70 mA. The spectrum of the uncoated blue LED is divided by 90. The intensity is shown on a linear scale and corresponds to the spectrum of the coated LED (red line). (c) CRI as a function of CCT and (b) chromaticity coordinates of the coated LED operating at different currents. As a comparison the data for an incandescent light bulb and commercial white LEDs are shown. The LED wafer was grown by M. Kappers at the University of Cambridge and device fabrication was performed by M. Hopkins at the University of Bath.*

chromaticity coordinates characterising the quality of the white light emission, as described in Section 2.5. These parameters have been measured for the blue LED coated with $(BODFlu_2Th)_2$-FB operated under different currents. The results are shown in Fig. 7.14(c), where the CRI is displayed as a function of CCT, and Fig. 7.14(d), which shows a section of the CIE 1976 uniform chromaticity diagram with the chromaticity coordinates (u', v') of the blue LED coated with the organic material. For comparison the same parameters are plotted for various commercial white LEDs and an incandescent lamp.

The best CRI of 70 is obtained for a current of 20 mA. The CCT of 3220 K brings the emission colour into the region of warm white light. The yellow and blue box in Fig. 7.14(a) mark the regions of warm and cool white light, respectively. They are estimated based on the human perception of white light. With increasing current more of the blue light from the LED is transmitted through the organic compound. This leads to a decrease in the CRI with values in the range of 53–58. The CCT is reduced to 2750–3030 K. A similar effect of the drive current can be observed in the chromaticity diagram in Fig. 7.14(d). With increasing current the v' coordinate shifts to lower values. As seen in the entire chromaticity diagram in Fig. 2.11 in Section 2.5 blue light is located on the perimeter of the bottom corner. Ideally, the chromaticity coordinates should be in close proximity to the Planckian locus with the desired CCT (warm white: ≈2500–3500 K; cool white: ≈4500–5500 K). For warm white light the ideal parameters should be similar to the ones for the incandescent lamp, which has the highest CRI.

The results from Fig. 7.13 for $(BODFluTh)_2$-FB and from Fig. 7.14(b) for $(BODFlu_2Th)_2$-FB provide valuable information, but no conclusion can be drawn on which molecule exhibits a stronger emission. For the first measurement $(BODFluTh)_2$-FB was deposited on blue-emitting nanorods, which were optically pumped by a laser, whereas $(BODFlu_2Th)_2$-FB was deposited on a fully-processed blue LED with electrical contacts for carrier injection. For an absolute comparison of $(BODFluTh)_2$-FB and $(BODFlu_2Th)_2$-FB, both molecules need to be deposited on the same test structure, ideally a contacted blue LED, under the same measurement conditions. Also, the concentration of the solution used for the deposition and the thickness of the organic film should be identical.

7.5 Summary

The colour conversion characteristics of newly-synthesised organic materials, absorbing in the UV and blue spectral region and emitting yellow light, were investigated. Each compound consisted of a BODIPY unit, which accounted for the yellow emission, and an absorbing partner unit. The aim was to generate white light by combining an inorganic blue LED with a yellow-emitting organic compound.

The first generation of organic molecules comprised one BODIPY unit connected to two or three units of fluorenes at the *meso*- or *beta*-position of the BODIPY. *Meso*-QFBOD had the strongest absorption, which also matched the emission peak of a commercial AlGaN UV LEDs at 365 nm. Although, the UV LED showed a yellow emission band, due to defects in the LED material, a red-shifted and more intense emission band at 590 nm appeared after deposition of the organic compound. This band is associated with the emission from *meso*-QFBOD pumped by the UV LED.

For white light generation, the absorption band of the molecule needed to be shifted into the blue spectral region. This was achieved by exchanging the absorbing partner. The second generation consisted of an absorbing core and a BODIPY unit on either side for increased emission. The strongest absorption band was found for the compound $(BODFluTh)_2$-FB, which was chosen for deposition on fully-processed blue LEDs and blue-emitting InGaN/GaN MQW nanorods. Investigation of the film formation using a variable pressure SEM showed that the organic compound filled in the spaces between the nanorods, but also could form a continuous film on top of the rods. Luminescence measurements were performed by selectively exciting the blue MQW emission, which in turn pumps the organic compound, which is in direct contact with the active region. Stronger energy transfer between the MQW emission and the organic compound was observed when increasing the film thickness.

For further improvements of the absorption and enhancement of the emission from the organic compound, the conjugation length of the fluorene unit of the absorbing core of $(BODFluTh)_2$-FB was doubled. EL measurements of fully-processed blue LEDs coated with the modified compound, $(BODFlu_{\mathbf{2}}Th)_2$-FB, demonstrated good emission from the organic compound. Characterisation of the

quality of the white light showed a relatively high CRI of 70 and CCT of 3220 K. These values are close to the region of warm white light.

Chapter 8

Summary and future work

This work describes the optical characterisation of III-nitride materials and light-emitting devices. Firstly, the structural and luminescence properties of dislocations in a GaN epilayer were investigated, which are incorporated in most III-nitride-based opto-electronic devices. Secondly, planar InGaN/GaN MQW structures were studied, which form the basic building blocks for LEDs emitting in the blue to green spectral region. These structures then formed a template for the fabrication of nanorods, whose luminescence was investigated by CL imaging. Finally, the colour conversion of blue-emitting nanorods and blue LEDs using novel organic compounds and the quality of the white light was explored. This chapter will provide short summaries of key findings from the previous chapters and will also discuss the future work on the reported research topics.

Chapter 4 described the study of the influence of TDs on the emission characteristics in a Si-doped GaN film using CL, ECCI and AFM imaging, performed on the same micron-scale area. A one-to-one correlation was observed between TDs with B–W contrast in ECCI and dark spots in CL. A comparison measurement using AFM identified these TDs to be either of edge or screw-/mixed character. Consequently, it can be concluded that pure edge-type TDs and TDs with a screw-component act as centres for non-radiative recombination. The ambiguity over whether or not pure screw TDs are optically active was not possible to resolve. The reasons were that the density of screw-type TDs was too low (<2%) and the total TD density too high, which made it difficult to resolve dark spots in

close proximity to each other in CL. To investigate the behaviour of pure screw-type TDs and clarify this ambiguity a more suitable sample is needed. Sample requirements are a low TD density to resolve individual dislocations and a high percentage of pure screw-type TDs. Additionally, the influence of various donors and acceptors (dopants) and doping concentration on the emission properties of dislocations could be investigated.

Planar InGaN/GaN MQW structures were investigated in **Chapter 5** using PL, CL imaging and TEM. PL measurements showed a redshift of the MQW emission with increasing InN content and well width. Temperature-dependent measurements of the PL peak energy exhibited the commonly observed s-shaped behaviour due to potential fluctuations in the composition and well/barrier width. IQE measurements indicated the presence of a high density of non-radiative recombination centres at room temperature. SE imaging identified three types of trench defects on the surface of these MQW structures besides the well-known V-defect. Closed loops of narrow and wider trenches and open loops are observed. CL imaging showed that these three types have a different impact on the luminescence properties. While the area enclosed by wide trenches exhibits a large redshift and intense luminescence, the emission from the region within loops with narrower trenches is only slightly redshifted and its intensity is lower than the surrounding, defect-free area. Cross-section TEM revealed an increase of the QW thickness leading to the trench enclosed area being raised for some of the trench defects. The underlying structure of the trench defect is composed of a basal plane stacking fault connected to vertical stacking mismatch boundaries, which are terminated by the apex of a trench. Different effects can contribute to the observed luminescence characteristics, such as increase in QW thickness and InN composition, strain relaxation (formation of SMBs and BSFs), change in the QCSE and carrier localisation (potential fluctuations and InN clusters). Additionally, most of these effects are interrelated. With increasing depth and width of the trenches more enclosed material is affected by the defect, effectively separating the inside region from the surrounding. For wider trench defects carrier localisation might be the main cause, dominating over other effects, whereas for narrower trench defects localisation seems to be much weaker and the emission is governed by the increased width of the QWs. The strongly reduced intensity

of the trenches suggests that the SMBs below the trenches are associated with centres for non-radiative recombination.

Various mechanisms have been proposed for the observed luminescence characteristics of trench defects. TEM imaging further identified increased QW widths, and the presence of BSFs and SMBs. It is not possible yet, however, to unambiguously identify the cause of these changes in the optical properties. There is a direct correlation between the width of the trench and the redshift of the trench enclosed area, which is yet to be understood. A strong contender for the increased emission intensity is localisation. Atom probe tomography would be a suitable technique to measure the InN content and investigate its uniformity since it avoids the problem of beam damage, which is often an issue in TEM. It would also give information on the interface roughness, another cause for localisation. Local measurements of the electric fields within the trench defect can be performed by electron holography or differential phase contrast imaging using a high resolution TEM to study the influence of the QCSE. Structural analysis techniques with a resolution of the length scale of the trench defects (a few 100 nm) are needed for further characterisation to understand the structural properties and their influence on the luminescence.

The luminescence characteristics of single nanorods and nanorod arrays have been investigated in **Chapter 6** using CL and PL spectroscopy. Nanorods were fabricated from planar InGaN/GaN MQW structures using a self-assembled nickel metal mask for the etching process. Nanorods have been detached from the array and deposited on a Si wafer for CL imaging of single and isolated nanorods. Strong emission from the MQW region was observed at the top of the nanorod, whereas further down GaN band edge emission was detected. The GaN emission showed no shift along the axis of the rod indicating no change of strain. The MQW emission exhibited a redshift of 18 meV towards the top. This is either caused by a change in material properties within the MQW stack (change in InN content, well width or strain) or due to effects outside the QW area (carrier diffusion and screening). An intensity line scan across the MQW stack identified different slopes of the intensity profile towards the top and the base of the nanorod. The fast drop of intensity towards the top is due to the beam scanning over the top of the rod. The exponential drop of the MQW emission intensity below

the MQW structure allowed a room temperature diffusion length of 55 nm in the GaN nanorod (250 nm diameter) to be calculated, which is in agreement with diffusion lengths estimated from dark spots in CL images. PL spectroscopy of nanorod arrays showed a 70 meV blueshift of the nanorod sample compared with the planar as-grown sample. Further power-dependent PL measurements distinguished a smaller blueshift of the nanorod sample with increasing laser power compared with the as-grown sample. These findings indicate that the nanorod fabrication leads to (partial) relaxation of the strain in the MQW stack; this is supported by RSM measurements of the InGaN in-plane lattice constants.

The electric fields within the MQW structure lead to energy shifts and intensity reductions due to the QCSE. Relaxation of the strain reduces the influence of the QCSE as indicated by the experimental results. These electric fields, however, are not directly measured, but had an effect on the emission properties as determined by CL and PL spectroscopy. Direct measurements of these electric fields could confirm their change after nanorod fabrication. As previously mentioned, electron holography or differential phase contrast imaging using a TEM can map electric fields on an atomic scale. Measurements of the lattice constants by high resolution cross-section TEM also could verify the effect of strain relaxation on the lattice. A problem, which needs to be considered, is the sensitivity of the InN containing MQW structure under high energy electron irradiation, because clustering has been observed caused by the electron beam. Strain relaxation can further be studied using nanorods with different InN content in the MQW structure. Improved nanorods with more uniformity in diameter and different densities can be explored. Nanorods with a thicker capping layer could be fabricated for measurement of the carrier diffusion above and below the MQW stack. Furthermore, nanorods with differently spaced QWs or only a single well would allow the CL resolution to be tested.

In **Chapter 7** organic compounds for colour conversion, especially for the generation of white light, were investigated. Novel organic compounds, which consisted of a BODIPY moiety attached to an absorbing partner unit, were synthesised by collaborators at the Department of Pure & Applied Chemistry, University of Strathclyde. The first generation of developed molecules had an absorption band in the UV and showed yellow emission above 550 nm when deposited on top of

UV LEDs. This combination, however, did *not* yield white light, because a blue component in the the emission spectrum was missing. Therefore, the absorbing partner was exchanged and the geometry slightly modified (absorbing core between two BODIPY units) to shift the absorption band into the blue spectral region. The second generation molecules showed a broad absorption band centred at around 405 nm. Stronger absorption was observed for $(BODFluTh)_2$-FB, which was chosen for deposition on nanorods containing a MQW structure emitting blue light (445 nm). Film generation was investigated using an environmental SEM and it was shown that the organic material can be deposited between the nanorods, which brings the organic molecule in close contact to the active region. To increase the absorption the conjugation of part of the absorbing unit (fluorene unit) was doubled, which lead to an increase in absorption and emission. The modified molecule, $(BODFlu_2Th)_2$-FB, was deposited on a fully-processed blue LED structure (440 nm) and parameters describing the colour quality, such as CRI, CCT and chromaticity coordinated, were calculated. The best results yielded a CRI of 70 and CCT of 3220 K, which brings the light emission close to the region of warm white light.

The coating process was carried out by using a pipette for the deposition of drops of solution of the organic compounds on the sample. With further deposition to increase the film thickness and therefore the absorption, the previous layer was redissolved resulting in a worse quality film. To avoid this problem a higher concentrated solution of the organic compound could be used to increase the absorption. Furthermore, alternative deposition processes, such as spin coating, need to be explored to increase the uniformity of the films and make measurements on different samples comparable. The desired wavelength of the blue light from the LED is in a region of 440–460 nm. The current second generation molecules have an absorption band located at around 405 nm, which needs to be further blueshifted to match the LED emission. This could possibly be achieved by extending the conjugation, which also could increase the intensity of the absorption band, or by exchanging the absorbing core unit. As for the molecules $(BODFluTh)_2$-FB and $(BODFlu_2Th)_2$-FB, where the conjugation of the fluorene unit was doubled, further experiments need to be performed to determine the increase of the yellow emission and its influence on colour mixing to generate white light. This can be achieved by using the same blue emitter (LEDs

or nanorods) and the same properties of the organic film, such as thickness and concentration. To investigate the stability and lifetime of the organic compounds and the entire device repeated measurements could to be performed over a set period of time. In addition, encapsulating the LED chip with epoxy resin could increase the lifetime of the organic compound.

References

[1] A. Zukauskas, M. S. Shur and R. Gaska: *Introduction to Solid-state Lighting*, Wiley-Blackwell, 2002.

[2] International Energy Agency: *Light's labour's lost: Policies for energy-efficient lighting* (2006).

[3] C. J. Humphreys: *Solid-state lighting*, MRS Bull. **33**, 459 (2008).

[4] J. Swan: *UK patent no. 8* (1880).

[5] J. Swan: *UK patent no. 4933* (1880).

[6] N. Holonyak Jr. and S. F. Bevacqua: *Coherent (visible) light emission from* $Ga(As_{1-x}P_x)$ *junctions*, Appl. Phys. Lett. **1**, 82 (1962).

[7] N. Holonyak Jr.: Reader's Digest, February Issue (1963).

[8] K. T. Kamtekar, A. P. Monkman and M. R. Bryce: *Recent advances in white organic light-emitting materials and devices (WOLEDs)*, Adv. Mater. **22**, 572 (2010).

[9] R. V. Steele: *The story of a new light source*, Nature Photon. **1**, 25 (2007).

[10] R. Haitz and J. Y. Tsao: *Solid-state lighting: The case 10 years after and future prospects*, Phys. Status Solidi A **208**, 17 (2011).

[11] E. F. Schubert and J. K. Kim: *Solid-state light sources getting smart*, Science **308**, 1274 (2005).

[12] M. A. Moram: *Light-emitting diodes and their applications in energy-saving lighting*, Proceedings of the ICE - Energy **164**, 17 (2011).

[13] H. Amano, N. Sawaki, I. Akasaki and Y. Toyoda: *Metalorganic vapor phase epitaxial growth of a high quality GaN film using an AlN buffer layer*, Appl. Phys. Lett. **48**, 353 (1986).

[14] Y. Koide, N. Itoh, K. Itoh, N. Sawaki and I. Akasaki: *Effect of AlN buffer layer on AlGaN/α-Al_2O_3 heteroepitaxial growth by metalorganic vapor phase epitaxy*, Jpn. J. Appl. Phys. **27**, 1156 (1988).

[15] I. Akasaki, H. Amano, Y. Koide, K. Hiramatsu and N. Sawaki: *Effects of AlN buffer layer on crystallographic structure and on electrical and optical properties of GaN and $Ga_{1-x}Al_xN$ ($0 < x \leq 0.4$) films grown on sapphire substrate by MOVPE*, J. Cryst. Growth **98**, 209 (1989).

[16] H. Amano, M. Kito, K. Hiramatsu and I. Akasaki: *P-type conduction in Mg-doped GaN treated with low-energy electron beam irradiation (LEEBI)*, Jpn. J. Appl. Phys. **28**, L2112 (1989).

[17] S. Nakamura, T. Mukai, M. Senoh and N. Iwasa: *Thermal annealing effects on p-type Mg-doped GaN films*, Jpn. J. Appl. Phys. **31**, L139 (1992).

[18] S. Nakamura, T. Mukai and M. Senoh: *Candela-class high-brightness InGaN/AlGaN double-heterostructure blue-light-emitting diodes*, Appl. Phys. Lett. **64**, 1687 (1994).

[19] S. Nakamura, M. Senoh, S. Nagahama, N. Iwasa, T. Yamada, T. Matsushita, H. Kiyoku and Y. Sugimoto: *InGaN-based multi-quantum-well-structure laser diodes*, Jpn. J. Appl. Phys. **35**, L74 (1996).

[20] E. F. Schubert: *Light-Emitting Diodes*, Cambridge University Press, 2006, Second edn..

[21] S. Nakamura: *Current status of GaN-based solid-state lighting*, MRS Bull. **34**, 101 (2009).

[22] M. Würtele, T. Kolbe, M. Lipsz, A. Külberg, M. Weyers, M. Kneissl and M. Jekel: *Application of GaN-based ultraviolet-C light emitting diodes - UV LEDs - for water disinfection*, Water Res. **45**, 1481 (2011).

[23] I. Ichimura, F. Maeda, K. Osato, K. Yamamoto and Y. Kasami: *Optical disk recording using a GaN blue-violet laser diode*, Jpn. J. Appl. Phys. **39**, 937 (2000).

[24] G. Parish, S. Keller, P. Kozodoy, J. P. Ibbetson, H. Marchand, P. T. Fini, S. B. Fleischer, S. P. DenBaars, U. K. Mishra and E. J. Tarsa: *High-performance (Al,Ga)N-based solar-blind ultraviolet p–i–n detectors on laterally epitaxially overgrown GaN*, Appl. Phys. Lett. **75**, 247 (1999).

[25] G. Steinhoff, O. Purrucker, M. Tanaka, M. Stutzmann and M. Eickhoff: *$Al_xGa_{1-x}N$–A new material system for biosensors*, Adv. Funct. Mater. **13**, 841 (2003).

[26] C. J. Neufeld, N. G. Toledo, S. C. Cruz, M. Iza, S. P. DenBaars and U. K. Mishra: *High quantum efficiency InGaN/GaN solar cells with 2.95 eV band gap*, Appl. Phys. Lett. **93**, 143502 (2008).

[27] V. Tilak, A. Vertiatchikh, J. Jiang, N. Reeves and S. Dasgupta: *Piezoresistive and piezoelectric effects in GaN*, Phys. Status Solidi C **3**, 2307 (2006).

[28] U. K. Mishra, L. Shen, T. Kazior and Y.-F. Wu: *GaN-based RF power devices and amplifiers*, Proc. IEEE **96**, 287 (2008).

[29] N. Ikeda, Y. Niiyama, H. Kambayashi, Y. Sato, T. Nomura, S. Kato and S. Yoshida: *GaN power transistors on Si substrates for switching applications*, Proc. IEEE **98**, 1151 (2010).

[30] R. Feynman: *There's plenty of room at the bottom*, J. Microelectromech. Syst. **1**, 60 (1992).

[31] N. Taniguchi: *On the basic concept of 'nano-technology'*, Proc. Intl. Conf. Prod. Eng. Part II (1974).

[32] H.-M. Kim, Y.-H. Cho, H. Lee, S. I. Kim, S. R. Ryu, D. Y. Kim, T. W. Kang and K. S. Chung: *High-brightness light emitting diodes using dislocation-free indium gallium nitride/gallium nitride multiquantum-well nanorod arrays*, Nano Lett. **4**, 1059 (2004).

[33] C. H. Chiu, T. C. Lu, H. W. Huang, C. F. Lai, C. C. Kao, J. T. Chu, C. C. Yu, H. C. Kuo, S. C. Wang, C. F. Lin and T. H. Hsueh: *Fabrication of InGaN/GaN nanorod light-emitting diodes with self-assembled Ni metal islands*, Nanotechnology **18**, 445201 (2007).

[34] H. Sekiguchi, K. Kishino and A. Kikuchi: *Emission color control from blue to red with nanocolumn diameter of InGaN/GaN nanocolumn arrays grown on same substrate*, Appl. Phys. Lett. **96**, 231104 (2010).

[35] H.-W. Lin, Y.-J. Lu, H.-Y. Chen, H.-M. Lee and S. Gwo: *InGaN/GaN nanorod array white light-emitting diode*, Appl. Phys. Lett. **97**, 073101 (2010).

[36] T. N. Oder, J. Shakya, J. Y. Lin and H. X. Jiang: *III-nitride photonic crystals*, Appl. Phys. Lett. **83**, 1231 (2003).

[37] S. J. Pearton, B. S. Kang, S. Kim, F. Ren, B. P. Gila, C. R. Abernathy, J. Lin and S. N. G. Chu: *GaN-based diodes and transistors for chemical, gas, biological and pressure sensing*, J. Phys.: Condens. Matter **16**, R961 (2004).

[38] N. Sofikiti, N. Chaniotakis, J. Grandal, M. Utrera, M. A. Sanchez-Garcia, E. Calleja, E. Iliopoulos and A. Georgakilas: *Direct immobilization of enzymes in GaN and InN nanocolumns: The urease case study*, Appl. Phys. Lett. **95**, 113701 (2009).

[39] J. S. Wright, W. Lim, D. P. Norton, S. J. Pearton, F. Ren, J. L. Johnson and A. Ural: *Nitride and oxide semiconductor nanostructured hydrogen gas sensors*, Semicond. Sci. Technol. **25**, 024002 (2010).

[40] L. Siozade, J. Leymarie, P. Disseix, A. Vasson, M. Mihailovic, N. Grandjean, M. Leroux and J. Massies: *Modelling of thermally detected optical*

absorption and luminescence of (In,Ga)N/GaN heterostructures, Solid State Commun. **115**, 575 (2000).

[41] S. Nakamura and S. F. Chichibu (eds.): *Introduction to Nitride Semiconductor Blue Lasers and Light Emitting Diodes*, CRC Press, 2000.

[42] H. Morkoç: *Nitride Semiconductor Devices: Fundamentals and Applications*, Wiley VCH, 2013.

[43] B. Monemar: *Fundamental energy gap of GaN from photoluminescence excitation spectra*, Phys. Rev. B **10**, 676 (1974).

[44] W. Shan, B. D. Little, A. J. Fischer, J. J. Song, B. Goldenberg, W. G. Perry, M. D. Bremser and R. F. Davis: *Binding energy for the intrinsic excitons in wurtzite GaN*, Phys. Rev. B **54**, 16369 (1996).

[45] H. Fröhlich: *Electrons in lattice fields*, Adv. Phys. **3**, 325 (1954).

[46] D. Kovalev, B. Averboukh, D. Volm, B. K. Meyer, H. Amano and I. Akasaki: *Free exciton emission in GaN*, Phys. Rev. B **54**, 2518 (1996).

[47] R. Pecharromán-Gallego, P. R. Edwards, R. W. Martin and I. M. Watson: *Investigations of phonon sidebands in InGaN/GaN multi-quantum well luminescence*, Mat. Sci. Eng. B **93**, 94 (2002).

[48] F. A. Ponce, D. P. Bour, W. T. Young, M. Saunders and J. W. Steeds: *Determination of lattice polarity for growth of GaN bulk single crystals and epitaxial layers*, Appl. Phys. Lett. **69**, 337 (1996).

[49] A. R. Smith, R. M. Feenstra, D. W. Greve, J. Neugebauer and J. E. Northrup: *Reconstructions of the GaN*$(000\bar{1})$ *surface*, Phys. Rev. Lett. **79**, 3934 (1997).

[50] O. Ambacher: *Growth and applications of group III-nitrides*, J. Phys. D: Appl. Phys. **31**, 2653 (1998).

[51] C. Trager-Cowan: *Report on the evening rump session on InN – July 21, 2004 at the 2004 International Workshop on Nitride Semiconductors*, Phys. Status Solidi C **2**, 2240 (2005).

[52] F. Bernardini, V. Fiorentini and D. Vanderbilt: *Spontaneous polarization and piezoelectric constants of III-V nitrides*, Phys. Rev. B **56**, R10024 (1997).

[53] O. Ambacher, R. Dimitrov, M. Stutzmann, B. Foutz, M. Murphy, J. Smart, J. Shealy, N. Weimann, K. Chu, M. Chumbes, B. Green, A. Sierakowski, W. Schaff and L. Eastman: *Role of spontaneous and piezoelectric polarization induced effects in group-III nitride based heterostructures and devices*, Phys. Status Solidi B **216**, 381 (1999).

[54] U. M. E. Christmas, A. D. Andreev and D. A. Faux: *Calculation of electric field and optical transitions in InGaN/GaN quantum wells*, J. Appl. Phys. **98**, 073522 (2005).

[55] D. A. B. Miller, D. S. Chemla, T. C. Damen, A. C. Gossard, W. Wiegmann, T. H. Wood and C. A. Burrus: *Band-edge electroabsorption in quantum well structures: The quantum-confined stark effect*, Phys. Rev. Lett. **53**, 2173 (1984).

[56] T. Takeuchi, S. Sota, M. Katsuragawa, M. Komori, H. Takeuchi, H. Amano and I. Akasaki: *Quantum-confined stark effect due to piezoelectric fields in GaInN strained quantum wells*, Jpn. J. Appl. Phys. **36**, L382 (1997).

[57] S. F. Chichibu, A. C. Abare, M. S. Minsky, S. Keller, S. B. Fleischer, J. E. Bowers, E. Hu, U. K. Mishra, L. A. Coldren, S. P. DenBaars and T. Sota: *Effective band gap inhomogeneity and piezoelectric field in InGaN/GaN multiquantum well structures*, Appl. Phys. Lett. **73**, 2006 (1998).

[58] O. Ambacher, J. Majewski, C. Miskys, A. Link, M. Hermann, M. Eickhoff, M. Stutzmann, F. Bernardini, V. Fiorentini, V. Tilak, B. Schaff and L. F. Eastman: *Pyroelectric properties of Al(In)GaN/GaN hetero- and quantum well structures*, J. Phys.: Condens. Matter **14**, 3399 (2002).

[59] J. P. Hirth and J. Lothe: *Theory of Dislocations*, Krieger Publishing Company, 1991, Second edn..

[60] S. Kraeusel: *Native defects in the Group III Nitrides*, Ph.D. thesis, University of Strathclyde (2013).

[61] X. H. Wu, L. M. Brown, D. Kapolnek, S. Keller, B. Keller, S. P. DenBaars and J. S. Speck: *Defect structure of metal-organic chemical vapor deposition-grown epitaxial (0001) GaN/Al_2O_3*, J. Appl. Phys. **80**, 3228 (1996).

[62] R. Liu, J. Mei, S. Srinivasan, H. Omiya, F. A. Ponce, D. Cherns, Y. Narukawa and T. Mukai: *Misfit dislocation generation in InGaN epilayers on free-standing GaN*, Jpn. J. Appl. Phys. **45**, L549 (2006).

[63] F. A. Ponce: *Defects and interfaces in GaN epitaxy*, MRS Bull. **22**, 51 (1997).

[64] D. B. Holt and B. G. Yacobi: *Extended Defects in Semiconductors*, Cambridge University Press, 2007.

[65] M. D. McCluskey, L. T. Romano, B. S. Krusor, D. P. Bour, N. M. Johnson and S. Brennan: *Phase separation in InGaN/GaN multiple quantum wells*, Appl. Phys. Lett. **72**, 1730 (1998).

[66] *Commission internationale de l'Eclairage proceedings* (1931).

[67] J. J. Vos: *Colorimetric and photometric properties of a 2° fundamental observer*, Color Res. Appl. **3**, 125 (1978).

[68] D. L. MacAdam: *Specification of small chromaticity differences*, J. Opt. Soc. Am. **33**, 18 (1943).

[69] G. Wyszecki and W. S. Stiles: *Color Science: Concepts and Methods, Quantitative Data and Formulae*, Wiley-Blackwell, 2000, Second edn..

[70] M. Planck: *Ueber eine Verbesserung der Wien'schen Spectralgleichung*, Verhandlungen der Deutschen physikalischen Gesellschaft **13**, 202 (1900).

[71] M. Planck: *Ueber das Gesetz der Energieverteilung im Normalspectrum*, Ann. Phys. **309**, 553 (1901).

[72] W. Wien: *Ueber die Energievertheilung im Emissionsspectrum eines schwarzen Körpers*, Anal. Phys. **294**, 662 (1896).

[73] CIE No. 17.4: *International lighting vocabulary* (1987).

[74] E. Taylor, P. R. Edwards and R. W. Martin: *Colorimetry and efficiency of white LEDs: Spectral width dependence*, Phys. Status Solidi A **209**, 461 (2012).

[75] CIE No. 13.3: *Method of measuring and specifying colour rendering properties of light sources* (1995).

[76] S. Chichibu, K. Wada and S. Nakamura: *Spatially resolved cathodoluminescence spectra of InGaN quantum wells*, Appl. Phys. Lett. **71**, 2346 (1997).

[77] T. Sugahara, H. Sato, M. Hao, Y. Naoi, S. Kurai, S. Tottori, K. Yamashita, K. Nishino, L. T. Romano and S. Sakai: *Direct evidence that dislocations are non-radiative recombination centers in GaN*, Jpn. J. Appl. Phys. **37**, L398 (1998).

[78] H. C. Casey, B. I. Miller and E. Pinkas: *Variation of minority-carrier diffusion length with carrier concentration in GaAs liquid-phase epitaxial layers*, J. Appl. Phys. **44**, 1281 (1973).

[79] M. Ettenberg, H. Kressel and S. L. Gilbert: *Minority carrier diffusion length and recombination lifetime in GaAs:Ge prepared by liquid-phase epitaxy*, J. Appl. Phys. **44**, 827 (1973).

[80] Y.-L. Li, T. Gessmann, E. F. Schubert and J. K. Sheu: *Carrier dynamics in nitride-based light-emitting p-n junction diodes with two active regions emitting at different wavelengths*, J. Appl. Phys. **94**, 2167 (2003).

[81] C.-F. Huang, C.-F. Lu, T.-Y. Tang, J.-J. Huang and C. C. Yang: *Phosphor-free white-light light-emitting diode of weakly carrier-density-dependent spectrum with prestrained growth of InGaN/GaN quantum wells*, Appl. Phys. Lett. **90**, 151122 (2007).

[82] B. Damilano, A. Dussaigne, J. Brault, T. Huault, F. Natali, P. Demolon, P. D. Mierry, S. Chenot and J. Massies: *Monolithic white light emitting diodes using a (Ga,In)N/GaN multiple quantum well light converter*, Appl. Phys. Lett. **93**, 101117 (2008).

[83] H.-Y. Chen, H.-W. Lin, C.-H. Shen and S. Gwo: *Structure and photoluminescence properties of epitaxially oriented GaN nanorods grown on Si(111) by plasma-assisted molecular-beam epitaxy*, Appl. Phys. Lett. **89**, 243105 (2006).

[84] W. Guo, A. Banerjee, P. Bhattacharya and B. S. Ooi: *InGaN/GaN disk-in-nanowire white light emitting diodes on (001) silicon*, Appl. Phys. Lett. **98**, 193102 (2011).

[85] K. Bando, K. Sakano, Y. Noguchi and Y. Shimizu: *Development of high-bright and pure-white LED lamps*, J. Light & Vis. Env. **22**, 2 (1998).

[86] P. Schlotter, J. Baur, C. Hielscher, M. Kunzer, H. Obloh, R. Schmidt and J. Schneider: *Fabrication and characterization of GaN/InGaN/AlGaN double heterostructure LEDs and their application in luminescence conversion LEDs*, Mater. Sci. Eng. B **59**, 390 (1999).

[87] C. Ronda, T. Jüstel and H. Nikol: *Rare earth phosphors: fundamentals and applications*, J. Alloys Compd. **275**, 669 (1998).

[88] X. Guo, J. W. Graff, E. F. Schubert and R. F. Karlicek, Jr.: *Photon recycling semiconductor light-emitting diode*, Proc. SPIE **3938**, 60 (2000).

[89] X. Guo, G. D. Shen, B. L. Guan, X. L. Gu, D. Wu and Y. B. Li: *Cascade single-chip phosphor-free white light-emitting diodes*, Appl. Phys. Lett. **92**, 013507 (2008).

[90] P. Schlotter, R. Schmidt and J. Schneider: *Luminescence conversion of blue light emitting diodes*, Appl. Phys. A **64**, 417 (1997).

[91] R. D. Dupuis: *Epitaxial growth of III–V nitride semiconductors by metalorganic chemical vapor deposition*, J. Cryst. Growth **178**, 56 (1997).

[92] I. M. Watson: *Metal organic vapour phase epitaxy of AlN, GaN, InN and their alloys: A key chemical technology for advanced device applications*, Coord. Chem. Rev. **257**, 2120 (2013).

[93] J. Bai, T. Wang, P. Comming, P. J. Parbrook, J. P. R. David and A. G. Cullis: *Optical properties of AlGaN/GaN multiple quantum well structure by using a high-temperature AlN buffer on sapphire substrate*, J. Appl. Phys. **99**, 023513 (2006).

[94] H. Seiler: *Secondary electron emission in the scanning electron microscope*, J. Appl. Phys. **54**, R1 (1983).

[95] D. B. Holt and D. C. Joy (eds.): *Techniques of Physics Volume 12: SEM Microcharacterization of Semiconductors*, Academic Press, 1989.

[96] J. Goldstein, D. Newbury, D. Joy, C. Lyman, P. Echlin, E. Lifshin, L. Sawyer and J. Michael: *Scanning Electron Microscopy and X-ray Microanalysis*, Springer, 2007, Third edn..

[97] R. F. Egerton: *Physical Principles of Electron Microscopy: An Introduction to TEM, SEM, and AEM*, Springer, 2005.

[98] W. Zhou and Z. L. Wang (eds.): *Scanning Microscopy for Nanotechnology: Techniques and Applications*, Springer, 2007.

[99] K. Watanabe and M. Zelikoff: *Absorption coefficients of water vapor in the vacuum ultraviolet*, J. Opt. Soc. Am. **43**, 753 (1953).

[100] H. Bethe: *Zur Theorie des Durchgangs schneller Korpuskularstrahlen durch Materie*, Ann. Phys. **397**, 325 (1930).

[101] B. G. Yacobi and D. B. Holt: *Cathodoluminescence Microscopy of Inorganic Solids*, Plenum Press, 1990.

[102] T. E. Everhart and P. H. Hoff: *Determination of kilovolt electron energy dissipation vs penetration distance in solid materials*, J. Appl. Phys. **42**, 5837 (1971).

[103] K. Kanaya and S. Okayama: *Penetration and energy-loss theory of electrons in solid targets*, J. Phys. D: Appl. Phys. **5**, 43 (1972).

[104] D. Drouin, A. R. Couture, D. Joly, X. Tastet, V. Aimez and R. Gauvin: *CASINO v2.42 - A fast and easy-to-use modeling tool for scanning electron microscopy and microanalysis users*, Scanning **29**, 92 (2007).

[105] J. Christen, M. Grundmann and D. Bimberg: *Scanning cathodoluminescence microscopy: A unique approach to atomic-scale characterization of heterointerfaces and imaging of semiconductor inhomogeneities*, J. Vac. Sci. Technol. B **9**, 2358 (1991).

[106] R. W. Martin, P. R. Edwards, K. P. O'Donnell, M. D. Dawson, C.-W. Jeon, C. Liu, G. R. Rice and I. M. Watson: *Cathodoluminescence spectral mapping of III-nitride structures*, Phys. Status Solidi A **201**, 665 (2004).

[107] K. Pearson: *On lines and planes of closest fit to systems of points in space*, Philos. Mag. **2**, 559 (1901).

[108] P. R. Edwards, D. Sleith, A. W. Wark and R. W. Martin: *Mapping localized surface plasmons within silver nanocubes using cathodoluminescence hyperspectral imaging*, J. Phys. Chem. C **115**, 14031 (2011).

[109] P. R. Edwards and R. W. Martin: *Cathodoluminescence nanocharacterization of semiconductors*, Semicond. Sci. Technol. **26**, 064005 (2011).

[110] A. Gustafsson and E. Kapon: *Cathodoluminescence in the scanning electron microscope: Application to low-dimensional semiconductor structures*, Scanning Microscopy **12**, 285 (1998).

[111] C. Donolato: *Contrast and resolution of SEM charge-collection images of dislocations*, Appl Phys. Lett. **34**, 80 (1979).

[112] C. E. Norman: *Challenging the spatial resolution limits of CL and EBIC*, Solid State Phenom. **78-79**, 19 (2001).

[113] J. Bruckbauer, P. R. Edwards, T. Wang and R. W. Martin: *High resolution cathodoluminescence hyperspectral imaging of surface features in*

InGaN/GaN multiple quantum well structures, Appl. Phys. Lett. **98**, 141908 (2011).

[114] D. C. Joy, D. E. Newbury and D. L. Davidson: *Electron channeling patterns in the scanning electron microscope*, J. Appl. Phys. **53**, R81 (1982).

[115] G. E. Lloyd: *Atomic number and crystallographic contrast images with the SEM: A review of backscattered electron techniques*, Mineral. Mag. **51**, 3 (1987).

[116] C. Trager-Cowan, F. Sweeney, P. W. Trimby, A. P. Day, A. Gholinia, N.-H. Schmidt, P. J. Parbrook, A. J. Wilkinson and I. M. Watson: *Electron backscatter diffraction and electron channeling contrast imaging of tilt and dislocations in nitride thin films*, Phys. Rev. B **75**, 085301 (2007).

[117] G. Naresh-Kumar, B. Hourahine, P. R. Edwards, A. P. Day, A. Winkelmann, A. J. Wilkinson, P. J. Parbrook, G. England and C. Trager-Cowan: *Rapid nondestructive analysis of threading dislocations in wurtzite materials using the scanning electron microscope*, Phys. Rev. Lett. **108**, 135503 (2012).

[118] S. D. Lester, F. A. Ponce, M. G. Craford and D. A. Steigerwald: *High dislocation densities in high efficiency GaN-based light-emitting diodes*, Appl. Phys. Lett. **66**, 1249 (1995).

[119] S. J. Rosner, E. C. Carr, M. J. Ludowise, G. Girolami and H. I. Erikson: *Correlation of cathodoluminescence inhomogeneity with microstructural defects in epitaxial GaN grown by metalorganic chemical-vapor deposition*, Appl. Phys. Lett. **70**, 420 (1997).

[120] S. Mathis, A. Romanov, L. Chen, G. Beltz, W. Pompe and J. Speck: *Modeling of threading dislocation reduction in growing GaN layers*, J. Cryst. Growth **231**, 371 (2001).

[121] T. Hino, S. Tomiya, T. Miyajima, K. Yanashima, S. Hashimoto and M. Ikeda: *Characterization of threading dislocations in GaN epitaxial layers*, Appl. Phys. Lett. **76**, 3421 (2000).

[122] M. Albrecht, J. L. Weyher, B. Lucznik, I. Grzegory and S. Porowski: *Nonradiative recombination at threading dislocations in n-type GaN: Studied by cathodoluminescence and defect selective etching*, Appl. Phys. Lett. **92**, 231909 (2008).

[123] E. G. Brazel, M. A. Chin and V. Narayanamurti: *Direct observation of localized high current densities in GaN films*, Appl. Phys. Lett. **74**, 2367 (1999).

[124] K. X. Chen, Q. Dai, W. Lee, J. K. Kim, E. F. Schubert, J. Grandusky, M. Mendrick, X. Li and J. A. Smart: *Effect of dislocations on electrical and optical properties of n-type* $Al_{0.34}Ga_{0.66}N$, Appl. Phys. Lett. **93**, 192108 (2008).

[125] P. Kozodoy, J. P. Ibbetson, H. Marchand, P. T. Fini, S. Keller, J. S. Speck, S. P. DenBaars and U. K. Mishra: *Electrical characterization of GaN p-n junctions with and without threading dislocations*, Appl. Phys. Lett. **73**, 975 (1998).

[126] S. Das Bakshi, J. Sumner, M. Kappers and R. Oliver: *The influence of coalescence time on unintentional doping in GaN/sapphire*, J. Cryst. Growth **311**, 232 (2009).

[127] H. Lu, X. Cao, S. LeBoeuf, H. Hong, E. Kaminsky and S. Arthur: *Cathodoluminescence mapping and selective etching of defects in bulk GaN*, J. Cryst. Growth **291**, 82 (2006).

[128] E. Meissner, S. Schweigard, J. Friedrich, T. Paskova, K. Udwary, G. Leibiger and F. Habel: *Cathodoluminescence imaging for the determination of dislocation density in differently doped HVPE GaN*, J. Cryst. Growth **340**, 78 (2012).

[129] E. F. Schubert, I. D. Goepfert, W. Grieshaber and J. M. Redwing: *Optical properties of Si-doped GaN*, Appl. Phys. Lett. **71**, 921 (1997).

[130] W. Shan, T. J. Schmidt, X. H. Yang, S. J. Hwang, J. J. Song and B. Goldenberg: *Temperature dependence of interband transitions in GaN*

grown by metalorganic chemical vapor deposition, Appl. Phys. Lett. **66**, 985 (1995).

[131] H. Amano, K. Hiramatsu and I. Akasaki: *Heteroepitaxial growth and the effect of strain on the luminescent properties of GaN films on (*$11\bar{2}0$*) and (*0001*) sapphire substrates*, Jpn. J. Appl. Phys. **27**, L1384 (1988).

[132] L. T. Romano, C. G. Van de Walle, J. W. Ager, W. Götz and R. S. Kern: *Effect of Si doping on strain, cracking, and microstructure in GaN thin films grown by metalorganic chemical vapor deposition*, J. Appl. Phys. **87**, 7745 (2000).

[133] K. J. Lethy, P. R. Edwards, C. Liu, W. N. Wang and R. W. Martin: *Cross-sectional and plan-view cathodoluminescence of GaN partially coalesced above a nanocolumn array*, J. Appl. Phys. **112**, 023507 (2012).

[134] J. Xie, S. Mita, L. Hussey, A. Rice, J. Tweedie, J. LeBeau, R. Collazo and Z. Sitar: *On the strain in n-type GaN*, Appl Phys. Lett. **99**, 141916 (2011).

[135] M. A. Moram, M. J. Kappers, F. Massabuau, R. A. Oliver and C. J. Humphreys: *The effects of Si doping on dislocation movement and tensile stress in GaN films*, J. Appl Phys. **109**, 073509 (2011).

[136] R. Oliver, M. Kappers, J. Sumner, R. Datta and C. Humphreys: *Highlighting threading dislocations in MOVPE-grown GaN using an in situ treatment with* SiH_4 *and* NH_3, J. Cryst. Growth **289**, 506 (2006).

[137] F. Brunner, A. Mogilatenko, A. Knauer, M. Weyers and J.-T. Zettler: *Analysis of doping induced wafer bow during GaN:Si growth on sapphire*, J. Appl. Phys. **112**, 033503 (2012).

[138] P. Cantu, F. Wu, P. Waltereit, S. Keller, A. E. Romanov, S. P. DenBaars and J. S. Speck: *Role of inclined threading dislocations in stress relaxation in mismatched layers*, J. Appl. Phys. **97**, 103534 (2005).

[139] K. P. O'Donnell, M. Auf der Maur, A. Di Carlo, K. Lorenz and the SORBET consortium: *It's not easy being green: Strategies for all-nitrides, all-colour solid state lighting*, Phys. Status Solidi RRL **6**, 49 (2012).

[140] S. Pendlebury, P. Parbrook, D. Mowbray, D. Wood and K. Lee: *InGaN/GaN quantum wells with low growth temperature GaN cap layers*, J. Cryst. Growth **307**, 363 (2007).

[141] Y.-S. Lin, K.-J. Ma, C. Hsu, S.-W. Feng, Y.-C. Cheng, C.-C. Liao, C. C. Yang, C.-C. Chou, C.-M. Lee and J.-I. Chyi: *Dependence of composition fluctuation on indium content in InGaN/GaN multiple quantum wells*, Appl. Phys. Lett. **77**, 2988 (2000).

[142] J. Speck and S. Rosner: *The role of threading dislocations in the physical properties of GaN and its alloys*, Physica B **273-274**, 24 (1999).

[143] P. M. F. J. Costa, R. Datta, M. J. Kappers, M. E. Vickers, C. J. Humphreys, D. M. Graham, P. Dawson, M. J. Godfrey, E. J. Thrush and J. T. Mullins: *Misfit dislocations in In-rich InGaN/GaN quantum well structures*, Phys. Status Solidi A **203**, 1729 (2006).

[144] H. K. Cho, J. Y. Lee, C. S. Kim, G. M. Yang, N. Sharma and C. Humphreys: *Microstructural characterization of InGaN/GaN multiple quantum wells with high indium composition*, J. Cryst. Growth **231**, 466 (2001).

[145] T. Metzger, R. Höpler, E. Born, O. Ambacher, M. Stutzmann, R. Stömmer, M. Schuster, H. Göbel, S. Christiansen, M. Albrecht and H. P. Strunk: *Defect structure of epitaxial GaN films determined by transmission electron microscopy and triple-axis X-ray diffractometry*, Philos. Mag. A **77**, 1013 (1998).

[146] Y. Chen, T. Takeuchi, H. Amano, I. Akasaki, N. Yamada, Y. Kaneko and S. Y. Wang: *Pit formation in GaInN quantum wells*, Appl. Phys. Lett. **72**, 710 (1998).

[147] R. C. Powell, N.-E. Lee, Y.-W. Kim and J. E. Greene: *Heteroepitaxial wurtzite and zinc-blende structure GaN grown by reactive-ion molecular-beam epitaxy: Growth kinetics, microstructure, and properties*, J. Appl. Phys. **73**, 189 (1993).

[148] W. Qian, M. Skowronski, M. D. Graef, K. Doverspike, L. B. Rowland and D. K. Gaskill: *Microstructural characterization of α-GaN films grown on sapphire by organometallic vapor phase epitaxy*, Appl. Phys. Lett. **66**, 1252 (1995).

[149] S. M. Ting, J. C. Ramer, D. I. Florescu, V. N. Merai, B. E. Albert, A. Parekh, D. S. Lee, D. Lu, D. V. Christini, L. Liu and E. A. Armour: *Morphological evolution of InGaN/GaN quantum-well heterostructures grown by metalorganic chemical vapor deposition*, J. Appl. Phys. **94**, 1461 (2003).

[150] D. I. Florescu, S. M. Ting, J. C. Ramer, D. S. Lee, V. N. Merai, A. Parkeh, D. Lu, E. A. Armour and L. Chernyak: *Investigation of V-defects and embedded inclusions in InGaN/GaN multiple quantum wells grown by metalorganic chemical vapor deposition on (0001) sapphire*, Appl. Phys. Lett. **83**, 33 (2003).

[151] M. S. Kumar, J. Y. Park, Y. S. Lee, S. J. Chung, C.-H. Hong and E.-K. Suh: *Effect of barrier growth temperature on morphological evolution of green InGaN/GaN multi-quantum well heterostructures*, J. Phys. D: Appl. Phys. **40**, 5050 (2007).

[152] S.-L. Sahonta, M. J. Kappers, D. Zhu, T. J. Puchtler, T. Zhu, S. E. Bennett, C. J. Humphreys and R. A. Oliver: *Properties of trench defects in InGaN/GaN quantum well structures*, Phys. Status Solidi A **210**, 195, doi: 10.1002/pssa.201200408 (2012).

[153] F. C.-P. Massabuau, S.-L. Sahonta, L. Trinh-Xuan, S. Rhode, T. J. Puchtler, M. J. Kappers, C. J. Humphreys and R. A. Oliver: *Morphological, structural, and emission characterization of trench defects in InGaN/GaN quantum well structures*, Appl. Phys. Lett. **101**, 212107 (2012).

[154] K. P. O'Donnell, T. Breitkopf, H. Kalt, W. Van der Stricht, I. Moerman, P. Demeester and P. G. Middleton: *Optical linewidths of InGaN light emitting diodes and epilayers*, Appl. Phys. Lett. **70**, 1843 (1997).

[155] N. Duxbury, P. Dawson, U. Bangert, E. Thrush, W. van der Stricht, K. Jacobs and I. Moerman: *Effects of carrier gas on the properties of InGaN/GaN quantum well structures grown by MOCVD*, Phys. Status Solidi B **216**, 355 (1999).

[156] T. Ogino and M. Aoki: *Mechanism of yellow luminescence in GaN*, Jpn. J. Appl. Phys. **19**, 2395 (1980).

[157] E. R. Glaser, T. A. Kennedy, K. Doverspike, L. B. Rowland, D. K. Gaskill, J. A. Freitas, M. Asif Khan, D. T. Olson, J. N. Kuznia and D. K. Wickenden: *Optically detected magnetic resonance of GaN films grown by organometallic chemical-vapor deposition*, Phys. Rev. B **51**, 13326 (1995).

[158] D. M. Hofmann, D. Kovalev, G. Steude, B. K. Meyer, A. Hoffmann, L. Eckey, R. Heitz, T. Detchprom, H. Amano and I. Akasaki: *Properties of the yellow luminescence in undoped GaN epitaxial layers*, Phys. Rev. B **52**, 16702 (1995).

[159] J. Neugebauer and C. G. Van de Walle: *Atomic geometry and electronic structure of native defects in GaN*, Phys. Rev. B **50**, 8067 (1994).

[160] P. Perlin, T. Suski, H. Teisseyre, M. Leszczynski, I. Grzegory, J. Jun, S. Porowski, P. Bogusławski, J. Bernholc, J. C. Chervin, A. Polian and T. D. Moustakas: *Towards the identification of the dominant donor in GaN*, Phys. Rev. Lett. **75**, 296 (1995).

[161] T. Suski, P. Perlin, H. Teisseyre, M. Leszczyński, I. Grzegory, J. Jun, M. Boćkowski, S. Porowski and T. D. Moustakas: *Mechanism of yellow luminescence in GaN*, Appl. Phys. Lett. **67**, 2188 (1995).

[162] J. Neugebauer and C. G. Van de Walle: *Gallium vacancies and the yellow luminescence in GaN*, Appl. Phys. Lett. **69**, 503 (1996).

[163] K. Saarinen, T. Laine, S. Kuisma, J. Nissilä, P. Hautojärvi, L. Dobrzynski, J. M. Baranowski, K. Pakula, R. Stepniewski, M. Wojdak, A. Wysmolek, T. Suski, M. Leszczynski, I. Grzegory and S. Porowski: *Observa-*

tion of native Ga vacancies in GaN by positron annihilation, Phys. Rev. Lett. **79**, 3030 (1997).

[164] J. L. Lyons, A. Janotti and C. G. Van de Walle: *Carbon impurities and the yellow luminescence in GaN*, Appl. Phys. Lett. **97**, 152108 (2010).

[165] C. Hums, T. Finger, T. Hempel, J. Christen, A. Dadgar, A. Hoffmann and A. Krost: *Fabry-Perot effects in InGaN/GaN heterostructures on Si-substrate*, J. Appl. Phys. **101**, 033113 (2007).

[166] Y. P. Varshni: *Temperature dependence of the energy gap in semiconductors*, Physica **34**, 149 (1967).

[167] K. P. O'Donnell and X. Chen: *Temperature dependence of semiconductor band gaps*, Appl. Phys. Lett. **58**, 2924 (1991).

[168] Y.-H. Cho, G. H. Gainer, A. J. Fischer, J. J. Song, S. Keller, U. K. Mishra and S. P. DenBaars: *"S-shaped" temperature-dependent emission shift and carrier dynamics in InGaN/GaN multiple quantum wells*, Appl. Phys. Lett. **73**, 1370 (1998).

[169] H. P. D. Schenk, M. Leroux and P. de Mierry: *Luminescence and absorption in InGaN epitaxial layers and the van Roosbroeck–Shockley relation*, J. Appl. Phys. **88**, 1525 (2000).

[170] Y. Narukawa, Y. Kawakami, S. Fujita and S. Nakamura: *Dimensionality of excitons in laser-diode structures composed of $In_xGa_{1-x}N$ multiple quantum wells*, Phys. Rev. B **59**, 10283 (1999).

[171] M. Leroux, N. Grandjean, B. Beaumont, G. Nataf, F. Semond, J. Massies and P. Gibart: *Temperature quenching of photoluminescence intensities in undoped and doped GaN*, J. Appl. Phys. **86**, 3721 (1999).

[172] A. Yasan, R. McClintock, K. Mayes, D. H. Kim, P. Kung and M. Razeghi: *Photoluminescence study of AlGaN-based 280 nm ultraviolet light-emitting diodes*, Appl. Phys. Lett. **83**, 4083 (2003).

[173] K. L. Teo, J. S. Colton, P. Y. Yu, E. R. Weber, M. F. Li, W. Liu, K. Uchida, H. Tokunaga, N. Akutsu and K. Matsumoto: *An analysis of*

temperature dependent photoluminescence line shapes in InGaN, Appl. Phys. Lett. **73**, 1697 (1998).

[174] M. S. Minsky, S. B. Fleischer, A. C. Abare, J. E. Bowers, E. L. Hu, S. Keller and S. P. Denbaars: *Characterization of high-quality InGaN/GaN multiquantum wells with time-resolved photoluminescence*, Appl. Phys. Lett. **72**, 1066 (1998).

[175] J. A. Davidson, P. Dawson, T. Wang, T. Sugahara, J. W. Orton and S. Sakai: *Photoluminescence studies of InGaN/GaN multi-quantum wells*, Semicond. Sci. Technol. **15**, 497 (2000).

[176] I. A. Buyanova, W. M. Chen, G. Pozina, B. Monemar, W.-X. Ni and G. V. Hansson: *Mechanism for thermal quenching of luminescence in SiGe/Si structures grown by molecular beam epitaxy: Role of nonradiative defects*, Appl. Phys. Lett. **71**, 3676 (1997).

[177] W. Götz, N. M. Johnson, C. Chen, H. Liu, C. Kuo and W. Imler: *Activation energies of Si donors in GaN*, Appl. Phys. Lett. **68**, 3144 (1996).

[178] J. E. Northrup, L. T. Romano and J. Neugebauer: *Surface energetics, pit formation, and chemical ordering in InGaN alloys*, Appl. Phys. Lett. **74**, 2319 (1999).

[179] X. H. Wu, C. R. Elsass, A. Abare, M. Mack, S. Keller, P. M. Petroff, S. P. DenBaars, J. S. Speck and S. J. Rosner: *Structural origin of V-defects and correlation with localized excitonic centers in InGaN/GaN multiple quantum wells*, Appl. Phys. Lett. **72**, 692 (1998).

[180] I.-H. Kim, H.-S. Park, Y.-J. Park and T. Kim: *Formation of V-shaped pits in InGaN/GaN multiquantum wells and bulk InGaN films*, Appl. Phys. Lett. **73**, 1634 (1998).

[181] S. Mahanty, M. Hao, T. Sugahara, R. S. Q. Fareed, Y. Morishima, Y. Naoi, T. Wang and S. Sakai: *V-shaped defects in InGaN/GaN multiquantum wells*, Mater. Lett. **41**, 67 (1999).

[182] H. K. Cho, J. Y. Lee, G. M. Yang and C. S. Kim: *Formation mechanism of V defects in the InGaN/GaN multiple quantum wells grown on GaN layers with low threading dislocation density*, Appl. Phys. Lett. **79**, 215 (2001).

[183] D. Li, M. Sumiya, S. Fuke, D. Yang, D. Que, Y. Suzuki and Y. Fukuda: *Selective etching of GaN polar surface in potassium hydroxide solution studied by x-ray photoelectron spectroscopy*, J. Appl Phys. **90**, 4219 (2001).

[184] M. Yoshikawa, M. Murakami, H. Ishida and H. Harima: *Characterizing nanometer-sized V-defects in InGaN single quantum well films by high-spatial-resolution cathodoluminescence spectroscopy*, Appl. Phys. Lett. **94**, 131908 (2009).

[185] K. P. O'Donnell, R. W. Martin and P. G. Middleton: *Origin of luminescence from InGaN diodes*, Phys. Rev. Lett. **82**, 237 (1999).

[186] M. S. Kumar, Y. Lee, J. Park, S. Chung, C.-H. Hong and E.-K. Suh: *Surface morphological studies of green InGaN/GaN multi-quantum wells grown by using MOCVD*, Mater. Chem. Phys. **113**, 192 (2009).

[187] T. Hikosaka, T. Shioda, Y. Harada, K. Tachibana, N. Sugiyama and S. ya Nunoue: *Impact of InGaN growth conditions on structural stability under high temperature process in InGaN/GaN multiple quantum wells*, Phys. Status Solidi C **8**, 2016 (2011).

[188] S. Pereira, M. R. Correia, E. Pereira, K. P. O'Donnell, C. Trager-Cowan, F. Sweeney and E. Alves: *Compositional pulling effects in $In_xGa_{1-x}N/GaN$ layers: A combined depth-resolved cathodoluminescence and Rutherford backscattering/channeling study*, Phys. Rev. B **64**, 205311 (2001).

[189] S. Pereira, M. R. Correia, E. Pereira, K. P. O'Donnell, E. Alves, A. D. Sequeira, N. Franco, I. M. Watson and C. J. Deatcher: *Strain and composition distributions in wurtzite InGaN/GaN layers extracted from X-ray reciprocal space mapping*, Appl. Phys. Lett. **80**, 3913 (2002).

[190] S. Pereira, M. R. Correia, E. Pereira, K. P. O'Donnell, E. Alves, A. D. Sequeira, N. Franco, I. M. Watson and C. J. Deatcher: *Erratum: "Strain and composition distributions in wurtzite InGaN/GaN layers extracted from X-ray reciprocal space mapping" [Appl. Phys. Lett.* ***80****, 3913 (2002)]*, Appl. Phys. Lett. **81**, 3500 (2002).

[191] M. Hao, H. Ishikawa, T. Egawa, C. L. Shao and T. Jimbo: *Anomalous compositional pulling effect in InGaN/GaN multiple quantum wells*, Appl. Phys. Lett. **82**, 4702 (2003).

[192] T. L. Song: *Strain relaxation due to V-pit formation in* $In_xGa_{1-x}N$*/GaN epilayers grown on sapphire*, J. Appl. Phys. **98**, 084906 (2005).

[193] H. W. Choi, C. W. Jeon, M. D. Dawson, P. R. Edwards and R. W. Martin: *Fabrication and performance of parallel-addressed InGaN micro-LED arrays*, IEEE Photon. Technol. Lett. **15**, 510 (2003).

[194] P. Waltereit, O. Brandt, A. Trampert, H. T. Grahn, J. Menniger, M. Ramsteiner, M. Reiche and K. H. Ploog: *Nitride semiconductors free of electrostatic fields for efficient white light-emitting diodes*, Nature **406**, 865 (2006).

[195] U. T. Schwarz and M. Kneissl: *Nitride emitters go nonpolar*, Phys. Status Solidi RRL **1**, A44 (2007).

[196] M. Ueda, K. Kojima, M. Funato, Y. Kawakami, Y. Narukawa and T. Mukai: *Epitaxial growth and optical properties of semipolar (112) GaN and InGaN/GaN quantum wells on GaN bulk substrates*, Appl. Phys. Lett. **89**, 211907 (2006).

[197] A. Chakraborty, B. A. Haskell, S. Keller, J. S. Speck, S. P. DenBaars, S. Nakamura and U. K. Mishra: *Nonpolar InGaN/GaN emitters on reduced-defect lateral epitaxially overgrown a-plane GaN with drive-current-independent electroluminescence emission peak*, Appl. Phys. Lett. **85**, 5143 (2004).

[198] M. Funato and Y. Kawakami: *Semipolar III nitride semiconductors: Crystal growth, device fabrication, and optical anisotropy*, MRS Bull. **34**, 334 (2009).

[199] J. S. Speck and S. F. Chichibu: *Nonpolar and semipolar group III nitride-based materials*, MRS Bull. **34**, 304 (2009).

[200] S. Li, X. Wang, S. Fündling, M. Erenburg, J. Ledig, J. Wei, H. H. Wehmann, A. Waag, W. Bergbauer, M. Mandl, M. Strassburg, A. Trampert, U. Jahn, H. Riechert, H. Jönen and A. Hangleiter: *Nitrogen-polar core-shell GaN light-emitting diodes grown by selective area metalorganic vapor phase epitaxy*, Appl. Phys. Lett. **101**, 032103 (2012).

[201] H.-M. Kim, D. S. Kim, D. Y. Kim, T. W. Kang, Y.-H. Cho and K. S. Chung: *Growth and characterization of single-crystal GaN nanorods by hydride vapor phase epitaxy*, Appl. Phys. Lett. **81**, 2193 (2002).

[202] R. Yan, D. Gargas and P. Yang: *Nanowire photonics*, Nature Photon. **3**, 569 (2009).

[203] V. Ramesh, A. Kikuchi, K. Kishino, M. Funato and Y. Kawakami: *Strain relaxation effect by nanotexturing InGaN/GaN multiple quantum well*, J. Appl. Phys. **107**, 114303 (2010).

[204] S. D. Hersee, A. K. Rishinaramangalam, M. N. Fairchild, L. Zhang and P. Varangis: *Threading defect elimination in GaN nanowires*, J. Mater. Res. **26**, 2293 (2001).

[205] S. X. Jin, J. Li, J. Y. Lin and H. X. Jiang: *InGaN/GaN quantum well interconnected microdisk light emitting diodes*, Appl. Phys. Lett. **77**, 3236 (2000).

[206] S. H. Kim, H. H. Park, Y. H. Song, H. J. Park, J. B. Kim, S. R. Jeon, H. Jeong, M. S. Jeong and G. M. Yang: *An improvement of light extraction efficiency for GaN-based light emitting diodes by selective etched nanorods in periodic microholes*, Opt. Express **21**, 7125 (2013).

[207] H. W. Seo, L. W. Tu, Y. T. Lin, C. Y. Ho, Q. Y. Chen, L. Yuan, D. P. Norman and N. J. Ho: *p-GaN/InGaN/n-GaN pedestal nanorods: Effect of postgrowth annealing on the electrical performance*, Appl. Phys. Lett. **94**, 201907 (2009).

[208] W. Bergbauer, M. Strassburg, C. Kölper, N. Linder, C. Roder, J. Lähnemann, A. Trampert, S. Fündling, S. F. Li, H.-H. Wehmann and A. Waag: *Continuous-flux MOVPE growth of position-controlled N-face GaN nanorods and embedded InGaN quantum wells*, Nanotechnology **21**, 305201 (2010).

[209] G. Kunert, W. Freund, T. Aschenbrenner, C. Kruse, S. Figge, M. Schowalter, A. Rosenauer, J. Kalden, K. Sebald, J. Gutowski, M. Feneberg, I. Tischer, K. Fujan, K. Thonke and D. Hommel: *Light-emitting diode based on mask- and catalyst-free grown N-polar GaN nanorods*, Nanotechnology **22**, 265202 (2011).

[210] N. Pan, X. Wang, M. Li, F. Li and J. G. Hou: *Strong surface effect on cathodoluminescence of an individual tapered ZnO nanorod*, J. Phys. Chem. C **111**, 17265 (2007).

[211] M. Schirra, A. Reiser, G. M. Prinz, A. Ladenburger, K. Thonke and R. Sauer: *Cathodoluminescence study of single zinc oxide nanopillars with high spatial and spectral resolution*, J. Appl. Phys. **101**, 113509 (2007).

[212] K. Xing, Y. Gong, J. Bai and T. Wang: *InGaN/GaN quantum well structures with greatly enhanced performance on a-plane GaN grown using self-organized nano-masks*, Appl. Phys. Lett. **99**, 181907 (2011).

[213] J. Bai, Q. Wang and T. Wang: *Greatly enhanced performance of InGaN/GaN nanorod light emitting diodes*, Phys. Status Solidi A **209**, 477 (2012).

[214] R. J. Shul, L. Zhang, A. G. Baca, C. G. Willison, J. Han, S. J. Pearton and F. Ren: *Inductively coupled plasma-induced etch damage of GaN p-n junctions*, J. Vac. Sci. Technol. A **18**, 1139 (2000).

[215] S. Y. Han, H. S. Yang, K. H. Baik, S. J. Pearton and F. Ren: *Role of ion energy and flux on inductively coupled plasma etch damage in InGaN/GaN multi quantum well light emitting diodes*, Jpn. J. Appl. Phys. **44**, 7234 (2005).

[216] S. Keller, C. Schaake, N. A. Fichtenbaum, C. J. Neufeld, Y. Wu, K. McGroddy, A. David, S. P. DenBaars, C. Weisbuch, J. S. Speck and U. K. Mishra: *Optical and structural properties of GaN nanopillar and nanostripe arrays with embedded InGaN/GaN multi-quantum wells*, J. Appl. Phys. **100**, 054314 (2006).

[217] J. D. Carey, L. L. Ong and S. R. P. Silva: *Formation of low-temperature self-organized nanoscale nickel metal islands*, Nanotechnology **14**, 1223 (2003).

[218] H.-W. Huang, C.-C. Kao, T.-H. Hsueh, C.-C. Yu, C.-F. Lin, J.-T. Chu, H.-C. Kuo and S.-C. Wang: *Fabrication of GaN-based nanorod light emitting diodes using self-assemble nickel nano-mask and inductively coupled plasma reactive ion etching*, Mater. Sci. Eng. B **113**, 125 (2004).

[219] M. J. Holmes, Y. S. Park, X. Wang, C. C. S. Chan, B. P. L. Reid, H. Kim, R. A. Taylor, J. H. Warner and J. Luo: *Optical studies on a single GaN nanocolumn containing a single $In_xGa_{1-x}N$ quantum disk*, Appl. Phys. Lett. **98**, 251908 (2011).

[220] J. Yoo, G.-C. Yi and L. S. Dang: *Probing exciton diffusion in semiconductors using semiconductor-nanorod quantum structures*, Small **4**, 467 (2008).

[221] J.-S. Hwang, F. Donatini, J. Pernot, R. Thierry, P. Ferret and L. S. Dang: *Carrier depletion and exciton diffusion in a single ZnO nanowire*, Nanotechnology **22**, 475704 (2011).

[222] L. Dai, B. Zhang, J. Y. Lin and H. X. Jiang: *Comparison of optical transitions in InGaN quantum well structures and microdisks*, J. Appl. Phys. **89**, 4951 (2001).

[223] H.-S. Chen, D.-M. Yeh, Y.-C. Lu, C.-Y. Chen, C.-F. Huang, T.-Y. Tang, C. C. Yang, C.-S. Wu and C.-D. Chen: *Strain relaxation and quantum confinement in InGaN/GaN nanoposts*, Nanotechnology **17**, 1454 (2006).

[224] Q. Wang, J. Bai, Y. P. Gong and T. Wang: *Influence of strain relaxation on the optical properties of InGaN/GaN multiple quantum well nanorods*, J. Phys. D: Appl. Phys. **44**, 395102 (2011).

[225] J. Bai, Q. Wang and T. Wang: *Characterization of InGaN-based nanorod light emitting diodes with different indium compositions*, J. Appl. Phys. **111**, 113103 (2012).

[226] H. W. Choi, C. W. Jeon, M. D. Dawson, P. R. Edwards, R. W. Martin and S. Tripathy: *Mechanism of enhanced light output efficiency in InGaN-based microlight emitting diodes*, J. Appl. Phys. **93**, 5978 (2003).

[227] D. Basko, G. La Rocca, F. Bassani and V. Agranovich: *Förster energy transfer from a semiconductor quantum well to an organic material overlayer*, Eur. Phys. J. B **8**, 353 (1999).

[228] M. Achermann, M. A. Petruska, S. Kos, D. L. Smith, D. D. Koleske and V. I. Klimov: *Energy-transfer pumping of semiconductor nanocrystals using an epitaxial quantum well*, Nature **429**, 642 (2004).

[229] N. Narendran, Y. Gu, J. P. Freyssinier-Nova and Y. Zhu: *Extracting phosphor-scattered photons to improve white LED efficiency*, Phys. Status Solidi A **202**, R60 (2005).

[230] H. Masui, S. Nakamura and S. P. DenBaars: *Effects of phosphor application geometry on white light-emitting diodes*, Jpn. J. Appl. Phys. **45**, L910 (2006).

[231] C. Sommer, P. Hartmann, P. Pachler, M. Schweighart, S. Tasch, G. Leising and F. P. Wenzl: *A detailed study on the requirements for angular homogeneity of phosphor converted high power white LED light sources*, Opt. Mater. **31**, 837 (2009).

[232] L. Zhu, X. H. Wang, P. Lai and H. Choi: *Angularly uniform white light-emitting diodes using an integrated reflector cup*, IEEE Photon. Technol. Lett. **22**, 513 (2010).

[233] J. H. Burroughes, D. D. C. Bradley, A. R. Brown, R. N. Marks, K. Mackay, R. H. Friend, P. L. Burns and A. B. Holmes: *Light-emitting diodes based on conjugated polymers*, Nature **347**, 539 (1990).

[234] D. Braun and A. J. Heeger: *Visible light emission from semiconducting polymer diodes*, Appl. Phys. Lett. **58**, 1982 (1991).

[235] F. Hide, P. Kozodoy, S. P. DenBaars and A. J. Heeger: *White light from InGaN/conjugated polymer hybrid light-emitting diodes*, Appl. Phys. Lett. **70**, 2664 (1997).

[236] R. Ziessel, G. Ulrich and A. Harriman: *The chemistry of bodipy: A new El Dorado for fluorescence tools*, New J. Chem. **31**, 496 (2007).

[237] A. Loudet and K. Burgess: *BODIPY dyes and their derivatives: Syntheses and spectroscopic properties*, Chem. Rev. **107**, 4891 (2007).

[238] G. Ulrich, R. Ziessel and A. Harriman: *The chemistry of fluorescent bodipy dyes: Versatility unsurpassed*, Angew. Chem. Int. Ed. **47**, 1184 (2008).

[239] A. L. Kanibolotsky, I. F. Perepichka and P. J. Skabara: *Star-shaped π-conjugated oligomers and their applications in organic electronics and photonics*, Chem. Soc. Rev. **39**, 2695 (2010).

[240] Y. Ikawa, S. Moriyama and H. Furuta: *Facile syntheses of BODIPY derivatives for fluorescent labeling of the 3' and 5' ends of RNAs*, Anal. Biochem. **378**, 166 (2008).

[241] L. Bonardi, H. Kanaan, F. Camerel, P. Jolinat, P. Retailleau and R. Ziessel: *Fine-tuning of yellow or red photo- and electroluminescence of functional difluoro-boradiazaindacene films*, Adv. Funct. Mater. **18**, 401 (2008).

[242] S. Hattori, K. Ohkubo, Y. Urano, H. Sunahara, T. Nagano, Y. Wada, N. V. Tkachenko, H. Lemmetyinen and S. Fukuzumi: *Charge separation in a nonfluorescent donor-acceptor dyad derived from boron dipyrromethene dye, leading to photocurrent generation*, J. Phys. Chem. B **109**, 15368 (2005).

[243] N. Boens, Q. Wenwu, M. Baruah, W. M. De Borggraeve, F. Aleksander, N. Smisdom, M. Ameloot, L. Crovetto, E. M. Talavera and J. M. Alvarez-Pez: *Rational design, synthesis, and spectroscopic and photophysical properties of a visible-light-excitable, ratiometric, fluorescent near-neutral pH indicator based on BODIPY*, Chem.-Eur. J. **17**, 10924 (2011).

[244] S. C. Dodani, Q. He and C. J. Chang: *A turn-on fluorescent sensor for detecting nickel in living cells*, J. Am. Chem. Soc. **131**, 18020 (2009).

[245] T. Förster: *Zwischenmolekulare Energiewanderung und Fluoreszenz*, Ann. Phys. **437**, 55 (1948).

[246] D. L. Dexter: *A theory of sensitized luminescence in solids*, J. Chem. Phys. **21**, 836 (1953).

[247] S. Diring, F. Puntoriero, F. Nastasi, S. Campagna and R. Ziessel: *Star-shaped multichromophoric arrays from bodipy dyes grafted on truxene core*, J. Am. Chem. Soc. **131**, 6108 (2009).

[248] N. J. Findlay, C. Orofino-Peña, J. Bruckbauer, S. E. T. Elmasly, S. Arumugam, A. R. Inigo, A. L. Kanibolotsky, R. W. Martin, and P. J. Skabara: *Linear oligofluorene-BODIPY structures for fluorescence applications*, J. Mater. Chem. C **1**, 2249 (2013).

[249] N. Greenham, I. Samuel, G. Hayes, R. Phillips, Y. Kessener, S. Moratti, A. Holmes and R. Friend: *Measurement of absolute photoluminescence quantum efficiencies in conjugated polymers*, Chem. Phys. Lett. **241**, 89 (1995).

Conference contributions

The presenting author is marked in **bold**.

Contributions to attended conferences:

1. 01/2013: **UK Nitride Consortium Winter Meeting** (Cardiff, UK):

   Talk: *"White light emission from InGaN/GaN nanorod LEDs using an organic compound for colour down conversion"*, **J. Bruckbauer**, N. J. Findlay, S. Arumugam, G. Conboy, M. Wallace, E. Taylor, A. R. Inigo, P. R. Edwards, J. Bai, T. Wang, P. J. Skabara, and R. W. Martin

2. 10/2012: **International Workshop on Nitride Semiconductors 2012** (Sapporo, Japan):

   Talk: *"Probing light emission from a single GaN nanorod containing multiple InGaN/GaN quantum wells"*, **J. Bruckbauer**, P. R. Edwards, J. Bai, T. Wang, and R. W. Martin

   Poster: *"Trench defects and threading dislocations in III-nitride structures investigated using scanning electron microscopy"*, **J. Bruckbauer**, P. R. Edwards, S.-L. Sahonta, G. Naresh-Kumar, M. J. Kappers, C. J. Humphreys, R. A. Oliver, C. Trager-Cowan, and R. W. Martin

   Poster: *"Spectral and emission characteristics of GaN nano-rods containing a single or multiple InGaN quantum wells"*, Y. Zhuang, S. Lis, **J. Bruckbauer**, S. E. J. O'Kane, P. A. Shields, P. R. Edwards, R. W. Martin, and D. W. E. Allsopp

   Talk: *"Applications of electron channelling contrast imaging for characterizing nitride semiconductor thin films in a scanning electron microscope"*,

G. Naresh-Kumar, B. Hourahine, P. R. Edwards, J. Bruckbauer, R. W. Martin, C. Mauder, A. Day, A. Winkelmann, P. Parbrook, A. Wilkinson, and C. Trager-Cowan

3. 07/2012: **UK Nitride Consortium Summer Meeting** (Sheffield, UK):

   Talk: *"Optical and structural studies of defects in nitride-based thin films using electron microscopes"*, **J. Bruckbauer**, G. Naresh-Kumar, S.-L. Sahonta, P. R. Edwards, T. Puchtler, S. Bennett, M. J. Kappers, C. J. Humphreys, R. A. Oliver, R. W. Martin, and C. Trager-Cowan

4. 01/2012: **UK Nitride Consortium Winter Meeting** (Bath, UK):

   Talk: *"Luminescence of single InGaN/GaN nanorods"*, **J. Bruckbauer**, P. R. Edwards, J. Bai, T. Wang, and R. W. Martin

   Talk: *"Study of cathodoluminescence by hyperspectral imaging of GaN Nanorods containing a single InGaN quantum well"*, **Y. Zhuang**, J. Bruckbauer, P. Shields, P. Edwards, R. Martin, and D. Allsopp

   Talk: *"Applications of electron channelling contrast imaging for characterising nitride semiconductor thin films"*, **N. Kumar**, J. Bruckbauer, P. R. Edwards, B. Hourahine, and C. Trager-Cowan

5. 07/2011: **9th International Conference on Nitride Semiconductors** (Glasgow, UK):

   Poster: *"Cathodo- and Photoluminescence Studies of Nanorods with Embedded InGaN/GaN Disks"*, **J. Bruckbauer**, P. R. Edwards, C. Trager-Cowan, P. Renwick, T. Wang, and R. W. Martin

6. 06/2011: **University of Strathclyde Research Day** (Glasgow, UK):

   Poster: *"Optical investigation of LED structures using cathodoluminescence hyperspectral imaging"*, **J. Bruckbauer**, P. R. Edwards, P. Renwick, T. Wang, and R. W. Martin (**Won best poster award for the Faculty of Science**)

7. 01/2011: **UK Nitride Consortium Winter Meeting** (Manchester, UK):

   Talk: *"High resolution cathodoluminescence hyperspectral imaging of*

InGaN/GaN multiple quantum wells", **J. Bruckbauer**, P. R. Edwards, T. Wang, and R. W. Martin

8. 03/2011: **SET for BRITAIN** (House of Commons, London, UK):

   Invited Poster: *"Optical investigation of LED structures using cathodoluminescence hyperspectral imaging"*, **J. Bruckbauer**, P. R. Edwards, P. Renwick, T. Wang, and R. W. Martin

9. 06/2010: **University of Strathclyde Research Day** (Glasgow, UK):

   Poster: *"Cathodoluminescence hyperspectral imaging of InGaN/GaN quantum wells"*, **J. Bruckbauer**, P. R. Edwards, T. Wang, and R. W. Martin

10. 03/2010: **DPG Spring Meeting of the Condensed Matter Division** (Regensburg, Germany):

    Talk: *"Cathodoluminescence hyperspectral imaging of InGaN/GaN quantum wells"*, **J. Bruckbauer**, P. R. Edwards, T. Wang, and R. W. Martin

Contributions to not attendend conferences:

1. 08/2013: **10th International Conference on Nitride Semiconductors** (Washington D.C., USA):

   Poster: *"White Light Emission from InGaN/GaN LEDs and Nanorods Using a Novel Organic Compound for Colour Conversion"*, J. Bruckbauer, N. J. Findlay, H. A. McMullen, A. R. Inigo, P. R. Edwards, J. Bai, T. Wang, F. Oehler, M. J. Kappers, C. J. Humphreys, R.A. Oliver, M. Hopkins, D. W. Allsopp, P. J. Skabara, and **R. W. Martin**

   Poster: *"Coincident Cathodoluminescence and Electron Channelling Contrast Imaging of Threading Dislocations in GaN"*, J. Bruckbauer, G. Naresh-Kumar, N. Allehiani, P. R. Edwards, S. Kraeusel, B. Hourahine, S. Lovelock, M. J. Kappers, C. J. Humphreys, M. A. Moram, R. A. Oliver, **R. W. Martin**, and C. Trager-Cowan

   Poster: *"Quantitative microstructural analysis of nitride thin films in the*

scanning electron microscope", C. Trager-Cowan, G. Naresh-Kumar, **N. Allehiani**, S. Kraeusel, B. Hourahine, S. Vespucci, J. Bruckbauer, M. Wallace, P. R. Edwards, R. W. Martin, A. Vilalta-Clemente, A. J. Wilkinson, A. J. Gray, A. P. Day4, A. Winkelmann, M. J. Kappers, M. A. Moram, R. A. Oliver, C. J. Humphreys, P. J. Parbrook, D. Maneuski, V. O'Shea, K. P. Mingard

2. 04/2013: **18th Microscopy of Semi-Conducting Materials** (Oxford, UK):

   Talk: *"Correlating structural and luminescence properties of nitride semiconductor thin films using ECCI and CL"*, **P. R. Edwards**, N. Kumar, J. Bruckbauer, N. Allehiani, S. Kraeusel, B. Hourahine, R. W. Martin, and C. Trager-Cowan

3. 03/2013: **Electron Back Scatter Diffraction Conference 2013** (Oxford, UK):

   Invited talk: *"Electron channelling contrast imaging of defects in III-nitrides"*, **C. Trager-Cowan**, G. Naresh-Kumar, N. Allehiani, S. Kraeusel, B. Hourahine, S. Vespucci, J. Bruckbauer, P. R. Edwards, R. W. Martin, C. Mauder, A. P. Day, A. Winkelmann, A. J. Wilkinson, P. J. Parbrook, D. Maneuski, V. O'Shea, and K. P. Mingard

4. 07/2012: **9th International Symposium on Semiconductor Light Emitting Devices 2012** (Berlin, Germany):

   Talk: *"Luminescence and structural investigation of defects in nitride-based LED structures using electron microscopy"*, J. Bruckbauer, G. Naresh-Kumar, S.-L. Sahonta, P. R. Edwards, T. Puchtler, S. Bennett, M. J. Kappers, C. J. Humphreys, R. A. Oliver, **R. W. Martin**, and C. Trager-Cowan

   Poster: *"Cathodoluminescence Hyperspectral Imaging Study of GaN Nanorods Containing a Single InGaN Quantum Well"*, **Y. Zhuang**, J. Bruckbauer, P. R. Edwards, P. A. Shields, R. W. Martin, and D. W. E. Allsopp

5. 06/2012: **International Conference on Extended Defects in Semiconductors** (Thessaloniki, Greece):

Talk: *"Applications of electron channelling contrast imaging for characterising nitride semiconductor thin films"*, **C. Trager-Cowan**, G. Naresh-Kumar, B. Hourahine, P. R. Edwards, J. Bruckbauer, R. W. Martin, C. Mauder, A. P. Day, G. England, A. Winkelmann, P. J. Parbrook, and A. J. Wilkinson

6. 03/2012: **Electron Back Scatter Diffraction Conference 2012** (NPL, London, UK):

   Talk: *"Applications of electron channelling contrast imaging for characterising nitride semiconductor thin films"*, **N. Kumar**, C. Trager-Cowan, B. Hourahine, J. Bruckbauer, P. R. Edwards, R. W. Martin,C. Mauder, A. P. Day, and G. England

7. 11/2011: **MRS Fall Metting 2011** (Boston, USA):

   Talk: *"Imaging and Identifying Defects in Nitride Semiconductor Thin Films Using a Scanning Electron Microscope"*, N. Kumar, J. Bruckbauer, P. Edwards, B. Hourahine, C. Mauder, H. Kalisch, A. Vescan, C. Giesen, M. Heuken, P. Shields, A. Day, G. England, and **C. Trager-Cowan**

8. 10/2011: **Cathodoluminescence 2011** (Gaithersburg, USA):

   Talk: *"Development of hyperspectral cathodoluminescence imaging systems for the characterization of semiconducting materials"*, **P. R. Edwards**, K. J. Lethy, J. Bruckbauer, N. Kumar, M. Wallace, F. Luckert, F. Sweeney, C. Trager-Cowan, K. P. O'Donnell, and R. W. Martin

   Talk: *"High resolution hyperspectral cathodoluminescence imaging of semiconductor and plasmonic nanostructures"*, **P. R. Edwards**, K. J. Lethy, J. Bruckbauer, A. W. Wark, and R. W. Martin

9. 09/2011: **Nano Meets Spectroscopy 2011** (NPL, London, UK):

   Poster: *"Cathodoluminescence hyperspectral imaging of individual nanorods with embedded InGaN/GaN nanodisks"*, J. Bruckbauer, P. R. Edwards, T. Wang, and **R. W. Martin**

10. 05/2010: **8th International Symposium on Semiconductor Light Emitting Devices 2010** (Beijing, China):

Talk: *"High spatial resolution cathodoluminescence mapping of InGaN/GaN LED structures"*, J. Bruckbauer, P. R. Edwards, **T. Wang** and R. W. Martin